Development of Novel Porous Materials and Thin Membranes for Gas Separations

A Dissertation
SUBMITTED TO THE FACULTY OF
UNIVERSITY OF MINNESOTA
BY

Feng Xue

IN PARTIAL FULFILLMENT OF THE REQUIREMENTS
FOR THE DEGREE OF
DOCTOR OF PHILOSOPHY

Professor Michael Tsapatsis, Advisor

January 2020

Acknowledgements

I would like to express my sincere appreciation to my advisor, Professor Michael Tsapatsis, for his guidance throughout my PhD study. It is a great honor to work with Professor Tsapatsis. His passion for science, rigorous attitude toward research, brilliant ideas and immense knowledge have always inspired me to become a good researcher. His patience and continuous support motivate me to keep moving forward even during challenging times. I am very grateful for his support during my job search. Besides my advisor, I am grateful for Professor Andre Mkhoyan, Professor Andreas Stein and Professor Paul Dauenhauer for serving on my committee and reviewing my thesis.

I would like to thank Center for Gas Separations funded by the Department of Energy, for supporting my doctoral research. Many thanks to Professor Jeffrey Long and Ever Velasquez (University of California, Berkeley) in the Center for collaboration on the MOF mixed matrix membrane project. I would like to thank Professor Andre Mkhoyan for his guidance on the TEM characterization in the MOF nanosheet project and LIPS membrane project.

I would like to thank all the past and present members in the Tsapatsis research group. I would like to especially thank: Dr. Meera Shete for helping me get started in the lab and for thought-provoking conversations; Dr. Xiaoli Ma and Dr. Kiwon Eum for training me on the membrane preparation and permeation measurements and for always being helpful and ready to answer my questions; Dr. Sabrina Conrad for collaboration on the ZIF nanosheet amorphization project and for her kind support especially in the last two years of my PhD study; Supriya Ghosh and Dr. Prashant Kumar for diligently carrying out the high resolution TEM measurements; Dr. Garrett Swindlehurst for being my mentor and giving me advice on career development during my fifth year of PhD study; Dr. Berna Topuz, Dr. Dandan Xu, Dr. Donghun Kim, Dr. Neel Rangnekar, Dr. Aparna Iyer, Dr. Maryam Khaleel, Xuekui Duan, Matheus Dorneles De Mello and Wenyang Zhao for their constant help and support.

My sincere thanks also go to staff at the University of Minnesota. I would like to thank Dr. Nick Seaton, Dr. Chris Frethem, Dr. Hanseung Lee, Dr. Javier Garcia Barriocanal, Dr. Jason Myers and Dr. Fang Zhou from the Characterization facility for their help with the sample preparation, microscopy and XRD measurements. I would like to thank Paul

Kimani and Tony Whipple from the Minnesota Nano Center for their help with the ALD experiments. Many thanks to Julie Prince, Teresa Bredahl and Daniel Williams at the Department of Chemical Engineering and Materials Science for their help with administrative affairs.

I also would like to thank all my friends for their constant support and friendship, and for the wonderful time we spent together. I would like to especially thank Xiaofan Feng and Dawei Chen for the entertainment, caring and emotional support they provided over the past ten years.

My deep and sincere gratitude goes to my family without whose constant support this would not have been possible. I am deeply grateful for my parents Dengwen Xue and Jinrui Li who provide unconditional love and care that have made me into the person I am today. They always believe in me and stand by my side that has helped me to get through difficult times. I would like to express my love and thank to my husband Tao Zhang. The best thing for me from the past five years is finding you. I truly thank Tao for constantly believing in me, supporting me and sharing this and future journey with me.

Dedication

To my family, Dengwen Xue, Jinrui Li and Tao Zhang

Abstract

The development of high-flux, high-selectivity, and low-cost membranes has the potential to improve the energy efficiency in the chemical industry by reducing the reliance on energy-intensive separation processes, such as distillation. To achieve this goal, novel porous materials and membrane fabrication methods are being increasingly sought after. Metal-organic frameworks (MOFs) are a new type of microporous materials with tunable pore structures suitable for gas separations. However, the high manufacturing cost and industrially-unattractive throughput hinder the industrial applications of MOF membranes. Fabrication of thin membranes with high throughput has the potential to overcome this barrier. This dissertation focuses on developing synthesis methods for thin MOF membranes by using two-dimensional (2D) MOF nanosheets and an all-vapor-phase zeolitic imidazolate frameworks (ZIFs) membrane synthesis process named ligand-induced permselectivation (LIPS). Crystal growth strategies for 2D MOFs were developed that yield Zn(Bim)OAc MOF nanosheets with desirable aspect ratio and uniformity for membrane formation. Using the Zn(Bim)OAc nanosheets, uniform coatings were successfully prepared on porous supports by vacuum filtration. A novel vapor growth method combining the support surface modification and ligand vapor treatment was developed to transform the nanosheet deposits into thin propylene-selective membranes. In addition, in an effort to reduce the membrane cost by using low-cost polymers, porous Cu(BDC) MOF nanosheets were incorporated into polymer matrices to form mixed matrix membranes that exhibited significantly improved performance for CO_2/N_2 separation. Besides solution processing of MOF membranes, a novel, well-controlled and cost-effective all-vapor-synthesis LIPS method with a combination of atomic layer deposition (ALD) and ligand vapor treatment was investigated. It was demonstrated that an ALD processing condition allowing a thin non-permeable ZnO deposit formation, as well as efficient ZnO-to-ZIFs conversion during ligand vapor treatment are very critical to realize consistent high membrane performance. With optimized ALD parameters, support and ligand properties, the membranes exhibit superior separation performance, with propylene permeance above 1.3×10^{-7} mol m^{-2} s^{-1} Pa^{-1} and propylene/propane selectivity above 60, which is highly promising for industrial applications.

Table of Contents

List of Tables

List of Figures

Chapter 1: Introduction

1.1 Membranes for gas separation

With increasing demands for clean and efficiently-produced energy, gas separation membranes have become an emerging separation technology to obtain desired molecules for fuels and plastics production.[1] Currently, the chemical separation accounts for 10-15% US total energy consumption, with almost 80% of this energy being consumed by energy-intensive thermal separation processes like distillation.[2] Membranes have the potential to partially replace these energy-intensive separations, and it has been shown that 90% less energy would be used by membrane-based separation compared with distillation. Besides high energy efficiency, the use of membranes occupies less space compared with absorbent materials and can be operated continuously.[3] These advantages make membrane-based gas separations highly attractive for industrial applications.

Membranes work by forming a barrier between the feed and permeate sides that allows the penetration of some species while restricting the movement of others.[4] This entire process is driven by the chemical potential difference (e.g. pressure, concentration difference) across the membrane. Based on how the molecules pass through the barrier, membranes are either dense or porous. Polymer membranes are dense membranes where molecules dissolve into the material and diffuse through it. The product of the solubility and diffusivity is the permeability. Porous membranes have pores that serve as a sieve where molecules can be separated by size and shape, thus they are also called molecular sieve membranes.[5]

The performance of membrane is primarily evaluated by permeability and selectivity. An ideal membrane would have both high permeability and selectivity. However, conventional

polymeric gas separation membranes currently used in industry suffer from a trade-off between permeability and selectivity in which higher permeability of a membrane correlates with lower selectivity, leading to an upper bound in the membrane separation performance plot.[6-7] This is because a more permeable membrane also has a more open structure thereby compromising selectivity. In order to realize high performance membranes, porous membrane materials with controllable pore sizes are highly desirable.

1.2 MOFs and MOF membranes

Metal-organic frameworks (MOFs) are an important class of crystalline porous materials consisting of metal ions/clusters interconnected with organic ligands.[8-9] As shown in **Figure 1-1**, they possess ordered pores, tunable pore sizes and functionalities, together with a remarkable degree of variability for both the metal ions and organic linkers.[10] Since the first discovery of MOFs by Prof. Yaghi's group in the late 1990s, this area of MOFs research has grown rapidly, with more than 20000 different MOF structures studied so far.[11-12]

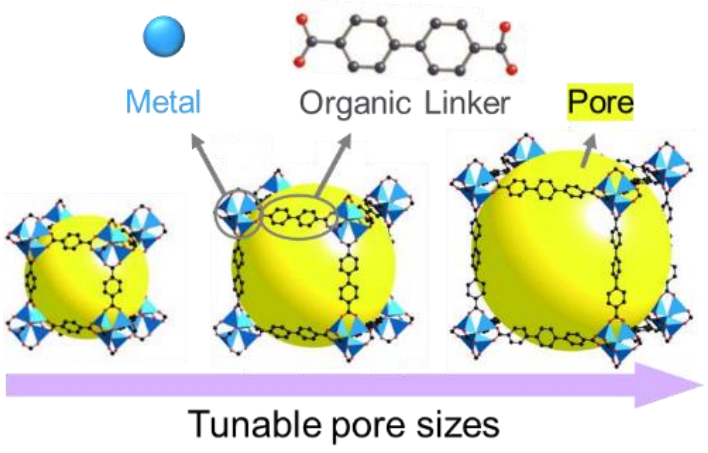

Figure 1-1. Schematics showing building blocks of MOFs and tunable pore sizes realized by linkers of different lengths. Adapted from reference 9.

The physical and chemical properties of MOFs greatly determine their applications. For example, the abundant active metal sites and the large surface area as high as 10000 m^2/g have made MOFs promising candidates in catalysis.[12-13] Due to the open porous framework structures with large accessible pore volumes and relative adsorption affinity, MOFs have shown exceptional performance as adsorbents for gas separations,[14-15] as well as storage of gases such as methane,[16] hydrogen[17] and carbon dioxide.[18] The pore size of MOFs is in the range of 0.2 – 9.8 nm, which covers well for the molecular size range of the industrial gas (0.3 – 1 nm), making MOFs highly promising for gas separation membranes.[12, 19] In particular, zeolitic imidazolate frameworks (ZIFs), a subclass of MOFs, have demonstrated tremendous potential as membrane materials for gas separation.[20-21]

ZIFs consist of transition metal ions connected with imidazole ligands in a way similar to the Si-O bond in zeolites (**Figure 1-2a**).[20, 22] ZIFs possess topology similar to zeolite, which endows ZIFs with excellent thermal and chemical stabilities as compared with most of other MOFs. Furthermore, the pore size of most ZIFs is well-defined in the range of 0.3-0.5 nm, enabling the kinetic separation of gas molecules with sub-angstrom size difference.[23-24]

The first MOF membrane for gas separation was reported in 2009 where continuous MOF-5 membrane supported on a porous alumina substrate was fabricated.[25] Since then, a number of studies have demonstrated the purification of hydrogen (e.g. H_2/CO_2,[26-29] H_2/CH_4[27-29]), carbon dioxide (e.g. CO_2/CH_4,[30-31] CO_2/N_2[31-32]) and light olefins (e.g. ethylene/ethane,[33-34] propylene/propane[35-37]) using MOF membranes. For example, one of the mostly investigated separations is the purification of propylene from its paraffin

propane. Propylene is a valuable chemical because it is primarily used as a monomer material for the production of polypropylene, which can be processed into a wide range of consumer and industrial products such as automotive parts, house wares, toys and bottle caps etc. Purification of light olefins (propylene/propane, ethylene/ethane) accounts for 0.3% of global energy use.[2] The current process of propylene production is by steam cracking of light hydrocarbons where propane acts as an impurity in the further processing steps. The separation of propylene from propane is currently realized by cryogenic distillation processes, which are very energy intensive due to the close boiling points of propylene (-48 °C) and propane (-42 °C). Instead, the propylene can be purified by passing a mixture of propylene and propane through a perm-selective ZIF-8 membrane (**Figure 1-2c**). The molecule size of propylene (4.03 Å) is slightly smaller than propane (4.16 Å). Despite the very small size difference, ZIF-8 membrane is highly selective for propylene over propane.[38]

ZIF-8 is one of the widely studied ZIFs that consist of zinc ions and 2-methylimidazole ligands. The structure of ZIF-8 is shown in **Figure 1-2b**. It possesses a sodalite (SOD) topology and the aperture size defined by the six-membered ring is 3.4 Å based on the single crystal x-ray diffraction characterization.[20] Due to the flexibility in organic ligand by rotation and flipping upon inclusion of guest molecules, the effective aperture size of ZIF-8 is larger. According to the adsorption study by Li and coworkers, propylene and propane can both enter the pores of ZIF-8, reaching a similar adsorption equilibrium. However, the diffusion rate of propylene is ~125 times higher than that of propane, indicating the great potential for kinetic separation of propylene/propane.[23] The molecular sieving properties of ZIF-8 were further studied by Koros et al. with kinetic uptake rate

measurements, giving rise to an effective aperture size of ZIF-8 in the range of 4.0 to 4.2 Å and an estimated ideal propylene/propane permselectivity of ZIF-8 membrane to be 130.[24]

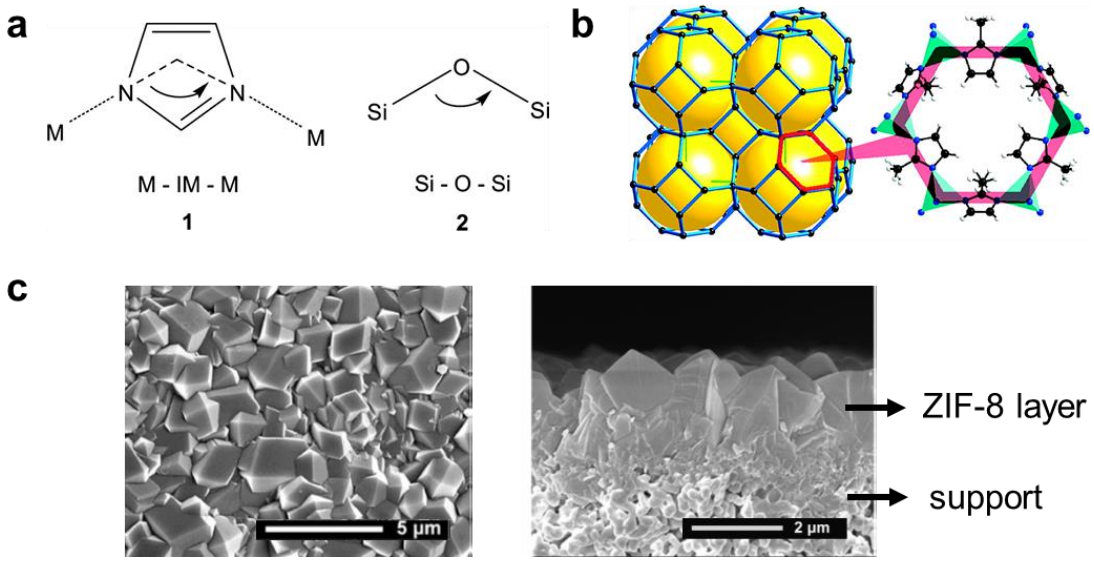

Figure 1-2. (a) The bridging angles in ZIFs (1) and zeolites (2). Adapted from reference 20. (b) (left) Sodalite topology and (right) narrow six-membered-ring opening through which molecules have to pass. Adapted from reference 40. (c) The (left) top and (right) cross section scanning electron microscopy (SEM) images of a ZIF-8 membrane. Adapted from reference 35.

The fabrication of MOF membranes, similar to zeolite membranes, is usually achieved by forming a continuous layer on the porous support primarily via two methods: in situ growth and seeded-assisted growth.[39] In the case of in situ growth, a bare support is immersed in the growth solution for heterogeneous nucleation and growth of a MOF membrane.[40] It is challenging to prepare continuous MOF films due to the poor membrane-substrate interaction. Thus many studies have focused on the surface modification of supports to promote the heterogeneous nucleation and enhance the interaction, such as the use of

covalent linkers (propyltriethoxysilane (APTES),[41-42] polydopamine[43]). Regarding seeded growth, nanosized seed crystals are synthesized and coated on the surface of the support with proper seeding techniques, such as rubbing[44] and dip coating,[35] followed by secondary growth via solvo- or hydrothermal synthesis to grow seed crystals into continuous membranes. Compared with in situ growth, seeded growth offers better control over the membrane thickness and microstructure by manipulating the size, shape and orientation of the deposited seed crystals.

The unique coordination chemistry of MOFs has also enabled new approaches for membrane fabrication. The fast reaction between many metal and ligand solutions without the need of a structure directing agent (SDA) has led to the membrane synthesis under mild conditions. For example, Jeong et al. reported a counter-diffusion method where well-intergrown ZIF-8 membrane was formed by first soaking the porous support into the metal solution and then transferred to the ligand solution for solvothermal growth. The metal ions and ligand counter diffuse and react at the surface of the support to form a continuous membrane.[36] In addition, the ability of MOFs to be synthesized in a solvent-free condition has promoted the development of vapor-phase membrane fabrication, which has cost and environmental advantages. For example, Stassen et al. reported the fabrication of ZIF-8 films on Si wafer by converting atomic-layer-deposition (ALD)-formed ZnO into ZIF-8 using ligand vapor treatment.[45] Inspired by this work, ligand vapor treatment methods have been developed to convert a Zn-based gel[46] or a ALD-ZnO deposit[47] into high performance ZIF-8 membranes.

1.3 Ultrathin MOFs and MOF membranes

Significant progress has been achieved in molecular sieve membranes based on the lab-scale studies, however, the deployment of the membranes in industry on a large scale has been primarily limited by the high cost of the membranes. For example, the cost of zeolite membranes is estimated to be $5,000 ~10,000 per square meter of a membrane module.[48] The solution to this, if the cost is not decreased further, is to increase the membrane throughput by 10 times, which can be realized by decreasing the membrane thickness. Therefore, ultrathin defect-free membranes are highly desirable.

One approach to obtain thin membranes as shown in **Figure 1-3** is to 1) prepare ultrathin anisotropic seed crystals, 2) deposit them onto a porous support with controlled orientation and then 3) apply a mild anisotropic crystal growth to seal all the gaps in between the seed crystals while minimizing the membrane thickness. The anisotropic seed crystals, with unit-cell (nm) thickness and large (μm) lateral dimensions, are called "nanosheets". Membranes fabricated from a zeolite nanosheet via this three-step process show unprecedented ultraselective performance for separation of xylene isomers.[49] Because of the ability to fine tune the pore structure and functionality of MOFs, MOF nanosheets are highly sought for achieving high performing membranes.

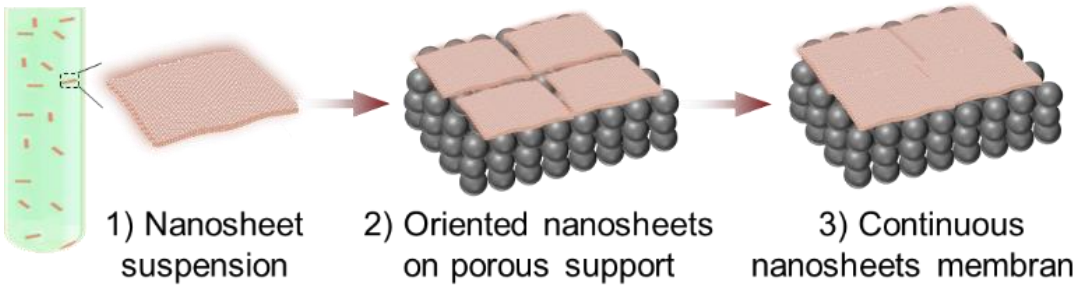

Figure 1-3. Schematics of the three-step process in fabricating nanosheet-based membranes.

MOF nanosheets are generally synthesized by two approaches: top-down approach and bottom-up approach. The top down approach involves exfoliation of layered MOFs precursors by methods such as sonication,[50-54] ball milling[26, 55-56] and chemical intercalation.[57] This method is simple and straight forward, but it often leads to damaged nanosheets and un-exfoliated particles, requiring a further purification step to collect the exfoliated nanosheets. Alternatively, a bottom-up approach (direct synthesis) requires careful design to restrict the growth of MOFs in one direction, which is often realized by the adsorption of surfactant molecules on certain crystal planes[58-65] or modulation of the contact manner between the metal and ligand solutions.[66-69] Direct synthesis often leads to a high yield of nanosheets with high aspect ratios, but it is challenging to perform well-controlled synthesis favoring two-dimensional growth.

The application of MOF nanosheets in membranes requires the preparation of a stable suspension containing pure crystalline nanosheets with uniform thickness and high aspect ratio. Peng et al. reported the fabrication of a H_2/CO_2-selective membrane consisting of multiple layers of MOF nanosheets supported on a porous alumina support.[26] The MOF nanosheets were achieved by exfoliation using wet ball milling. Rodenas et al. reported a three-layer synthesis method for a MOF nanosheet and incorporated it into a polymer matrix to form CO_2/CH_4-selective composite membranes.[66] Despite the progress, the development of MOF nanosheet-based membranes is still at a very early stage and many challenges abound including: the types of 2D MOFs that can be achieved in required quality are very limited due to the difficulty in synthesis, and the understanding of interactions between MOF nanosheets and the porous support/surrounding matrix during the membrane fabrication processes is very limited. To address these issues, in Chapter 2

and Chapter 3, synthesis methods for MOF nanosheets with required quality are explored, and the deposition and growth of MOF nanosheets on a porous support are discussed. A direct synthesis method is developed and uniform MOF nanosheet coatings are obtained on the porous support. In Chapter 4, the incorporation of MOF nanosheets into polymer matrices is studied and the favorable interaction between the MOF nanosheets and the surrounding matrix is achieved.

Another novel approach to obtain thin membranes, as recently demonstrated by Ma and Tsapatsis et al., is to utilize ALD to deposit ultrathin conformal layers of ZnO in a porous support, followed by ligand vapor treatment to convert ZnO into thin continuous confined ZIF deposits inside the mesopores, leading to high propylene/propane separation performance.[47] The understanding regarding the effects of different parameters in membrane formation is very limited, which hinders further optimization of the separation performance. In Chapter 5 this is discussed and superior separation performance is achieved.

1.4 Thesis outline

This dissertation is structured as follows.

Chapter 2 discusses the preparation of MOF nanosheets for membrane applications. To prepare nanosheets, exfoliation is first attempted and is found to be ineffective due to the damage to the nanosheets. The focus is then directed to the direct (bottom up) synthesis. A surfactant-assisted crystallization temperature-modulated direct synthesis method is developed for Zn-based MOF nanosheets which serve as building blocks of MOF membranes. The surfactant is removed from nanosheets based on a thermogravimetric

analysis. Using Langmuir-Shaefer type transfer, the nanosheets are introduced to a Si wafer which allows for the structural characterization using in-plane X-ray diffraction.

In Chapter 3, the obtained nanosheets described in Chapter 2 with high aspect ratio and desired pore orientation are used as seed crystals for membrane formation. Different types of inorganic supports and support modification methods are applied to enhance the interaction between the support surface and nanosheets. A vapor-phase secondary growth method is developed to tune the pore size and the microstructure of the MOF membranes. The resultant membranes are tested for propylene/propane separation.

Chapter 4 describes the synthesis of Cu-based MOF nanosheets and the incorporation of the nanosheets into a high permeability polymer, 6FDA-Durene, to form composite membranes. Using TEM, the stability of the MOF nanosheet under different processing conditions is examined and a condition to effectively prevent the nanosheet degradation during membrane fabrication is identified. A method to fabricate composite membranes at a high nanosheet loading is developed. The resulting composite membranes demonstrate remarkably enhanced performance for CO_2/N_2 separation compared to that of the neat polymer. The compatibility between the nanosheets and the polymer matrix is studied by microcopy analysis of the membrane microstructure as well as by gas permeation data analysis.

Chapter 5 discusses the fabrication of high performance ZIF-8 membranes using a novel all-vapor method including ALD of metal oxide layers and ligand vapor treatment. Effects of ALD processing parameters and support properties on the membrane separation performance are probed. X-ray diffraction and electron microscopy imaging are employed to characterize the crystallinity and the location of the selective ZIF layer. The optimized

membranes demonstrate both high permeability and selectivity for propylene/propane separation with performance well above the upper bound.

The summary of the conclusions from the dissertation and an outlook of the possible future research directions are described in Chapter 6.

Chapter 2: Synthesis of MOF nanosheets for membrane applications

Part of this chapter is published as:

F. Xue, P. Kumar, W. Xu, K. A. Mkhoyan, M. Tsapatsis, Direct Synthesis of 7 nm-Thick Zinc(II)–Benzimidazole–Acetate Metal–Organic Framework Nanosheets. *Chem. Mater.* **2018**, *30*, 69-73.

2.1 Introduction

Metal-organic frameworks (MOFs) are crystalline porous materials consisting of metal ions or clusters connected by bridging organic ligands.[8, 10] They have regularly arranged pores, tunable pore sizes and functionalities based on a diverse range of inorganic and organic building blocks that can be used.[12, 70] These unique features make MOFs promising candidates in gas storage, separations and catalysis.[13-14, 35-37, 39] As with other materials, the ability to control crystal size and morphology is essential for enabling optimal use in such applications.[71-74] More specifically, MOF nanosheets with few-nanometer thickness and large lateral dimensions, hold promise for ultraselective highly permeable gas separation membranes because molecularly sized pores oriented perpendicular to the basal plane can ensure the desirable separation selectivity and increased permeance along their thin dimension.[26, 66, 75-76] For the preparation of nanosheet-based membranes, it is a critical prerequisite to obtain a stable suspension containing crystalline nanosheets with uniform thickness and high aspect ratio.[49, 77] However, it remains challenging to synthesize stable MOF nanosheet suspensions satisfying these requirements.

Similar to other nanosheets, MOF nanosheets can be fabricated by two approaches. The top-down approach involves delamination of layered MOF precursors via methods such as

sonication and chemical intercalation.[50-52, 57, 78] This approach is simple but the obtained nanosheets often suffer from structural deterioration, fragmentation and aggregation. Moreover, this approach has often a low yield and is challenging to control the morphology of nanosheets. The direct (bottom-up) synthesis of MOF nanosheets is more desirable but relies on our ability to direct crystal growth to form high-aspect-ratio nanosheets at reasonable yield. Apart from few recent reports on zeolitic imidazolate framework nanosheets,[68, 79] there are only two series of MOFs that could be directly synthesized as discrete ultrathin nanosheets dispersible in solvents.[65-66] Rodenas et al. reported a three-layer synthesis method for M-BDC (M = Cu, Co, BDC = 1,4-benzenedicarboxylate) nanosheets by modulating the growth kinetics of MOF crystals.[66] The obtained nanosheets were successfully applied for the fabrication of CO_2-selective MOF-polymer composite membranes. Zhao et al. introduced a polymer as surfactant in the synthesis of M-TCPP (M = Zn, Cu, Cd, Co, TCPP = tetrakis (4-carboxyphenyl)porphyrin) nanosheets.[65] They proposed that the attachment of surfactant on the MOF surface restricts the thermodynamically favored layer-stacking growth and helps to stabilize the nanosheets, yielding high-aspect-ratio nanosheets with sub-10 nm thickness. In order for these nanosheets to be used for membrane applications, the polymer surfactant should probably have to be removed.

We start our investigation from the straight-forward top-down approach. A H_2/CO_2 selective membrane consisting of multiple layers of exfoliated MOF nanosheets supported on a porous alumina support was reported previously, where the exfoliation was achieved by ball-milling in organic solvents.[26] The effectiveness of this exfoliation method is evaluated and a new exfoliation method for MOFs is attempted, which suggests direct

synthesis is necessary to meet the quality requirements of MOF nanosheets for membrane applications. Here we report the direct synthesis of dispersible Zn(Bim)OAc (Bim = benzimidazole, OAc = acetate) MOF nanosheets. Zn(Bim)OAc and its isostructural counterpart Co(Bim)OAc were originally reported in the form of bulk materials.[80-81] Later, a lamellar structure consisting of Zn(Bim)OAc interleaved with cethyltrimethylammonium bromide (CTAB) was reported by Lotsch and co-workers. However, exfoliation of the lamellar structure in organic solvents resulted mainly in anisotropic nanobelts. Moreover, the nanobelts contain CTAB surfactant.[78] With the direct synthesis method reported here, ultrathin Zn(Bim)OAc nanosheets are produced without fragmentation. Furthermore, it is demonstrated that synthesis temperature is critical to tuning the morphology of the nanostructure from nanobelts to nanosheets. We also demonstrate the formation of oriented deposits and the removal of the surfactant via a heat treatment. This work paves the way toward evaluation of Zn(Bim)OAc for membrane applications.

2.2 Experimental

2.2.1 Chemicals

Zinc nitrate hexahydrate ($Zn(NO_3)\cdot 6H_2O$, 98%), Benzimidazole (98%), 1-hexanol (98%), n-heptane (99%), tetrahydrofuran (THF, 99%), and zinc acetate dihydrate ($Zn(OAc)_2\cdot 2H_2O$, 98%) were purchased from Sigma-Aldrich. Cetyltrimethylammonium bromide (CTAB, $C_{19}H_{42}NBr$, 99%) was purchased from Amresco. N,N-dimethylformamide (DMF, 99.9%), methanol (99.8%), 1-propanol (99%), toluene (99.5%) and ethyl alcohol (200 proof) were purchased from Fisher Scientific. All chemicals were used as received without any further purification.

2.2.2 Synthesis of $Zn_2(Bim)_4$ MOF precursor

$Zn_2(Bim)_4$ was synthesized by a modified protocol of hydrothermal transformation of ZIF-7.[27] To synthesize ZIF-7 nanoparticles, 1000 ml DMF was added to a solid mixture of 3.025 g $Zn(NO_3)\cdot 6H_2O$ and 7.695 g benzimidazole and stirred for 1 h. The solution was kept static at room temperature for 72 h, followed by repeated centrifugation in methanol and distilled water to recover and wash the product. The obtained ZIF-7 particles were then dispersed in distilled water at a concentration of 0.5 wt%, boiled and refluxed at 100 °C for 48 h. The $Zn_2(Bim)_4$ precipitate was collected by centrifugation at 15000 RCF (relative centrifugal force) for 30 min, washed with methanol 3 times (15000 RCF, 30 min), and dried at 50 °C overnight.

2.2.3 Exfoliation of $Zn_2(Bim)_4$ by ball milling

Typically, the $Zn_2(Bim)_4$ was dispersed in a solvent mixture of methanol and 1-propanol (V:V=1:1) at a concentration of 0.25 mg/ml in a ball milling jar. The jar was fixed in a lab roller mill and the suspension then underwent wet ball milling at a rotation speed of 45 rpm for 30 minutes. The suspension after ball milling was recovered and analyzed.

2.2.4 Exfoliation of $Zn_2(Bim)_4$ by polymer melt compounding

Typically, 0.03 g $Zn_2(Bim)_4$ was mixed with 14.97 g polystyrene (molecular weight = 1300 g/mol or 35000 g/mol), added into the melt-compounder (Xplore micro compounder MC15) and mixed for 1 h at 60 °C, 90 °C or 120 °C to achieve exfoliation with different forces. Then 2 g of the extruded composite materials was dissolved in 45 ml of toluene inside a centrifuge tube and centrifuged at 40,000 g for 3 h. The precipitate was collected and then washed 3 times with toluene to remove the polymer residue. Finally, the $Zn_2(Bim)_4$ cake after exfoliation was obtained at the bottom of the centrifuge tube.

2.2.5 Synthesis of thin Zn(Bim)OAc with CTAB

Thin Zn(Bim)OAc was synthesized according to a previously reported procedure with some modifications.[78] 5.4 ml benzimidazole solution (0.6 M in 1-hexanol) and 2.7 ml zinc acetate dihydrate solution (1.2 M in water) were added to a suspension containing 3.645g CTAB and 200 ml of the mixture of n-heptane and 1-hexanol (V:V=9.4:1) under stirring. The reaction solution was stirred vigorously at room temperature for 10 min and then treated at 110 °C, 60 °C or 25 °C to achieve thin Zn(Bim)OAc with different morphologies. The treatment time was varied from 16 h to 5 d.

Zn(Bim)OAc nanobelts shown in **Figures 2-5b,e** were prepared by refluxing the reaction solution at 110 °C in an oil bath for 16 h. Thin Zn(Bim)OAc shown in **Figures 2-5c,f** were prepared by refluxing the reaction solution at 60 °C in an oil bath for 20 h. For the Zn(Bim)OAc nanosheets shown in **Figures 2-5d,g**, the reaction solution was stirred at 25 °C for 20 h and kept under static condition for 4 d. After the reaction, the white product was collected by centrifugation at 12500 RCF for 20 min followed by decantation. The solid was washed twice in a mixed solvent of n-heptane and 1-hexanol (V:V=9.4:1) and was re-dispersed in 200 ml of the mixed solvent of n-heptane and 1-hexanol (V:V=9.4:1). Zn(Bim)OAc nanosheets synthesized at 25 °C were further transferred from the mixed solvent of n-heptane and 1-hexanol (V:V=9.4:1) to THF by 3 times washing with THF. The collected Zn(Bim)OAc nanosheets were re-dispersed in 200 ml THF and kept static in several 20 ml vials for at least two weeks in order to remove nanosheet aggregates. After the sedimentation, about 80% of top suspension was collected. Finally, Zn(Bim)OAc nanosheets were washed 4 times with THF and re-dispersed in 50 ml THF.

2.2.6 Synthesis of Zn(Bim)OAc without CTAB

Bulk Zn(Bim)OAc was synthesized according to a literature method.[78] The synthesis was similar to the synthesis of thin Zn(Bim)OAc without adding the CTAB surfactant. Briefly, 5.4 ml benzimidazole solution (0.6 M in 1-hexanol) and 2.7 ml zinc acetate dihydrate solution (1.2 M in water) were added to 200 ml of the mixture of n-heptane and 1-hexanol (V:V=9.4:1) under stirring. The reaction solution was stirred vigorously at room temperature for 10 min and then refluxed at 110 °C in an oil bath for 16 h. The obtained white product was collected by centrifugation at 10000 RCF (relative centrifugal force) for 10 min followed by decantation. The solid was washed 5 times in 200 proof ethanol and dried in an air oven overnight at 70 °C.

2.2.7 Nanosheet coating process via stamping

Zn(Bim)OAc nanosheets were coated on Si wafer using the Langmuir–Schaefer deposition technique as reported previously.[49, 82-84] 500 μl of the dispersion was added dropwise onto the surface of water in a polystyrene Petri dish (35-mm diameter). To transfer Zn(Bim)OAc nanosheets to the Si wafer, the Si wafer was lowered slowly and contacted with the surface of water. Then, the Si wafer was slightly tilted and lifted upward. The small amount of water remaining on the Si wafer was blown away by air flow.

2.2.8 Characterization

TEM samples of $Zn_2(Bim)_4$ were prepared by applying a few drops of $Zn_2(Bim)_4$ suspension in methanol/1-propanol (V:V=1:1) or toluene onto TEM grids (ultrathin carbon film on holey carbon support film, 400 mesh Cu, Ted Pella). TEM samples of Zn(Bim)OAc were prepared by applying a few drops of thin Zn(Bim)OAc suspension in n-heptane/1-hexanol (V:V=9.4:1) or THF onto TEM grids (ultrathin carbon film on holey carbon

support film, 400 mesh Cu, Ted Pella). The grids were dried at room temperature and imaged. Conventional TEM imaging and diffraction were performed on FEI Tecnai T12 TEM operating at 120 kV.

TGA analysis was performed using a Shimadzu TGA-50 analyser. The analysis was carried out for CTAB-free Zn(Bim)OAc, CTAB and CTAB-containing Zn(Bim)OAc nanosheets by heating 11-13 mg samples in air flow (50 mL/min) from 25 °C to 700 °C at a heating ramp rate of 5 °C/min. Heat treatment was carried out by heating about 12 mg fine powder of CTAB-containing Zn(Bim)OAc nanosheets in air flow (50 mL/min) from 25 °C to 325 °C at a heating ramp rate of 5 °C/min and holding the sample at 325 °C for 15 h.

SEM images were collected by using a Hitachi SU 8230 or JEOL 6700 microscope operated at 1.5 kV.

EDS was performed on a JEOL 6500 microscope at 15 kV.

AFM was performed in tapping mode using a Bruker Nanoscope V Multimode 8. The supported nanosheets on Si wafer were prepared via stamping.

XRD patterns of $Zn_2(Bim)_4$, CTAB-containing Zn(Bim)OAc nanosheets before and after heat treatment were recorded by using a Bruker-AXS (Siemens) D5005 diffractometer with a CuKα radiation source.

High-resolution powder diffraction patterns for the thin CTAB-containing Zn(Bim)OAc were collected at beamline 17-BM of the Advanced Photon Source with a monochromatic beam of 0.72768 Å at Argonne National Laboratory. Data collected in transmission geometry were processed with GSAS II[38] and converted to 2θ values which correspond to Cu Kα radiation.

The in-plane XRD measurements were carried out at beamline 33-BM-C of the Advanced Photon Source (0.7749 Å), Argonne National Laboratory. The instrumentation includes a bending magnet source with a Si(111) monochromator with the beam spot of 0.9 × 0.5 mm. The Si wafer coated with Zn(Bim)OAc nanosheets was placed on a Huber 4-circle stage and held almost parallel to the incident beam. The detector was set to move in the plane of the sample. Collected data were then converted to 2θ values corresponding to Cu Kα radiation.

The simulated powder XRD patterns of $Zn_2(Bim)_4$ and Zn(Bim)OAc were collected with Mercury software based on the reported single crystal data.[80, 85] (Cambridge Crystallographic Data Centre No. 675375 for $Zn_2(Bim)_4$ and No. 654813 for Zn(Bim)OAc)

2.2.9 Thickness determination using HAADF-STEM

HAADF-STEM image simulations were performed using Multislice method with TEMSIM code.[86] Simulations were performed for MFI unit cell of thickness 1.5 u.c. along b-direction and Zn(Bim)OAc unit cells of thickness 1-11 u.c. along a-direction. Simulation parameters (**Table 2-1**) were chosen to match the experimental conditions. The average ADF intensity (I) of the Zn(Bim)OAc and MFI nanosheets were calculated as:

$$I_{\mathrm{Zn(Bim)OAc}} = \frac{\sum_{i,j} I_{i,j}}{b_{Zn(Bim)OAc} * c_{Zn(Bim)OAc}}$$

$$I_{\mathrm{MFI}} = \frac{\sum_{i,j} I_{i,j}}{a_{MFI} * c_{MFI}}$$

where $I_{i,j}$ is the intensity value at pixel i, j in the simulated image of a single unit cell of Zn(Bim)OAc and MFI, and $b_{Zn(Bim)OAc}$ = 9.837 Å, $c_{Zn(Bim)OAc}$ = 8.821 Å, a_{MFI} = 20.022 Å, c_{MFI}=13.383 Å are corresponding lattice parameters. Intensity ratios for x = 1 – 11 u.c. were calculated as:

$$R_x = \frac{I_{Zn(Bim)OAc,\ x}}{I_{MFI}}$$

R_x was plotted with respect to thickness (t) of Zn(Bim)OAc nanosheet along a-direction ($t = x * a_{Zn(Bim)OAc}$, where $a_{Zn(Bim)OAc}$ = 10.818 Å). This graph (**Figure 2-7c**) was used as a calibration curve to convert experimentally obtained intensity ratios to thickness of the nanosheet.

A STEM sample was prepared by drop-casting a suspension of MFI nanosheets onto ultrathin carbon film on holey carbon support film (400 mesh Cu, from Ted Pella) and allowing it to air dry at room temperature. Furthermore, a suspension of thin Zn(Bim)OAc nanosheets in n-heptane/1-hexanol (V:V=9.4:1) was drop casted onto the same grid and again air dried at room temperature. HAADF-STEM images were acquired using aberration-corrected FEI Titan 60-300 (S)TEM, equipped with an analytical Super-Twin pole piece and FEI SuperX EDX detector, operating at 80 kV and 200 kV (**Table 2-1**).

HAADF-STEM images were acquired with MFI nanosheets (internal standard sample) and Zn(Bim)OAc nanosheets located within the same imaging window (**Figure 2-8**). This ensures that the ADF detector parameters, probe parameters, and pixel size[87] are the same for MFI and Zn(Bim)OAc nanosheets. Histograms for sections containing only the MFI and Zn(Bim)OAc nanosheets were plotted (**Figure 2-7b**) from images acquired at 80 kV and 200 kV (**Figures 2-8c,d**). The experimental *Intensity Ratios* were calculated by dividing the *Intensity* values for Zn(Bim)OAc in the *Counts* vs. *Intensity* histograms (blue curves in **Figure 2-7b**) with the *Intensity* value corresponding to the MFI peak in the *Counts* vs. *Intensity* histograms (intensity corresponding to the peak of the red curves in **Figure 2-7b**). These *Intensity Ratios* were then used to determine the corresponding Zn(Bim)OAc *Thicknesses* from the simulation-based calibration curves (**Figure 2-7c**).

The *Counts* vs. *Thickness* histograms were then generated (**Figure 2-7d**) using these *Thicknesses*.

Table 2-1. HAADF-STEM Imaging and Simulation parameters

Parameter	Experiment$_1$	Simulation$_1$	Experiment$_2$	Simulation$_2$
Voltage	200 kV	200 kV	80 kV	80 kV
Convergence angle (α)	24 mrad	24 mrad	21 mrad	21 mrad
Detector inner angle (α_1)	37 mrad	37 mrad	56 mrad	56 mrad
Pixel size	1.88 nm/pixel	0.13 Å/pixel	1.88 nm/pixel	0.13 Å/pixel
Beam current	10 pA	NA	30 pA	NA

2.2.10 Mass calculations for TGA and heat treatment process

For 100% pure Zn(Bim)OAc, the molecular weight $M_{(Zn(Bim)OAc)}$ = 241.54 g/mol

From 241.54 g Zn(Bim)OAc, we will get 1 mol ZnO after full calcination. $M_{(ZnO)}$ = 81.41 g/mol

$$\frac{81.41\ \text{g/mol}}{241.54\ \text{g/mol}} \times 100\% = 33.7\%$$

The residue weight percent of 33.7% compares well with 33.2% obtained from TGA.

For CTAB-containing nanosheets, after heat treatment at 325 °C for 15 h, 78.0% of mass was retained, within which the atomic ratio of Zn to Br is 1 : 0.06 based on the EDS measurement.

Consider 100 g CTAB-containing nanosheets, if we assume complete removal of surfactant, there are X g Zn(Bim)OAc and (78.0 − X) g Br, then

$$\frac{\left(\frac{\mathrm{X\ g}}{241.54\ \mathrm{g/mol}}\right)}{\frac{(78.0-\mathrm{X})\mathrm{g}}{79.90\ \mathrm{g/mol}}} = \frac{1}{0.06}$$

$$\mathrm{X} = 76.5\ \mathrm{g}$$

The remaining 78.0 g sample contains 76.5 g Zn(Bim)OAc and 1.5 g Br.

Based on this composition, after full calcination to 700 °C, the mass of ZnO is

$$76.5\ \mathrm{g} \times \frac{81.41\ \mathrm{g/mol}}{241.54\ \mathrm{g/mol}} = 25.8\ \mathrm{g}$$

The total amount of residue will be

$$25.8\ \mathrm{g\ ZnO} + 1.5\ \mathrm{g\ Br} = 27.3\ \mathrm{g}$$

By assuming no surfactant presence in heat-treated nanosheets, 27.3% of residue is calculated, which compares well with 26.8% residue obtained from TGA. This further confirms that the surfactant has been removed after the heat treatment.

2.3 Results and discussion

2.3.1 $Zn_2(Bim)_4$ nanosheets prepared by exfoliation

The layered MOF precursor $Zn_2(Bim)_4$ is built from zinc ions and benzimidazole (Bim) ligand. Two-dimensional layers lie in the ab plane and stack in a shifted fashion to form a monoclinic crystal. Within the layer, as shown in **Figure 2-1a**, two pairs of parallel Bim ligands connect four Zn atoms to form a square unit with a diagonal length about 8.1 Å. The aperture size identified from this four-membered ring is estimated to be 2.1 Å.[26] **Figure 2-1b** shows that the weak interlayer van der Waals interaction comes from the benzene rings of Bim ligands from the neighboring layer stacking in a face to edge arrangement, with an interlayer distance of 9.7 Å. Powder X-ray diffraction (XRD) pattern (**Figure 2-2a**) of the as-synthesized layered precursor matches the simulated pattern of $Zn_2(Bim)_4$, confirming the structure of the synthesized material. The morphology was characterized by scanning electron microscopy (SEM) (**Figure 2-2b**) and transmission electron microscopy (TEM) (**Figure 2-2c**), where 1-6 μm crystals with a thick-platelet morphology were identified.

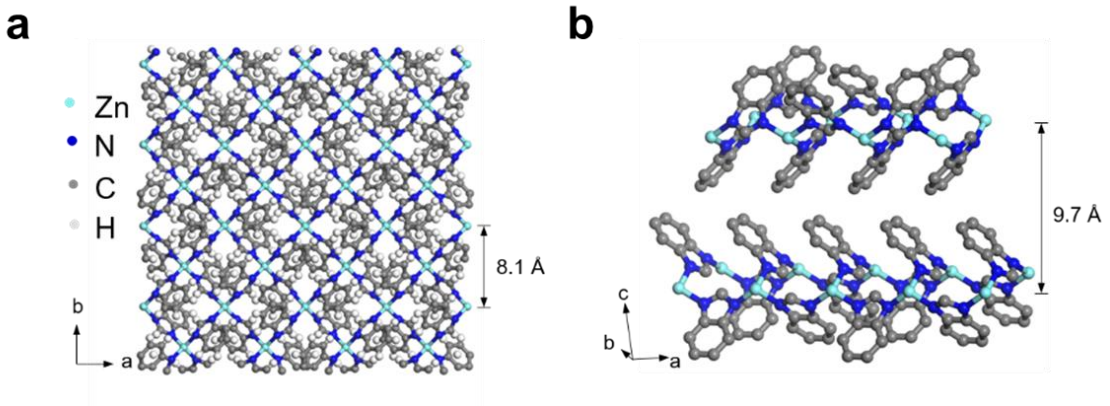

Figure 2-1. (a) Structure of a single layer $Zn_2(Bim)_4$ in the ab plane showing a square unit and a diagonal length of 8.1Å. (b) Representation of C-H···π stacking interactions between 2D layers and the interlayer distance of 9.7 Å is labeled.

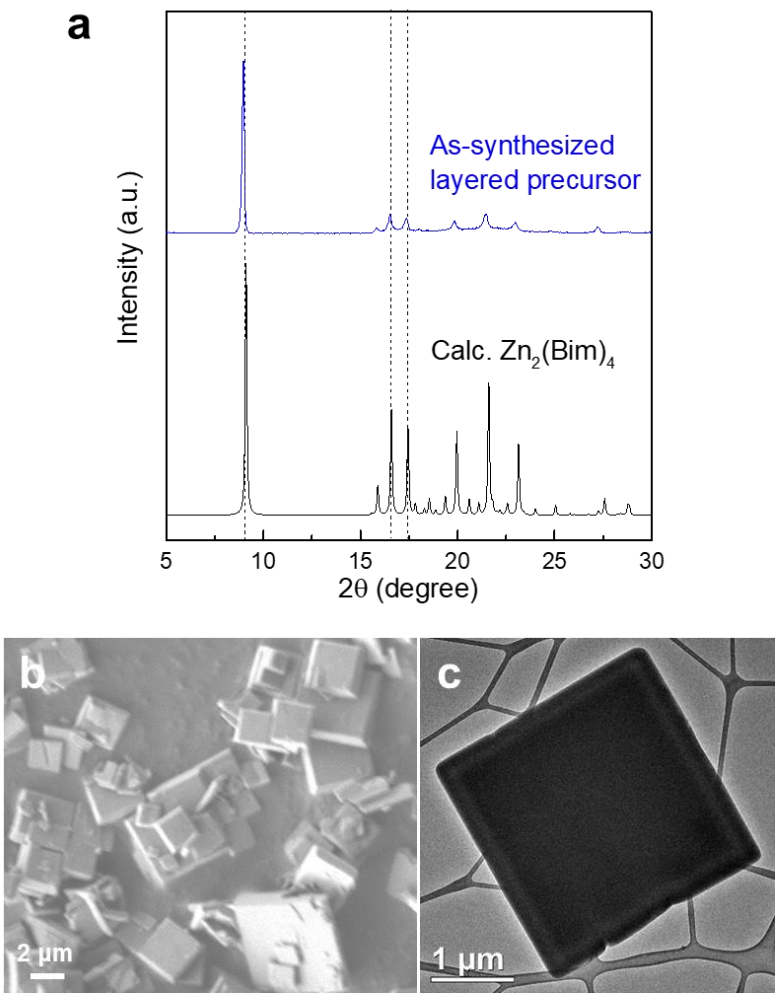

Figure 2-2. (a) XRD pattern (b) SEM and (c) TEM images of as-synthesized $Zn_2(Bim)_4$ crystals.

Exfoliation of $Zn_2(Bim)_4$ by ball milling was carried out in solvents of methanol and 1-propanol. To avoid intense shock stress that can destroy the in-plane structure of the MOF crystal, the suspension was ball milled at a very low rotation speed of 45 rpm for 30 minutes. The sheets after exfoliation treatment were characterized by TEM and selected area electron diffraction (SAED). From TEM imaging, it is possible to find several-layered nanosheets (**Figures 2-3a,d**). The lateral dimension of the sheets ranges from 100 nm to 1

μm. The sheets preserve their structure as evidenced by the electron diffraction pattern (**Figure 2-3e**), which shows a good agreement with the simulated diffraction pattern along the c axis of the $Zn_2(Bim)_4$ nanosheet (**Figure 2-3f**). The thickness of a typical sheet was determined to be about 8 nm, with a calibration method that is discussed in detail in **section 2.2.9**. Although thin sheets (5-10 nm thick) could be created by ball milling, ball milling was found to produce a low exfoliation yield as shown in **Figure 2-3b**, and to create debris by brittle-fracture (**Figure 2-3c**), which is detrimental to membrane formation.

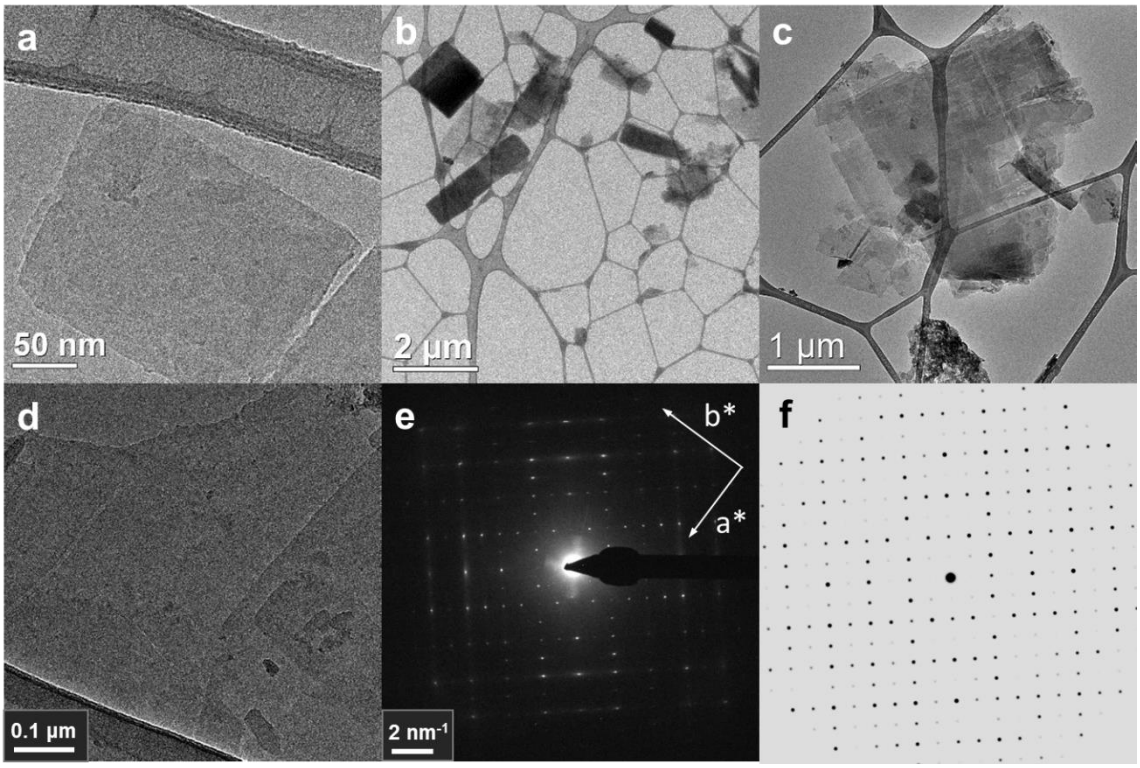

Figure 2-3. TEM images of samples after ball milling treatment. (a) The thinnest sheet found. (b) The low-magnification image showing a distribution of very little thin sheets among many thick particles. (c) Fragmented sheets and debris. (d) A thin sheet where SAED was taken from. (e) Experimental SAED pattern from (d). (f) Simulated diffraction pattern down the c axis of a $Zn_2(Bim)_4$ nanosheet.

To address this problem, polymer melt compounding exfoliation, which was successfully applied to obtain zeolite nanosheets,[77] is attempted. Melt blending is performed in a co-rotating twin screw extruder with a recirculation channel under nitrogen environment. It generates shear force, which is expected to slide apart stacks and produce single layers. Polystyrene, a hydrophobic polymer, is used to form composites with the MOF particles based on the hydrophobic π-π stacking interaction between $Zn_2(bim)_4$ layers. Melt temperature and polymer molecular weight are two processing parameters that influence the exfoliation effect. As shown in **Table 2-2**, a range of temperatures and polymer molecular weights are attempted, indicating that lower temperature and higher molecular weight polymer generate higher shear stress but lower diffusion rate of polymers.

Table 2-2. Experimental details in polymer melt compounding exfoliation

Polymer Mw (g/mol)	Melt Temperature (°C)	Average Shear Force (N)
35000	120	2500
35000	150	1200
1300	60	2250
1300	90	375
1300	120	15

After the treatment, the sheets are recovered from dissolving and removing polystyrene. TEM images of typical sheets obtained under these conditions are demonstrated in **Figure 2-4**. Except the treatment of polystyrene oligomer (Mw=1300 Da) at 120 °C (**Figure 2-4e**) where the viscosity is too low to exert any shear force, all other conditions could produce

smaller stacks with several layers. The exfoliated sheets are rare, which indicates lack of penetration of the polymer into the MOF interlayer gallery due to a very small interlayer distance (9.7 Å).

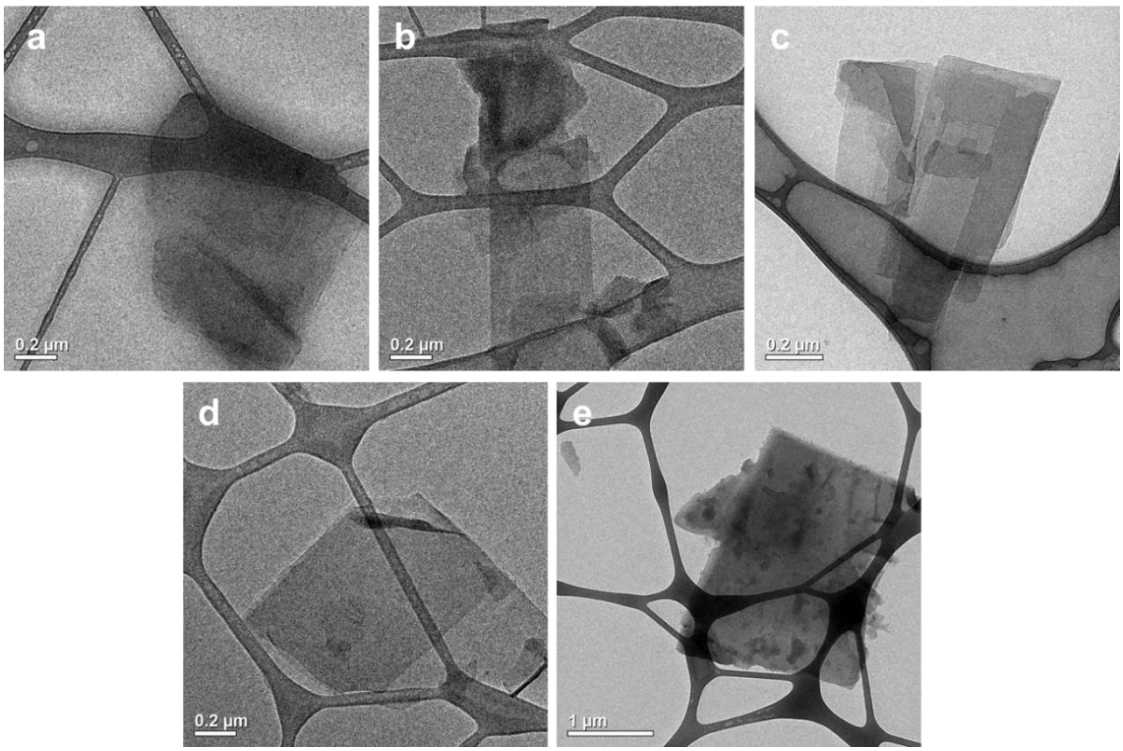

Figure 2-4. TEM images of representative sheets after melt compounding treatment at different conditions. (a) Mw=35000 g/mol, T=120 °C (b) Mw=35000 g/mol, T=150 °C (c) Mw=1300 g/mol, T=60 °C (d) Mw=1300 g/mol, T=90 °C (e) Mw=1300 g/mol, T=120 °C.

Both the exfoliation methods, ball milling and polymer melt compounding, have limitations in preparing pure ultrathin nanosheets at a high yield. Therefore, for membrane applications, direct synthesis of MOF nanosheets is the desirable way forward.

2.3.2 Direct synthesis of Zn(Bim)OAc nanosheets

The structure of Zn(Bim)OAc as proposed in ref. 80 is shown in **Figure 2-5a**. Two-dimensional (2D) layers are stacked along the a axis due to van der Waals forces. Within the 2D layer, each Zn ion is coordinated with two benzimidazole ligands and two acetate ligands in a distorted tetrahedral geometry, and each benzimidazole and acetate connect with two Zn ions. Interestingly, all the Zn-benzimidazole-Zn (Zn-Bim-Zn) linkages are along the b axis while all the Zn-acetate-Zn (Zn-OAc-Zn) linkages are along the c axis. Their crossing creates four-membered ring within the layer, with an aperture size that can be estimated from crystallographic data to be ~ 2.4 Å. Following the conventional solvothermal synthesis protocol reported in ref. 78, plate-like MOF crystals with lateral size ranging from 100 nm to 12 μm were obtained, some of which are grown together, forming irregularly-shaped particles (**Figure 2-6**).

Following ref. 78, CTAB is introduced to regulate the crystal nucleation and growth. As a cationic surfactant, CTAB has been proposed to selectively attach to basal crystal planes to enable anisotropic growth of Zn(Bim)OAc and other MOFs[88] in a controlled manner. The presence of the CTAB hydrophobic tail on the crystal surface could also stabilize it and prevent lamellar stack-ing by dispersing the nanosheets in solvents with which CTAB has favorable interactions. The synthesis was first carried out for 16 h at 110 °C which is slightly higher than the 100 °C temperature reported in ref. 78. The bright-field TEM images (**Figures 2-5b,e**) reveal the morphology of the product to be ultrathin nanobelts with average lateral dimensions of 300 nm (width) and 4 um (length). The SAED pattern (**Figure 2-5h**) recorded along the [100] zone of Zn(Bim)OAc exhibits (0kl) reflections.

According to the SAED pattern, we determined the lateral dimensions of the nanobelt to correspond to the b and c axes of Zn(Bim)OAc.

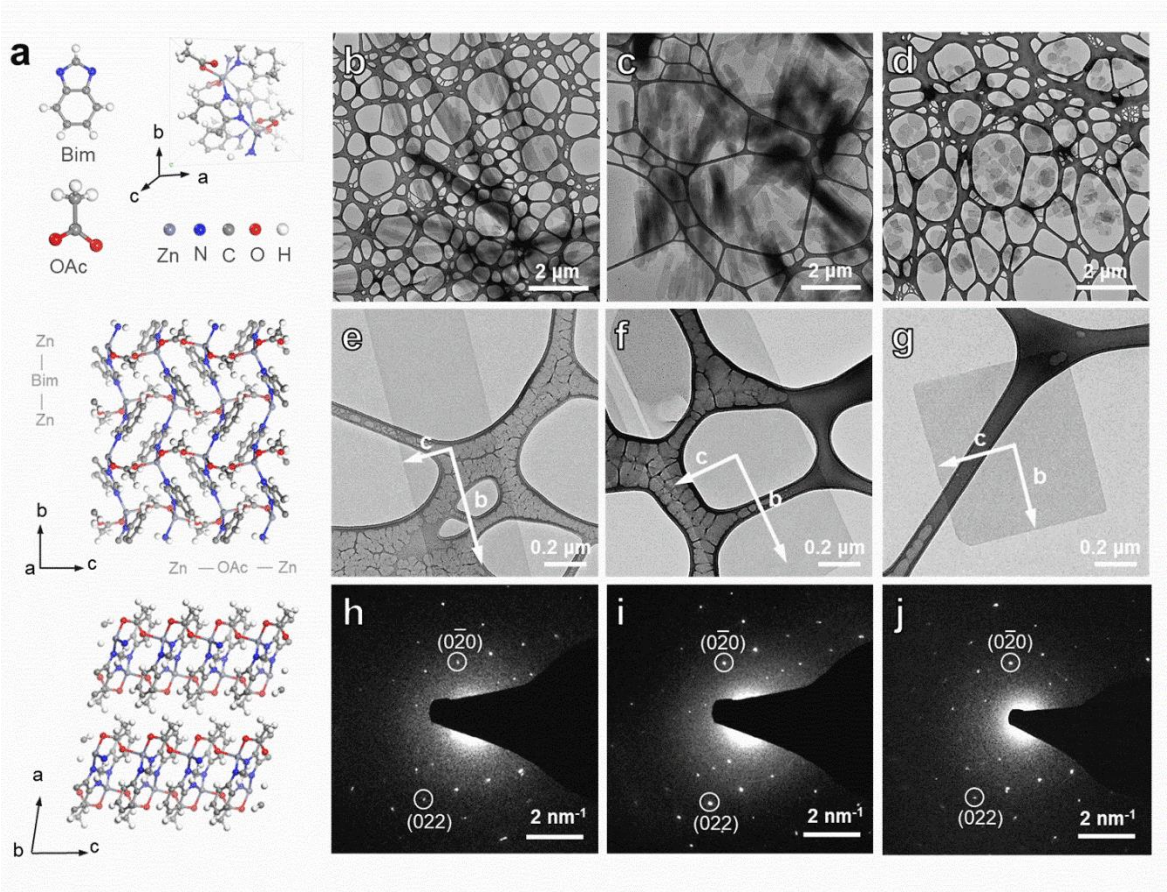

Figure 2-5. (a) Building units and the corresponding unit cell of Zn(Bim)OAc structure (top), 2D layers are viewed along the a axis (middle) and along the b axis (bottom). Structure of a single layer features Zn-Bim-Zn linkage along the b axis and Zn-OAc-Zn linkage along the c axis. TEM images of several nanocrystals, single nanocrystal and its corresponding electron diffraction pattern for synthesis of Zn(Bim)OAc structure at (b,e,h) 110 °C, (c,f,i) 60 °C and (d,g,j) 25 °C.

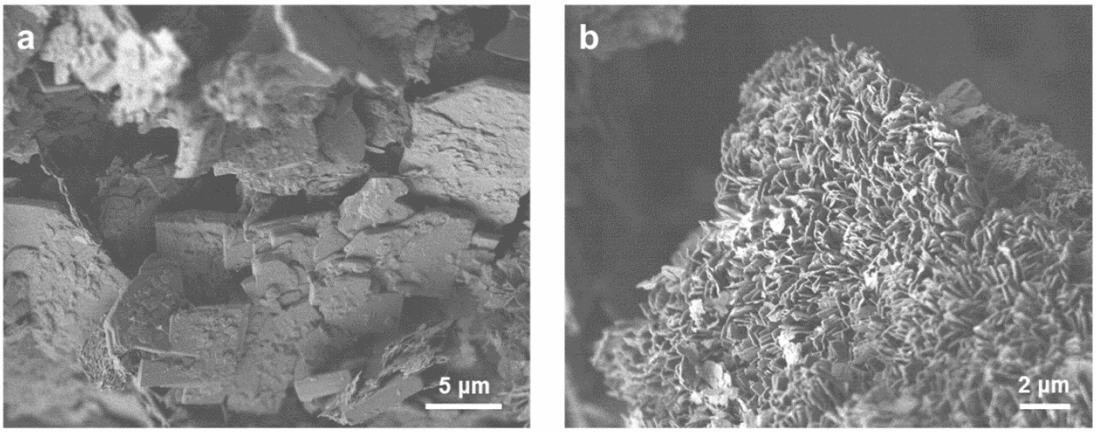

Figure 2-6. SEM images of Zn(Bim)OAc particles synthesized without CTAB.

It is known that temperature can affect the crystal growth rates and here we hypothesized that the growth rates along the Zn-Bim-Zn vs Zn-OAc-Zn chains could have different temperature dependence. Indeed, when the temperature was reduced, the thin nature of the product was retained while the ratio between the long and short lateral dimensions kept decreasing, with average ratio of 5.7 when synthesized at 60 °C (**Figures 2-5c,f**), and 1.3 when synthesized at room temperature (**Figures 2-5d,g**). To understand the temperature-dependent morphology change, we investigated its relationship with the crystal structure by SAED. As shown in **Figures 2-5e–j**, the long axis of the belt-like crystals was determined to be the b axis (Zn-Bim-Zn chain) of Zn(Bim)OAc, and the short axis of the belt-like crystals was determined to be the c axis (Zn-OAc-Zn chain) of Zn(Bim)OAc. Since the two axes correspond to two different linkages, the shape variation may result from the change in relative linker addition rate to metal center. At high temperature, the addition of benzimidazole to Zn center apparently happens much faster than the addition

of acetate to Zn center, resulting in nanobelt growing favorably along the b axis. With decreasing temperature, the addition rate of benzimidazole drops and becomes comparable to the addition rate of acetate at room temperature. As a result, ultrathin nanosheets with an average lateral dimension of 600 nm were successfully prepared at room temperature.

To determine the thickness of nanosheets, a high-angle annular dark-field scanning transmission electron microscopy (HAADF-STEM) based method was developed. Image intensity in a HAADF-STEM image is typically pro-portional to Z^{α}, (α = 1.3-2.0), where average Z is the atomic number of the specimen through which electron beam passes.[87, 89-91] Therefore, we utilized this inherent property of HAADF-STEM imaging to determine the thickness of a material with known composition by calibrating it with a standard material of known thickness and composition. For standard, we used the 3.2 nm-thick zeolite MFI nanosheets reported in ref. 77. **Figure 2-7a** shows the HAADF-STEM image of Zn(Bim)OAc (outlined in blue) and 3.2 nm-thick zeolite MFI nanosheets (outlined in red) deposited on an amorphous carbon support. HAADF intensity distributions from two different images (**Figure 2-8**) acquired under similar TEM conditions at 80 kV and 200 kV (**Figure 2-7b**) were obtained and analyzed. According to the calibration curves generated through HAADF-STEM simulation (**Figures 2-7c** and **2-9**), the intensity distribution of Zn(Bim)OAc nanosheets shown in **Figure 2-7b** was converted to the thickness distribution as shown in **Figure 2-7d**. Single Zn(Bim)OAc nanosheet displays a thickness of 7.0 nm ± 0.5 nm at 80 kV and 7.2 nm ± 1.7 nm at 200 kV, which corresponds to a stack of six to seven two-dimensional Zn(Bim)OAc layers. This result is consistent with the thickness measurement by atomic force microscopy (AFM), where the single layer nanosheet thickness is in the range of 7-9 nm (**Figure 2-10**).

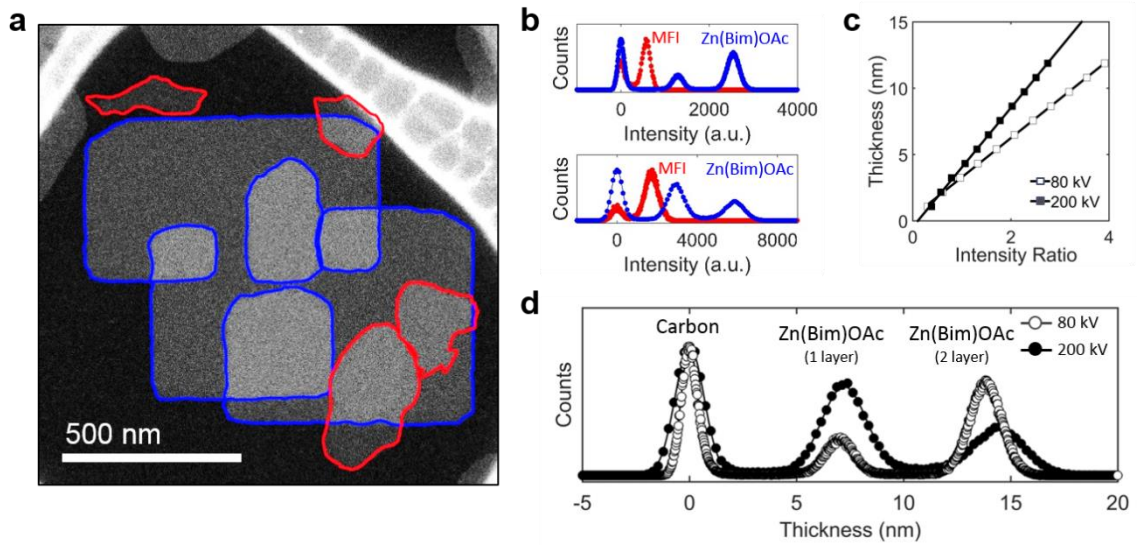

Figure 2-7. (a) HAADF-STEM image obtained at 80 kV of Zn(Bim)OAc nanosheet (outlined in blue) and 3.2 nm-thick 2D MFI (outlined in red) dispersed on an amorphous carbon support. (b) Intensity distribution in HAADF-STEM images of 3.2 nm-thick 2D MFI and Zn(Bim)OAc nanosheet acquired under similar TEM conditions at 80 kV (top) and 200 kV (bottom). (c) Calibration curves generated through HAADF-STEM simulation to convert intensity distribution in the image to thickness. (d) Intensity distribution of Zn(Bim)OAc nanosheet shown in panel b is converted to thickness distribution after applying the conversion shown in panel c. The single layer Zn(Bim)OAc nanosheet thickness is calculated to be 7.0 nm ± 0.5 nm at 80 kV and 7.2 nm ± 1.7 nm at 200 kV.

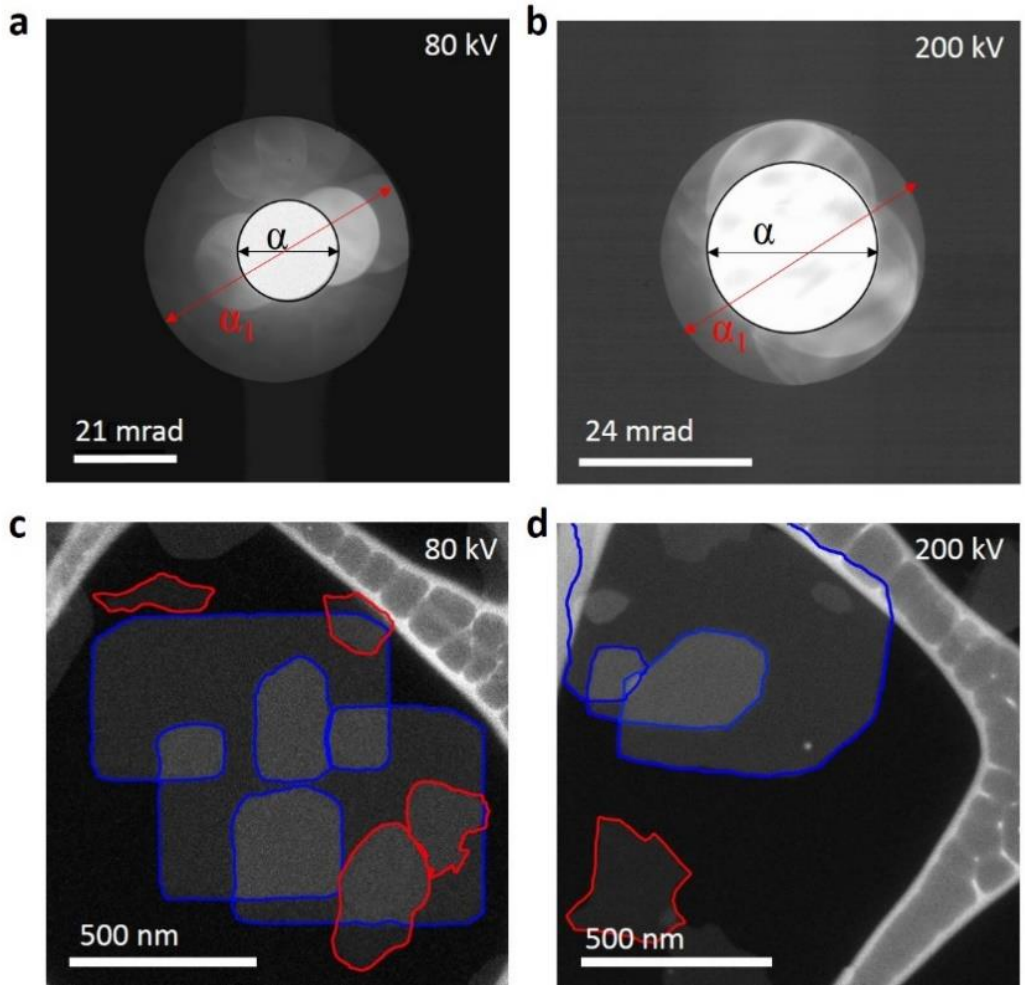

Figure 2-8. Annular dark field detector inner angle (α_I) measurement by imaging the shadow of the ADF-detector on CCD camera at (a) 80 kV and (b) 200 kV. The beam convergence angles were α = 21 mrad, 24 mrad respectively. HAADF-STEM images of MFI nanosheet (red) and Zn(Bim)OAc (blue) recorded at 80 kV (c) and 200 kV (d). Imaging parameters are listed in Table 2-1.

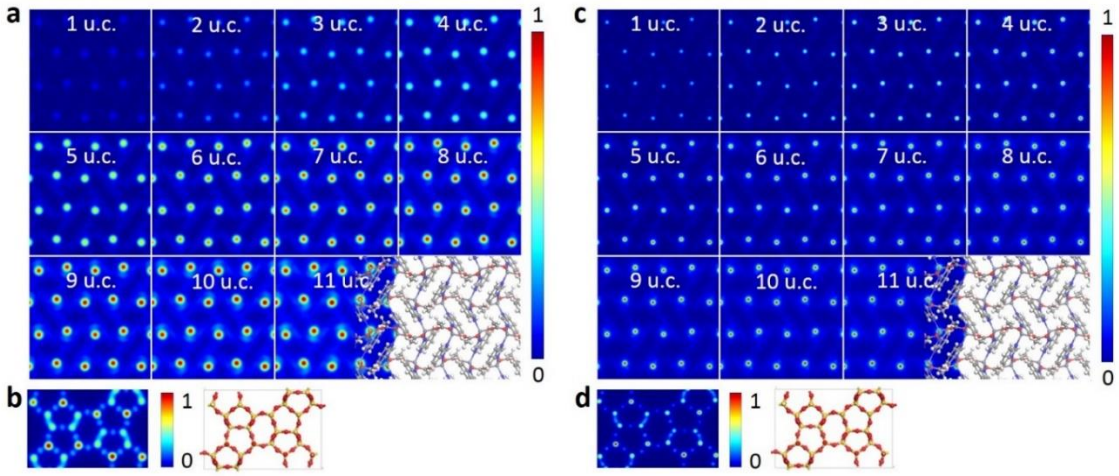

Figure 2-9. Simulated HAADF-STEM images of 1-11 unit cell (u.c.) thick Zn(Bim)OAc nanosheets viewed along *a*-direction with (a) 80 kV and, (c) 200 kV electron beams. The corresponding atomic models are overlaid for clarity. (b,d) Simulated HAADF-STEM image of a 1.5 u.c. (3.2 nm) thick MFI nanosheet viewed along b-direction, under the same 80 kV and 200 kV imaging conditions, respectively. Images of Zn(Bim)OAc nanosheets have been color-mapped with maximum intensity in the simulated image sequence for 1-11 u.c. thickness is 1 and minimum is 0. MFI images have been scaled individually according to the same colormap to enhance visibility. Lattice parameters of Zn(Bim)OAc unit cell used for simulation were: a = 10.818 Å, b = 9.837 Å, c = 8.821 Å, $\alpha = 90^o$, $\beta = 98.938^o$, $\gamma = 90^o$. Lattice parameters of MFI unit cell used for simulation were: a = 20.022 Å, b = 19.899 Å, c = 13.383 Å, $\alpha = 90^o$, $\beta = 90^o$, $\gamma = 90^o$.

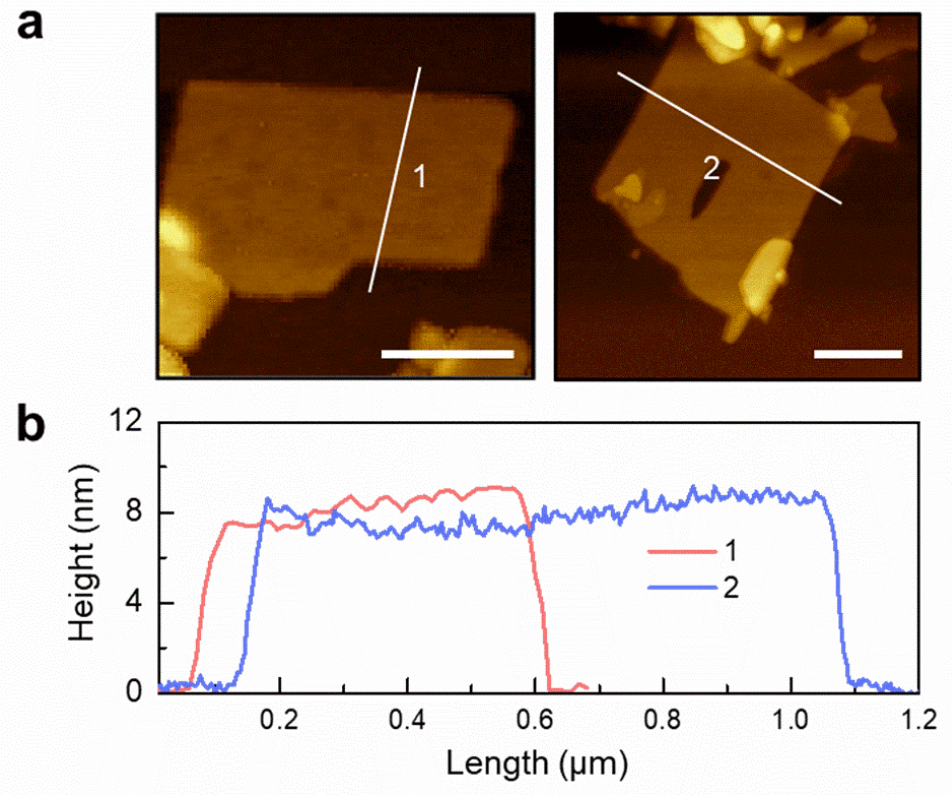

Figure 2-10. (a) AFM images of nanosheets deposited on Si wafer and (b) the corresponding height profiles. Scale bars in (a) are 400 nm.

In order to further study the crystal structure of nanosheets, XRD measurements were performed. The powder X-ray diffraction pattern (PXRD, **Figure 2-11**) confirms the presence of Zn(Bim)OAc in the sample, as the high-angle peaks ($2\theta > 11°$) match the simulated pattern of Zn(Bim)OAc based on the structure reported in ref. 80. However, the peak positions are shifted to lower angles. Moreover, in the low-angle region ($2\theta < 11°$), two intense peaks as well as several small peaks appear, which do not correspond to the reported structure of Zn(Bim)OAc in ref. 80. These peaks were also reported in ref. 78 and were attributed to a lamellar structure with a lattice period of around 8 nm. Within the

lamellar structure, CTAB is sandwiched between the stacked nanosheets at periodic locations.[78] As described next, we identified calcination conditions that remove the surfactant and the resulting material exhibits XRD pattern in close agreement with CTAB-free Zn(Bim)OAc.

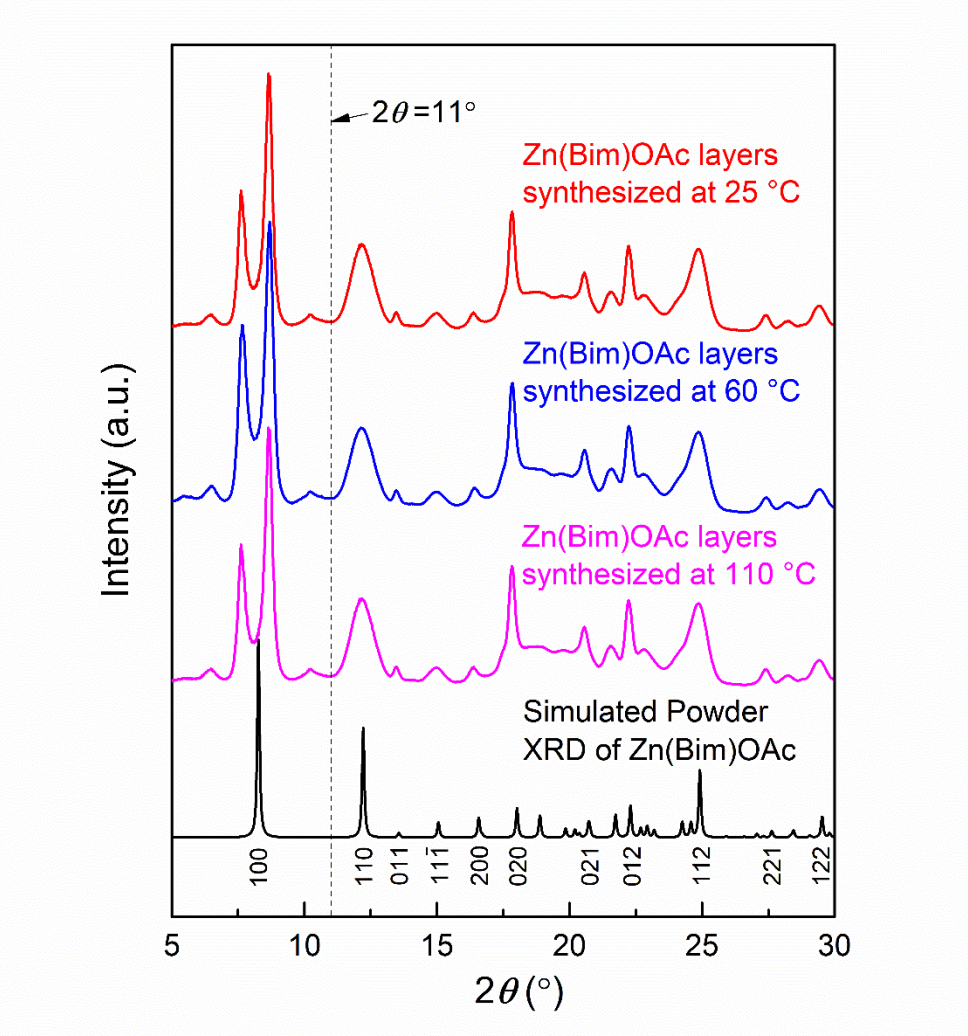

Figure 2-11. Synchrotron powder XRD pattern of Zn(Bim)OAc synthesized with CTAB at 25 °C, 60 °C, 110 °C and simulated powder XRD pattern of Zn(Bim)OAc (based on the structure reported in ref. 80). At 2θ > ~11°, there is qualitative agreement between the experimental data and the simulated XRD pattern, with the former being shifted to smaller angles. At 2θ < ~11°, there is no agreement with simulations as discussed in the main text and ref. 78.

Because the surfactant may block transport of molecules in membrane applications, it is desirable to have it removed. To identify conditions to remove CTAB without altering the structure of Zn(Bim)OAc, thermogravimetric analysis (TGA) was performed. As shown in **Figure 2-12**, pure Zn(Bim)OAc (made without using CTAB) shows a sharp weight loss at temperatures higher than 400 °C whereas the nanosheets made with CTAB experience a gradual weight loss from 230 °C before a sharp weight loss takes place at 400 °C. Considering that the weight loss of pure CTAB happens at similar temperature (it starts at about 200 °C and reaches 95% at 330 °C), the initial gradual weight loss in as-synthesized nanosheets could be attributed to the decomposition of CTAB. Because the loss of CTAB appears to start before the decomposition of Zn(Bim)OAc, heat treatment for CTAB removal was attempted by holding the temperature at 325 °C under air flow for 15 h (**Figure 2-12b**). After the heat treatment, XRD of the product (**Figure 2-12c**) showed exclusively reflections from Zn(Bim)OAc. The peak broadening of (100) and (200) of nanosheet sample relative to its bulk counterpart confirms its thin nature. The additional peaks which do not correspond to Zn(Bim)OAc structure disappeared. This observation is consistent with the assignment of the extra XRD peaks in ref. 78 to the presence of CTAB and indicates that the structure of Zn(Bim)OAc was retained while most of surfactant molecules were removed after the heat treatment, though a small amount of their counterion bromine was detected by energy-dispersive X-ray spectroscopy (EDS) (**Table 2-3**). To further confirm the CTAB removal, the residue weight percent of heat-treated nanosheets after full calcination to 700 °C was estimated, and compared with the residue mass acquired from TGA of CTAB-containing nanosheets. By assuming no surfactant presence in heat-treated nanosheets, a residue weight percent of 27.3% was calculated,

which compares well with the 26.8% residue obtained from TGA (calculation is shown in **section 2.2.10**).

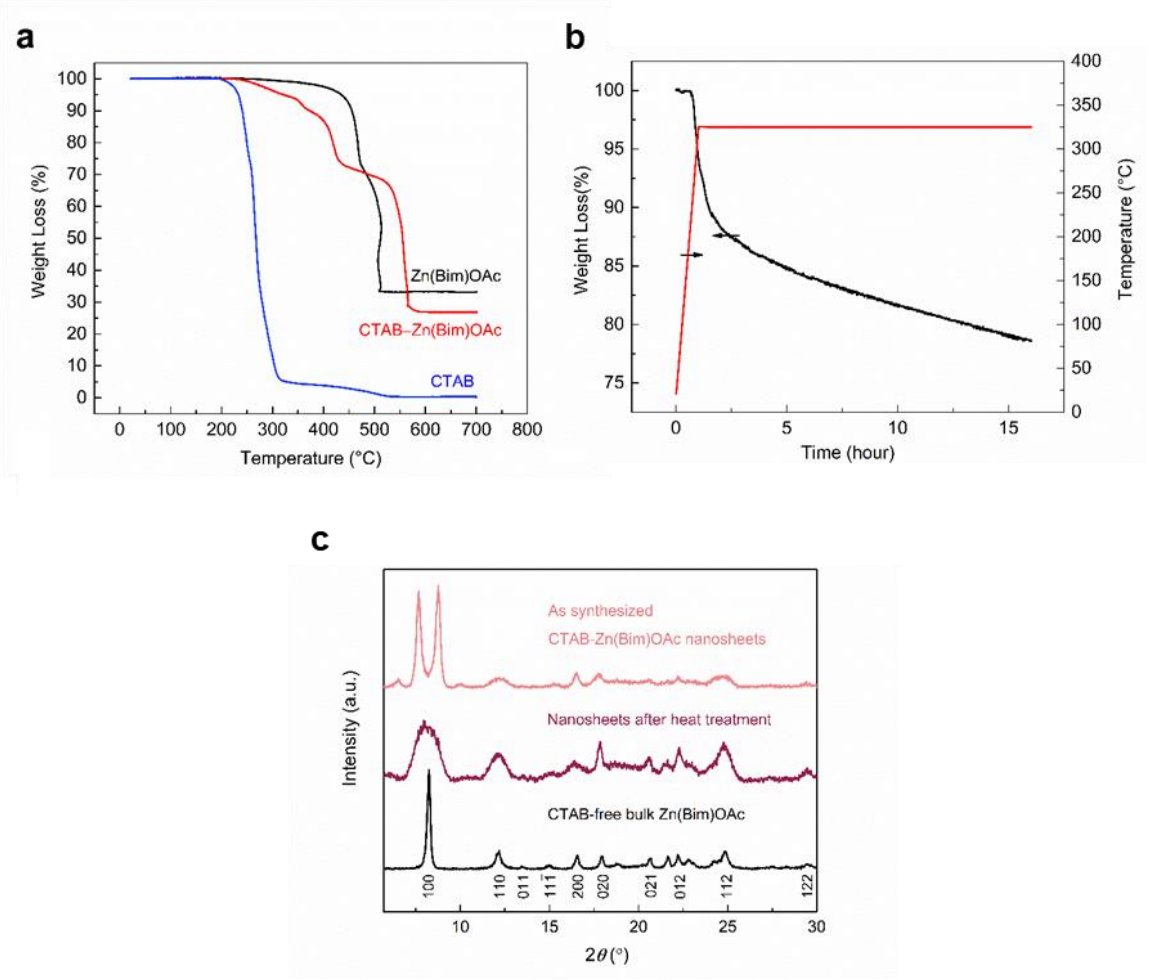

Figure 2-12. (a) Weight loss vs. temperature curves obtained by thermogravimetric analysis (TGA) of CTAB-free Zn(Bim)OAc, CTAB and CTAB-containing Zn(Bim)OAc nanosheets. (b) Temperature and weight loss vs. time from TGA indicating CTAB removal at 325 °C. (c) XRD of nanosheets before and after heat treatment at 325 °C and powder XRD of CTAB-free Zn(Bim)OAc.

Table 2-3. Bromine analysis using EDS

Sample	Before heat treatment	After heat treatment
Br/Zn (at%/at%) [a]	0.10 ± 0.02	0.06 ± 0.01

[a] Error is given as the standard deviation from 3 measurements at different sites.

The orientation of nanosheets, which determines the orientation of pore system with respect to the direction of permeate flow, is critical to the separation efficiency of nanosheet-based membranes. To demonstrate preferentially oriented coatings of Zn(Bim)OAc, we used Si wafers and a stamping method.[49, 82-84] As illustrated in **Figure 2-13a**, the nanosheets dispersed in tetrahydrofuran (THF) were transferred to the air–water interface by applying small quantities of the suspension dropwise onto the water surface. THF dissolved in water or evaporated, leading to nanosheets spreading on the surface of water. The nanosheets were introduced to Si wafer by Langmuir–Schaefer type transfer and the obtained coating was characterized by SEM and synchrotron in-plane XRD. **Figure 2-13b** shows a typical SEM image of the coating indicating that nanosheets lie flat on the substrate. The in-plane XRD of the coating (**Figure 2-13c**) shows exclusively reflections from (0kl) crystallographic planes of Zn(Bim)OAc, indicative of the preferentially a-out-of-plane orientation.

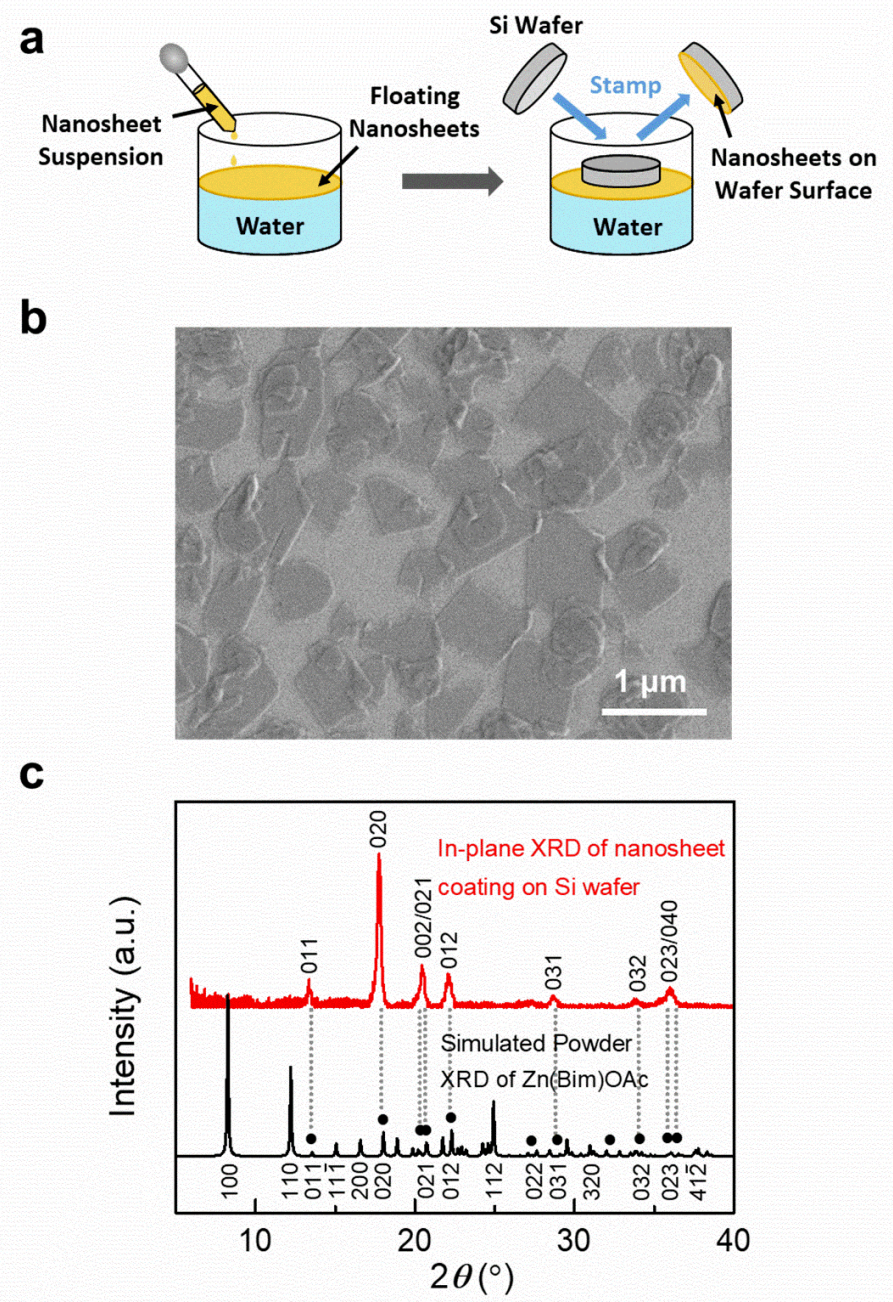

Figure 2-13. (a) Schematic of nanosheet coating process via stamping. (b) SEM image of nanosheet coating obtained by the stamping process. (c) In-plane XRD pattern of nanosheet coating on Si wafer (top) and simulated powder XRD pattern of Zn(Bim)OAc (bottom). The (0kl) peaks are marked with dots in the simulated pattern.

2.4 Conclusion

In summary, we show that direct synthesis is more desirable to prepare high-quality MOF nanosheets compared to exfoliation. We demonstrate that changing crystallization temperature can lead to direct synthesis of Zn(Bim)OAc nanosheets. Using HAADF-STEM, the thickness of Zn(Bim)OAc nanosheet was determined to be 7 nm. Moreover, we identify a temperature window allowing to remove the CTAB surfactant associated with Zn(Bim)OAc layers and show that Zn(Bim)OAc nanosheets can be transferred from an air–water inter-face to form an oriented coating on Si wafer. The obtained nanosheets with high aspect ratio and uniform thickness may open new opportunities for their application as gas separation membranes and their synthesis approach holds promise to be extended to other MOF structures to realize tunable porosity and functionality of MOF nanosheets.

Chapter 3: Fabrication of membranes based on Zn(Bim)OAc nanosheets

3.1 Introduction

The general fabrication of nanosheet-based membranes, as shown in **Figure 1-3**, includes three steps: 1) the preparation of pure uniform nanosheet suspension, 2) the oriented deposition of nanosheets onto porous supports and 3) the formation of a continuous membrane by secondary growth to seal all the interparticle gaps. High aspect ratio Zn(Bim)OAc MOF nanosheets with uniform thickness have been developed in Chapter 2, which completes the first step in membrane fabrication. In order to achieve Zn(Bim)OAc nanosheet-based membranes, it is crucial to study the deposition, adhesion and the growth of the MOF nanosheets on porous supports. However, it remains challenging due to the poor interaction between the MOFs and the porous supports.

A couple of studies in the literature have focused on the deposition and growth of nanosheets onto porous supports. Zeolite nanosheets were transferred to α-Al_2O_3 porous supports by vacuum filtration and then intergrown by a hydrothermal treatment to form high performance p-/o-xylene selective membranes.[77] For MOF nanosheets, Peng et al. prepared $Zn_2(Bim)_4$ and $Zn_2(Bim)_3(OH)(H_2O)$ (Bim=benzimidazole) nanosheets via exfoliation and deposited the nanosheets onto porous α-Al_2O_3 porous supports by a hot-drop coating method, where nanosheet suspension was deposited dropwise onto the surface of the support which was heated at elevated temperatures.[26, 55] The resulting coatings were several nanometers thick and demonstrated a remarkable H_2/CO_2 performance. Using a similar method, Wang et al. deposited MAMS-1 MOF nanosheets onto anodic aluminum oxide (AAO) porous supports and obtained H_2/CO_2 selective membranes.[76] In addition, a

graphene oxide (GO)-assisted vacuum filtration deposition method was used to enhance the adhesion and repair the defect of Cu(BDC) (BDC^{2-} = 1,4-benzenedicarboxylate) nanosheet-based membranes, leading to a good H_2/CO_2 separation performance.[92] These studies follow the general three-step (or the two-step omitting the third secondary growth step) method in preparing the nanosheet-based membranes and the resultant membrane performance is highly dependent on the nanosheet-support interaction, which differs between different structure types of nanosheets.

Recently, alternative methods of transforming the pre-deposited solid-state metal-based precursor into ultrathin MOF membranes have been demonstrated as a feasible way to enhance the membrane adhesion and confine the MOF nucleation and growth in a thin layer for different MOF structures. Li et al. reported that a thin layer of Zn-based gel on the support surface was able to be directly transformed into a 17 nm-thick ZIF-8 membrane under ligand vapor treatment.[46] The thinness of the membrane was attributed to the confined growth on the membrane surface under vapor processing conditions. Using a similar method, Nian et al. converted a thin layer of Co-based gel on the GO-modified porous substrate into a 57 nm-thick $Co_2(Bim)_4$ nanosheet laminated membrane under the vapor phase treatment of ligand benzimidazole.[93] In addition, Li et al. reported the direct growth of $Zn_2(Bim)_4$ nanosheet membranes by self-conversion of pre-deposited ZnO nanoparticles with the assistance of ammonia and GO.[94-95] The resulting nanosheet membranes are selective to H_2/CO_2 with a membrane thickness of 50 ~ 200 nm. Ma and Tsapatsis et al. deposited ultrathin ZnO inside the γ-Al_2O_3 support and transform it into a 200 nm-thick ZIF film by ligand vapor treatment.[47] As a result, the membrane demonstrates good adhesion with the support and a stable propylene/propane separation

performance under feed gas pressure up to 7 bar. For these membranes, metal-based gel and ZnO have been used as the solid-state metal-based precursor. The use of MOF nanosheets as the transformation precursor, which offers good control over the deposit thickness on top of the support surface, has not been reported.

In this chapter, Zn(Bim)OAc MOF nanosheets are used as building blocks for membrane fabrication. The coatings of Zn(Bim)OAc MOF nanosheets onto porous supports are prepared and subsequently tested for gas permeation. Furthermore, the use of a Zn(Bim)OAc MOF nanosheet coating as a metal-based precursor for forming membranes is explored, leading to the fabrication of propylene/propane selective membranes.

3.2 Experimental

3.2.1 Preparation of Zn(Bim)OAc nanosheet coating

To purify nanosheets, about 80% of top Zn(Bim)OAc nanosheet suspension in tetrahydrofuran (THF) was collected after two-week sedimentation and centrifuged 4 times at 7500 RCF for 15 min. The cake was collected and re-dispersed in THF to form the purified nanosheet suspension. 2 ml of the purified nanosheet suspension was collected and then diluted with 4 ml of THF. The resulting suspension was sonicated (Branson 5510R-DTH ultrasonic cleaner) for 15 min and then used as Zn(Bim)OAc nanosheet coating sol.

α-Al_2O_3 porous supports were prepared by a slip casting method developed by Tsapatsis group.[96] γ-Al_2O_3 supports were prepared on the surface of α-Al_2O_3 supports by a sol-gel method reported before.[97] 1 M boehmite sol was prepared and mixed with 3 wt% polyvinyl alcohol (PVA) solution to use as coating sol. The γ-Al_2O_3 sol was then coated on the surface of α-Al_2O_3 porous support by a slip casting method, followed by overnight

drying at room temperature, and calcination at 450 °C for 3 h with a heating and cooling rate of 0.5 °C/min.

6 ml of the Zn(Bim)OAc nanosheet coating sol was deposited on the α-Al_2O_3 porous support or the γ-Al_2O_3 support by vacuum filtration to form the Zn(Bim)OAc nanosheet coating.

3.2.2 Membrane fabrication

Prior to membrane fabrication, the surface of γ-Al_2O_3 supports was modified with ultrathin ZnO by atomic layer deposition (ALD). The supports were placed horizontally inside the ALD chamber (Savannah series from Cambridge NanoTech) at 125 °C with the γ-Al_2O_3 side facing upward. For one cycle, the supports are exposed to 0.015 s water vapor, 5 s vacuum purge, 0.015 s diethylzinc vapor and 5 s vacuum purge. 5 cycles of deposition were carried out in total. The ZnO modified γ-Al_2O_3 support was then coated with Zn(Bim)OAc nanosheets by vacuum filtration as described in **Section 3.2.1** and dried at room temperature overnight. The nanosheet-coated support was then placed vertically in a Teflon liner with 0.2 g solid 2-methylimidazole (mIm) at the bottom. The liner was sealed and heated at 125 °C for 24 h for the ligand vapor treatment. After the treatment, the membrane was activated at 80 - 100 °C for 16 h under vacuum. The reference membranes were prepared in the same way except omitting the surface modification step or the nanosheet coating step.

3.2.3 Characterization

X-ray diffraction (XRD) pattern was recorded using a Bruker-AXS (Siemens) D5005 diffractometer with a CuKα radiation source. Scanning electron microscopy (SEM) images were acquired using a Hitachi SU8230 or JEOL 6700 scanning electron microscope

operated at 1.5 kV. The membrane cross-section for SEM imaging was prepared by Focused-ion-beam milling with a FEI Quanta 200 3D.

3.2.4 Gas permeation test

Single gas permeation tests of helium, hydrogen, nitrogen, carbon dioxide and propylene were carried out in a home-built constant volume variable pressure apparatus. The membrane was sealed tightly with O-rings inside a stainless-steel permeation cell. The cell was loaded into the apparatus with the feed side introduced with pure atmospheric pressure gas at room temperature and the permeate side initially maintained under vacuum. During the measurement, the rate of pressure change on the permeate side was used for permeance calculation. The ideal selectivity was determined to be the permeance ratio of the two gases. The mixed gas propylene/propane permeation measurements were performed in the Wicke-Kallenbach mode. Typically, 10 sccm equimolar propylene/propane gases at atmospheric pressure were introduced to the membrane side. 10 sccm argon at atmospheric pressure was introduced to the permeate side as sweep gas to carry the permeating gas to an attached gas chromatograph (Shimadzu, GC 2014). The composition of permeating gas was determined via gas chromatography equipped with a flame ionization detector (FID) and a capillary column. The selectivity was determined to be the permeance ratio of the two components.

3.3. Results and discussion

3.3.1 Deposition of Zn(Bim)OAc MOF nanosheets on porous supports

To deposit Zn(Bim)OAc MOF nanosheets, conventional α-Al_2O_3 porous supports and vacuum filtration technique which allows quantitative nanosheet transfer were first attempted. As shown in **Figure 3-1a**, the pore size of the α-Al_2O_3 support is smaller than

400 nm, which allows the penetration of the solvent while keeping the nanosheets (lateral dimension of ~600 nm) lying flat on the surface during the vacuum filtration process. The coating quality after the vacuum filtration is examined by SEM. As shown in **Figure 3-1b**, the coating is not uniform with some area covered with thick deposits while other area remaining uncovered. This is due to the unfavorable interaction between the nanosheet and support surface such that the nanosheets prefer to stay in the suspension rather than on the support surface during the filtration process. To address this issue, the support surface was tuned from α-Al_2O_3 to a layer of γ-Al_2O_3 by dip coating. **Figure 3-1c** shows the SEM image of the top surface of the γ-Al_2O_3 layer. It has a much smaller pore size of 2-5 nm and surface roughness compared to that of the α-Al_2O_3.[97] In addition, the surface is abundant of hydroxyl groups, making it highly hydrophilic.[98] **Figure 3-1d** demonstrates the oriented and uniform nanosheet coating on the γ-Al_2O_3 support, indicating the favorable interaction between the Zn(Bim)OAc nanosheet and γ-Al_2O_3.

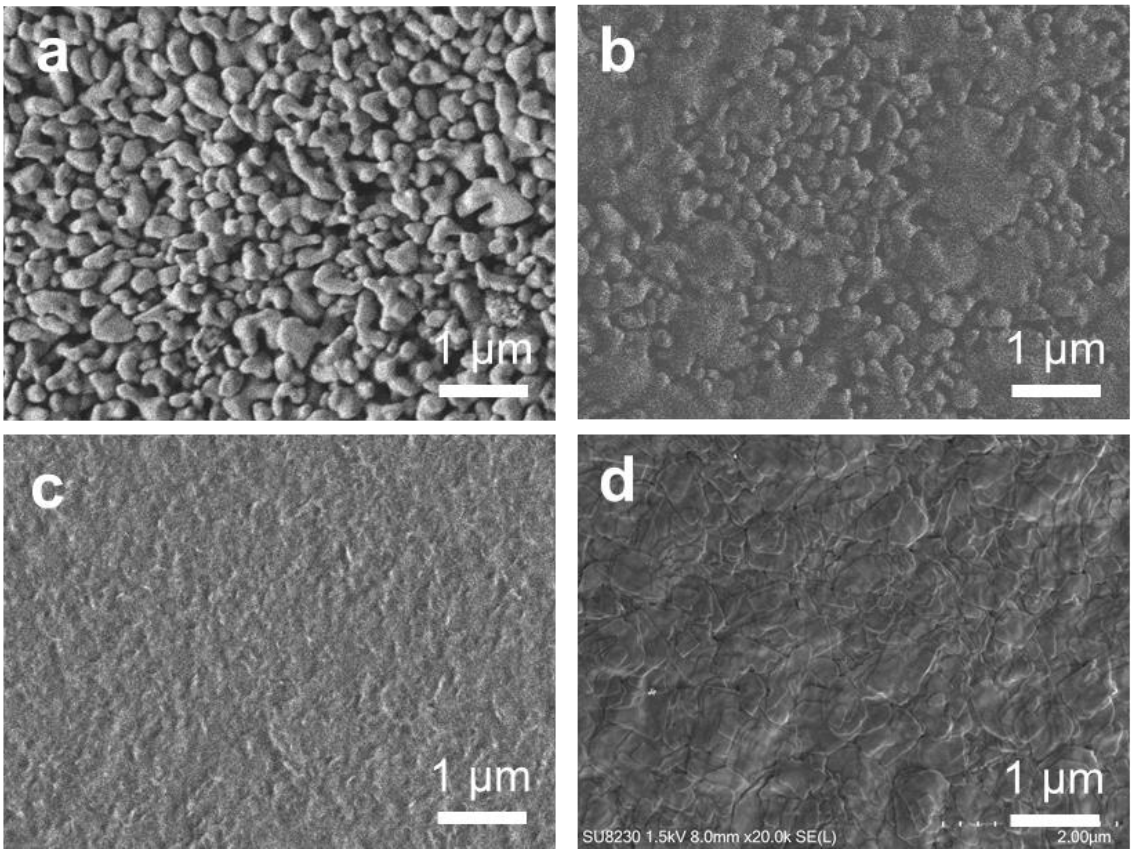

Figure 3-1. Top view SEM images of (a) bare α-Al_2O_3 support and (b) Zn(Bim)OAc nanosheet coating on α-Al_2O_3 support, (c) bare γ-Al_2O_3 support and (d) Zn(Bim)OAc nanosheet coating on γ-Al_2O_3 support.

The single gas permeation test for He, H_2, CO_2 and N_2 under a feed pressure of 1 bar at room temperature was performed to the as-formed nanosheet coating on the γ-Al_2O_3 support. As shown in **Figure 3-2a**, the coating demonstrates a He permeance of 1.1 $\times 10^{-8}$ mol m^{-2} s^{-1} Pa^{-1} and a H_2 permeance of 1.3 $\times 10^{-8}$ mol m^{-2} s^{-1} Pa^{-1}, which are at least two orders of magnitude lower than the bare γ-Al_2O_3 support (the propylene permeance of the bare γ-Al_2O_3 support is 1.1 $\times 10^{-6}$ mol m^{-2} s^{-1} Pa^{-1}), indicating the complete coverage of the

nanosheets on the support. In addition, as depicted in **Figure 3-2b**, the ideal selectivity is close to the Knudsen selectivity. For example, the H_2/N_2 ideal selectivity is 3.5 and Knudsen selectivity is 3.7, and the He/N_2 ideal selectivity is 2.8 and Knudsen selectivity is 2.6. This suggests the existence of gas-leakage channels which are likely to come from the interparticle gaps. Overall, the low permeance and low selectivity indicate that the intrinsic pore size of the nanosheet is smaller than the diameter of the smallest gas He (2.6 Å) and the direct deposits has gas-leakage channels.

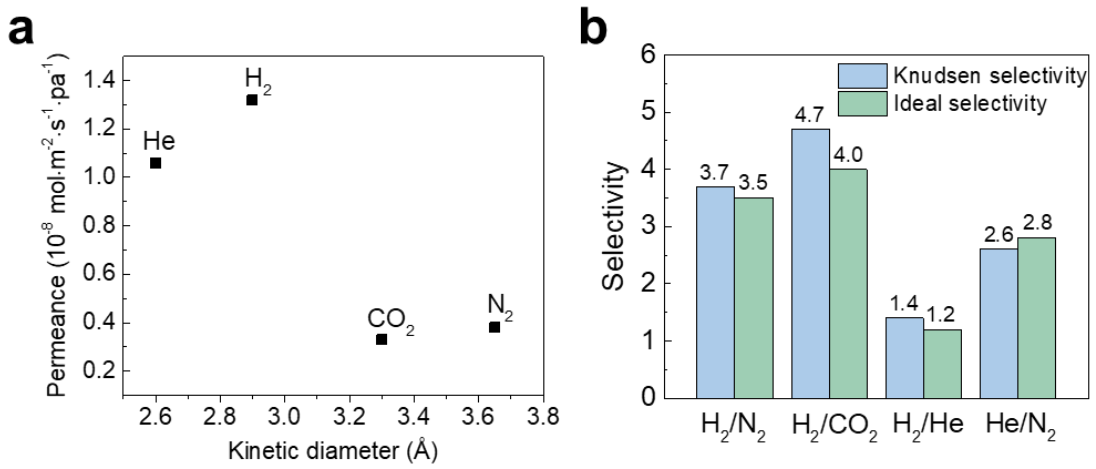

Figure 3-2. Single gas permeation data for Zn(Bim)OAc nanosheet coating on the γ-Al_2O_3 support, showing (a) permeance and (b) ideal selectivity in comparison to Knudsen selectivity

3.3.2 Formation of ZIF-8 membranes by transformation of Zn(Bim)OAc MOF nanosheet coatings

Since the direct deposition of the Zn(Bim)OAc nanosheets onto the porous support results in low-permeance and selectivity coatings, methods to increase the pore size of the layer while healing the interparticle defects were explored to realize selective membranes.

Uniform and oriented MOF nanosheet coatings offer good control over the deposition thickness and a confined layer of metal center, which are desirable to use as the solid-state metal-based precursor to form ultrathin MOF membranes. Furthermore, the use of ligand vapor to transform the nanosheet coatings into continuous membranes is beneficial for forming MOF with a different structure and maintaining thin morphology, as the mobility for metal ions is significantly inhibited without a solvent. Therefore, 2-methylimidazole (mIm) ligand vapor was selected to treat the Zn(Bim)OAc nanosheet coatings aiming to transform the nanosheet coatings into ZIF-8 membranes, as ZIF-8 with a proper pore structure for propylene/propane separation has been demonstrated to be easily formed from zinc-based solid precursors and mIm vapor at a relatively low temperature in previous studies.[45-47]

The mIm vapor was first supplied to Zn(Bim)OAc nanosheet coatings supported on the bare γ-Al_2O_3. Cross-sectional SEM image of the membrane (**Figure 3-3**) demonstrates that there are gaps between the transformed membrane layer and the γ-Al_2O_3 support, indicating the poor membrane-substrate adhesion. In order to improve the adhesion, 5 cycles of ZnO is deposited to the γ-Al_2O_3 support by atomic layer deposition (ALD) for support surface modification. The surface hydroxyl groups of the γ-Al_2O_3 support react with the precursor diethylzinc and water vapor in ALD, forming ZnO with good adhesion with the support. In addition, 5 cycles of ZnO is less than 1 nm in thickness, which does not impact the gas permeation properties of the support, as the propylene permeances for the 5 cycles of ZnO modified support and the unmodified support are both 1.1 $\times 10^{-6}$ mol m^{-2} s^{-1} Pa^{-1}. Therefore, the vacuum filtration of Zn(Bim)OAc nanosheet suspension could still be carried out on the modified support.

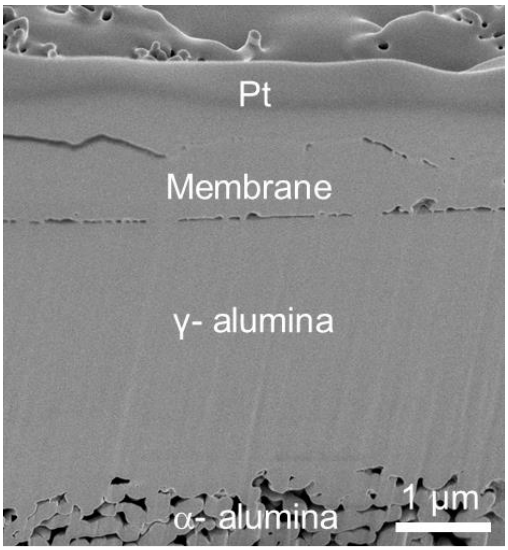

Figure 3-3. Cross-sectional SEM image of Zn(Bim)OAc-converted membrane on an unmodified γ-Al_2O_3 support showing the poor adhesion between the membrane layer and the support.

The schematics of the nanosheet-based membrane fabrication process are shown in **Figure 3-4**. The nanosheet coating on ZnO-modified support is treated with mIm vapor at 125 °C for 24 h, followed by vacuum activation at 100 °C overnight to remove the unreacted ligand. The XRD of the membrane in **Figure 3-5a** shows peaks from ZIF-8 crystal structure and underlying α-Al_2O_3 substrate, suggesting the complete conversion of Zn(Bim)OAc into ZIF-8. Top view of the membrane surface (**Figure 3-5b**) shows that ZIF-8 crystals are intergrown with a morphology favoring flat crystals, which is beneficial for forming thin layer. Examination of the membrane cross section (**Figure 3-5c**) confirms the small membrane thickness of around 100 nm and demonstrates good adhesion between the membrane and the support.

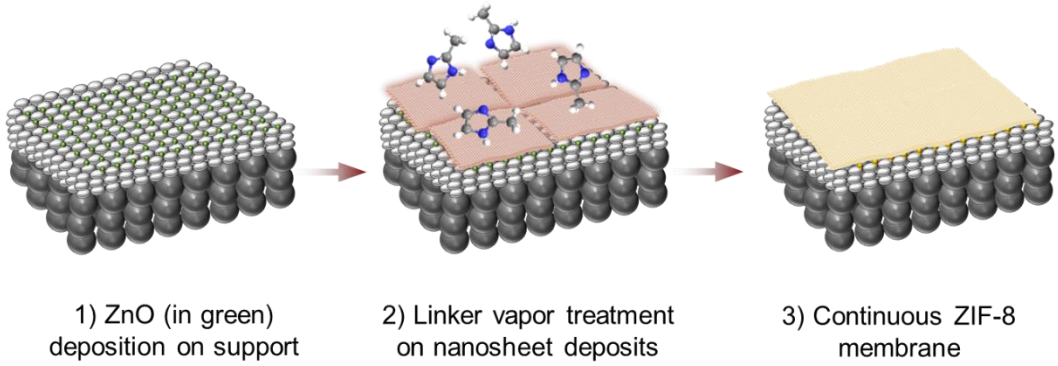

Figure 3-4. Schematics of the process in fabricating ZIF-8 membranes based on the transformation of Zn(Bim)OAc nanosheets

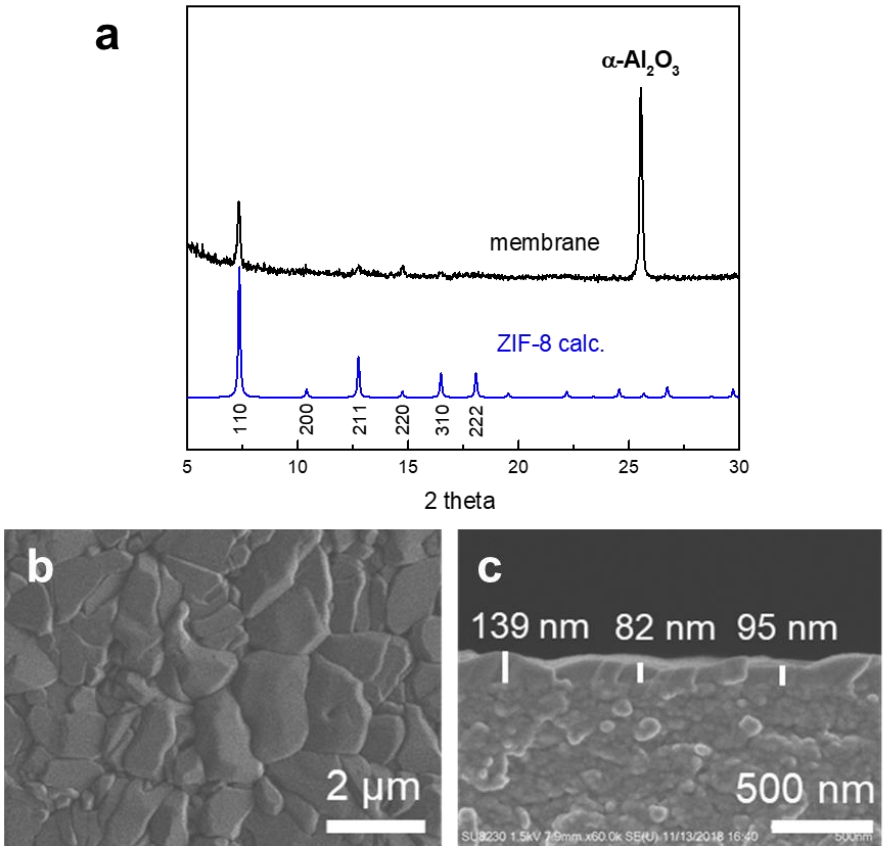

Figure 3-5. (a) Top view and (b) cross-sectional view SEM images and (c) XRD pattern of the Zn(Bim)OAc nanosheets-converted membrane.

The separation performance of membranes was evaluated by conducting 50/50 propylene/propane binary gas permeation measurement in a Wicke-Kallenbach setup at room temperature (~22 °C). As shown in **Figure 3-6**, Zn(Bim)OAc nanosheet coating on the unmodified γ-Al_2O_3 support displays a propylene permeance of 1.3 $\times 10^{-9}$ mol m^{-2} s^{-1} Pa^{-1} with a propylene/propane selectivity of 1. After ALD surface modification and ligand vapor treatment, the ZIF-8 membrane shows a 2-fold increase in permeance and 15 times increase in selectivity, with an average propylene permeance of 3.4 $\times 10^{-9}$ mol m^{-2} s^{-1} Pa^{-1} and a propylene/propane selectivity of 16. This is attributed to the proper pore structure formed within the converted continuous membrane layer for propylene/propane separation and strong adhesion to the substrate. In comparison, the membranes fabricated without 5 cycles of ZnO surface modification (shown as the purple data point in **Figure 3-6**) or without Zn(Bim)OAc nanosheet coatings (shown as the orange data point in **Figure 3-6**) demonstrate separation performance close to that of the bare support (propylene permeance of 1.1 $\times 10^{-6}$ mol m^{-2} s^{-1} Pa^{-1} with propylene/propane selectivity of 1), due to the poor membrane-substrate adhesion or insufficient Zn precursor to form a continuous film, respectively. Therefore, each step of support surface modification, nanosheet coating and ligand vapor treatment in the fabrication process as shown in **Figure 3-4** is important in forming functional membranes.

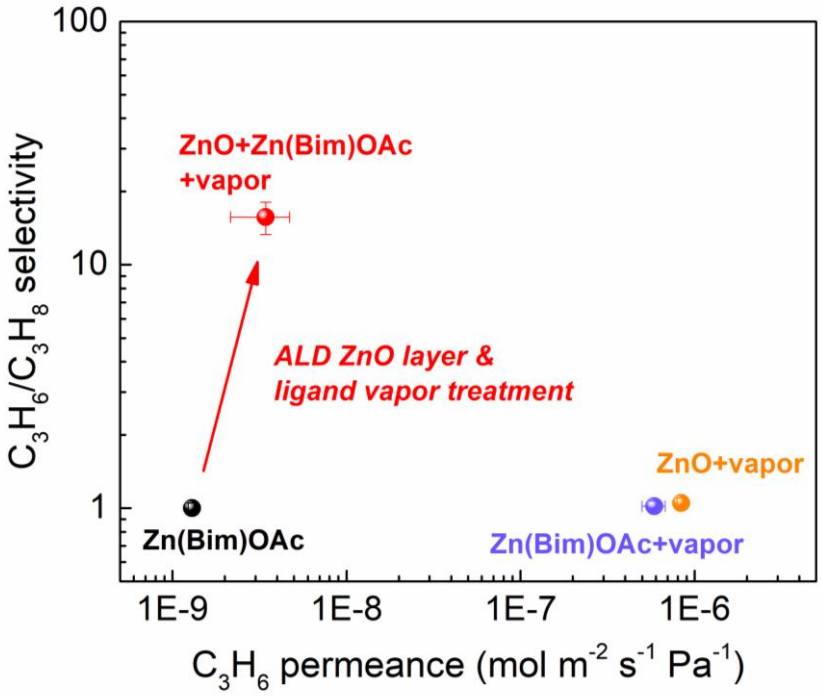

Figure 3-6. Propylene/propane mixed gas separation performance plot operated at feed pressure of 1 bar at room temperature for different membranes: Zn(Bim)OAc coating (black), Zn(Bim)OAc coating with 2-methylimidazole vapor treatment (purple), 5-cycle ALD ZnO with 2-methylimidazole vapor treatment (orange) and 5-cycle ALD ZnO coated with Zn(Bim)OAc nanosheets followed by 2-methylimidazole vapor treatment (red).

3.4 Conclusion

In summary, uniform and oriented Zn(Bim)OAc nanosheet coatings are successfully prepared on porous γ-Al_2O_3 supports by vacuum filtration. The permeation data for He, H_2, N_2, CO_2 show a significant permeance drop compared with bare supports and separation selectivity close to Knudsen selectivity, indicating that the gas molecules travel through the interparticle gaps while the nanosheets are not permeable for the gas molecules.

Modification of the γ-Al_2O_3 support surface with 5 cycles of ZnO by ALD and treatment of the nanosheet coatings with 2-methylimidazole ligand vapor result in the formation of thin ZIF-8 membranes as evidenced by SEM imaging and XRD. The mixed gas propylene/propane separation performance shows a 15 times improvement in selectivity for the converted ZIF-8 membranes compared with Zn(Bim)OAc nanosheet coatings without treatment. This method of using MOF nanosheets as metal precursor and ligand vapor treatment to form thin membranes on top of the substrate, combined with ZnO surface modification by ALD to enhance the membrane adhesion, is promising to be versatile to form ultrathin membranes with other MOF nanosheets and ligand vapor molecules.

Chapter 4: Mixed matrix membranes with Cu(BDC) MOF nanosheets for CO_2 separation

4.1 Introduction

To mitigate global warming caused by the rapid increase in CO_2 emissions in recent decades, significant research efforts have been directed towards developing materials for CO_2 capture and storage.[22, 99-102] Traditionally, wet-scrubbing technologies have been used for CO_2 capture industrially, which are mainly based on the absorption of CO_2 in primary alkanolamines such as monoethanolamine.[103] Despite the high selectivity in capturing CO_2, the high energy requirement and associated cost of the regeneration present a considerable drawback.[100] Adsorptive and membrane-based separations are two alternatives that have the potential for lower energy demand.[104] A variety of solid adsorbents such as zeolites, activated carbons, metal oxides, metal organic frameworks (MOFs) can bind CO_2 by weak physisorptive forces or strong chemisorptive forces.[105] Membrane-based separations are becoming increasingly attractive for separation of CO_2 from natural gas and flue gas streams, primarily due to the ability to selectively remove CO_2 from gas mixtures, the low energy consumption and the flexibility in configuration for retrofitting applications.[106] Among the inorganic, organic and hybrid membrane materials, polymeric membranes are currently employed at an industrial scale as they can be processed into units with large surface areas enabling low-cost production. However, they suffer from a trade-off between permeability and selectivity which leads to an upper bound on their performance.[6-7] To overcome this upper bound, hybrid nanocomposites are increasingly being studied, which provides a new paradigm allowing a step-change in membrane performance meanwhile minimizing the sacrifice in processability and cost-

related issues. Mixed matrix membranes (MMMs) incorporating microporous particles in a polymer matrix have demonstrated a significantly improved performance for CO_2 separation.[107] Among the different morphologies of the incorporated particles in MMMs, high aspect ratio nanosheets are highly desirable as the substantial enhancement in the transport properties can be achieved at a minimal loading by orienting the nanosheets perpendicular to the gas flow direction.[75, 108]

Metal-organic frameworks (MOFs) are crystalline porous materials consisting of metal ions or clusters and organic ligands.[10] They possess regular pore structures and tunable pore sizes due to a wide selection of metal and organic building blocks, giving rise to a large range of gas permeation properties. As a result, they are promising candidates as filler materials in MMMs for CO_2 separations.[109-110] Recently, high aspect ratio MOF nanosheets have gained considerable research interest owing to their unique properties compared to their bulk counterparts, such as the small thickness, large surface area and high flexibility.[111] The synthesis strategies for MOF nanosheets can be divided into two categories. The top-down approach involves exfoliation of layered MOF precursors using techniques such as sonication, ball milling and chemical intercalation.[26, 51, 57] The other approach is bottom-up synthesis (or direct synthesis) where the crystal growth along one direction is restricted by the adsorption of surfactant-like molecules or the modulation of the contact manners between the metal and linker ions.[65-66, 112] In terms of membrane applications, the direct synthesis is often more desirable because of the higher nanosheet quality and yield, giving rise to better membrane performance.[49] However, it remains challenging to synthesize such suspensions containing pure uniform MOF nanosheets.

Cu(BDC) (BDC^{2-} = 1,4-benzenedicarboxylate) is one of the very few MOF nanosheets that can be directly synthesized in pure form with high aspect ratio. Its synthesis was first developed by Rodenas et al. with a three-layer (linker-solvent-metal) gradient synthesis method, yielding nanosheets with thickness of 5-25 nm.[66] Building on this report, Shete et al. identified a direct homogeneous mixing condition that yields Cu(BDC) nanosheets with aspect ratios as high as 100 (average lateral size 2.5 μm and thickness of 25 nm) by systematically tuning the synthesis temperature and mixing conditions.[67] Incorporation of the Cu(BDC) nanosheets into a Matrimid polymer led to MMMs that exhibited increase in CO_2/CH_4 selectivity about 70% with reduced CO_2 permeability compared to that of the neat polymer.[66-67] The effective permeabilities of Cu(BDC) nanosheets were estimated based on the experimental data and a mathematical model describing transport in MMMs.[67] Besides Matrimid, in another study, Cu(BDC) nanosheets have also been incorporated into more permeable polymers such as 6FDA-DAM and PIM-1, whose CO_2 permeabilities are about 2 orders of magnitude higher than that of Matrimid. The resultant MMMs showed improved CO_2/CH_4 selectivity about 30-40% and reduced CO_2 permeability relative to the neat polymer.[113] However, the experimental MMMs permeability values are much higher than the model-predicted values based on the effective permeabilities of Cu(BDC) nanosheets in Matrimid, indicating the possible presence of defects or modification of the polymer matrix in the membranes.[67] It is known that the match of the permeabilities between the filler and the polymer matrix is essential to realize a substantial improvement relative to the neat polymer. Thus it is important to gain an understanding of the effective permeabilities of Cu(BDC) nanosheets in high permeability polymers.

Here, we select a highly permeable polymer, 6FDA-Durene, as the polymer matrix to form MMMs. The chemical structure of 6FDA-Durene is shown in **Figure 4-1**. 6FDA-Durene is one type of glassy polyimides that composed of a 2,2'-bis-(3,4-dicarboxyphenyl) hexafluoropropane dianhydride (6FDA) monomer polymerized with a durene diamine. It shows both decent selectivities and permeabilities for CO_2 separations with a high free volume of about 18%.[114-115] A couple of studies in the literature have focused on the permeation properties of MMMs based on 6FDA-Durene. Bachman et al. incorporated Ni_2(dobdc) particles in 6FDA-Durene and observed an increase in both the selectivity and permeability of the MMMs for separating CO_2 from CH_4.[110] Japip et al. incorporated ZIF-71 particles in 6FDA-Durene and observed a 3-fold increase in the single gas permeability of CO_2 and about 10% decrease in the CO_2/N_2 ideal selectivity.[116] We study the effect of addition of Cu(BDC) nanosheets on the transport properties and microstructure of the resultant 6FDA-Durene-based MMMs. To the best of our knowledge, this is the first time that MOF nanosheets are incorporated into this polymer matrix.

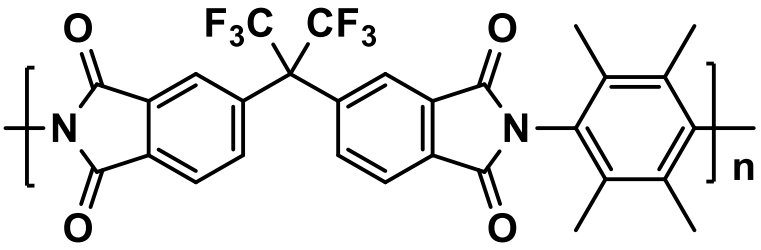

Figure 4-1. Chemical structure of 6FDA-Durene.

4.2 Experimental

4.2.1 Chemicals

Copper nitrate trihydrate ($Cu(NO_3)_2 \cdot 3H_2O$, 99%), terephthalic acid (H_2BDC, 98%) and acetonitrile (CH_3CN, 99.5%) were purchased from Sigma-Aldrich. N,N-dimethylformamide (DMF, 99.9%) and chloroform ($CHCl_3$, 99.9%) were purchased from Fisher Scientific. 6FDA-Durene was synthesized using the procedure reported in the literature and was kindly provided by our collaborators at the University of California, Berkeley.[110] Matrimid 5218 was kindly provided by Huntsman Advanced Materials. All chemicals were used as received.

4.2.2 Synthesis of Cu(BDC) nanosheets

Cu(BDC) nanosheets were directly synthesized following a method reported in the literature.[67] First, 900 mg of $Cu(NO_3)_2 \cdot 3H_2O$ was dissolved in 30 mL of DMF and 90 mL of CH_3CN to form metal solution in a conical flask while 900 mg of H_2BDC was dissolved in 90 mL of DMF and 30 mL of CH_3CN to form linker solution. The metal solution was then added dropwise to the linker solution under magnetic stirring over a period of 45 ~ 60 min. After complete addition, the resulting solution mixture was shaken in an orbital shaker (Thermo Scientific MAXQ 4000) at a speed of 200 rpm under 15 °C for 48 h. The precipitate was collected by centrifugation at 11000 RCF (relative centrifugal force) for 1h and washed with DMF three times. The solvent exchange was performed by repeated centrifugation (11000 RCF, 1h) in chloroform. In between centrifugation cycles, the cake was dispersed by vortexing (Fisher Scientific vortex mixer) and sonication (Branson 5510R-DTH ultrasonic cleaner), and then the dispersed nanosheets were kept static in chloroform for at least 1 h to facilitate the solvent exchange. This process was repeated 3

times. To purify the nanosheets from thick plates, the nanosheet suspension in chloroform was sonicated using a horn sonicator (Qsonica Q500, 500 watts, 0.25" microtip operating at 20% of maximum amplitude) for 20 s followed by sedimentation for 2 d. 80% of top suspension was collected and eventually used for the fabrication of MMMs.

4.2.3 Fabrication of MMMs

The membranes were fabricated by solution casting. To prepare the solution for the neat polymer membranes (6FDA-Durene or Matrimid), chloroform was added to the polymer to form a 2 wt % solution. To prepare the solution for the MMMs, a nanosheet suspension in chloroform was first concentrated by N_2 flow to remove the excess chloroform and then the concentrated suspension was added to polymer with the chloroform/polymer mass ratio kept the same as that for the neat polymer solution. The resultant solution was shaken in an orbital shaker at 250 rpm overnight, sonicated for 30 min (Branson 5510R-DTH ultrasonic cleaner), shaken again for 1 h and sonicated using a horn sonicator for 5 s. The solution was then cast onto a home-built flat bottom glass well in a glove bag filled with N_2 and chloroform vapor. After solvent evaporation at room temperature for 24 h, the resulting membrane was removed from the glass plate and activated at 180 °C under reduced pressure (0.1 bar) for 18 h. The film thickness was found to be in the range of 27 – 50 μm. The membranes were stored in N_2 glovebox.

The loading of Cu(BDC) nanosheets in the MMM was determined by a thermogravimetric analysis (TGA) method using the data from TGA of nanosheets powder as a reference. TGA was performed using a Shimadzu TGA-50 analyzer. Samples were activated under air (60 mL/min) at 120 °C for 1 h before the TGA profile was collected at a ramp rate of 10 °C/min up to 850 °C. The percentage of mass remaining after ramping to 850 °C was

attributed to the mass of metal oxide. By comparing this mass with the mass of metal oxide remaining after TGA obtained on a known weight of nanosheet powder, the loading of Cu(BDC) nanosheets in the MMM was determined.

4.2.4 Characterization

Transmission electron microscopy (TEM) nanosheet samples were prepared by applying several drops of nanosheet suspension onto TEM grids (ultrathin carbon film on holey carbon support film, 400 mesh Cu, Ted Pella). The grids were dried at room temperature and imaged. Conventional TEM imaging and selected area electron diffraction were performed on FEI Tecnai T12 TEM operating at 120 kV.

Atomic force microscopy (AFM) was performed in tapping mode using a Bruker Nanoscope V Multimode Scanning Probe Microscope. Samples for AFM analysis were prepared by applying a few drops of the nanosheet suspension on a Si wafer followed by drying.

The MMM cross-sections for TEM imaging were prepared as follows. The sample pieces were embedded in epoxy resin and polymerized at room temperature for overnight. 80 nm cross sections were cryo microtomed at -140 °C by using Leica UC6/FC6 microtome and a Diatome cryo diamond knife. The sections were collected on 400 mesh copper grids for analysis.

4.2.5 Gas permeation measurements

Single gas permeation experiments were performed in a constant-volume, variable-pressure instrument built in-house. A membrane coupon (22 mm in diameter) was cut out from the films and affixed to a steel fender washer using epoxy. The fender washer was then tightly sealed in a permeation cell. The system was kept under vacuum before the gas

permeation measurements were initiated. Permeation of N_2 was measured at three different feed pressures followed by permeation of CO_2. Upon the isolation of the downstream volume from vacuum, the gas is allowed to accumulate, and the rate of pressure increase was used to determine the gas permeability values. A leak rate of the system (including the membrane cell) was determined by affixing a dense metal disk to the fender washer, sealing it into the permeation cell and then measuring the pressure increase in the downstream volume upon vacuum isolation. The gas permeability is calculated using Eq. (1), where P is the permeability, l is the thickness of the membrane, V is the volume of the downstream chamber where the gas is allowed to accumulate, A is the area of the membrane exposed to the gas, p_f is the feed pressure, R is the gas constant, T is the absolute temperature in K, $\left({dp}/{dt}\right)_{SS}$ is the steady-state permeation rate and $\left({dp}/{dt}\right)_{leak}$ is the leak rate.

$$P = \frac{lV}{Ap_fRT}\left[\left({dp}/{dt}\right)_{SS} - \left({dp}/{dt}\right)_{leak}\right] \quad (1)$$

Permeabilities are reported in the unit of Barrer. Leak rate is about 0.03 Barrer for a 50 μm-thick film when corresponded to permeability. Temperature of the system was kept at 35 °C during the permeation experiments using a water bath.

4.3 Results and discussion

Cu(BDC) nanosheets were synthesized by homogeneous mixing following the method reported by Shete and coworkers.[67] The as-synthesized nanosheets were first washed in N,N-dimethyl formamide (DMF) and then transferred to chloroform ($CHCl_3$) to facilitate the formation of the de-solvated structure and the incorporation into the polymer matrix. Transmission electron microscopy (TEM) images (**Figures 4-2a, 4-3a, 4-3b**) show the solvent-exchanged Cu(BDC) nanosheets possess a lateral dimension of 1-3 μm with high uniformity free from aggregation, which is highly desirable for membrane applications. The selected area electron diffraction (SAED) pattern (**Figure 4-2b**) demonstrates a good match with the SAED pattern reported by Shete et al. for the de-solvated Cu(BDC) nanosheets.[67] This confirms that the diffraction spots can be indexed as (0 *k l*) and the solvent-exchanged nanosheets display a de-solvated Cu(BDC) structure with pore channels and crystallographic *a* axis running along the thin dimension (**Figure 4-2d**). As indicated by the atomic force microscopy (AFM) analysis, the typical thickness of the thin dimension of nanosheets is around 25 nm (**Figure 4-2c**), giving rise to nanosheet aspect ratio of about 80.

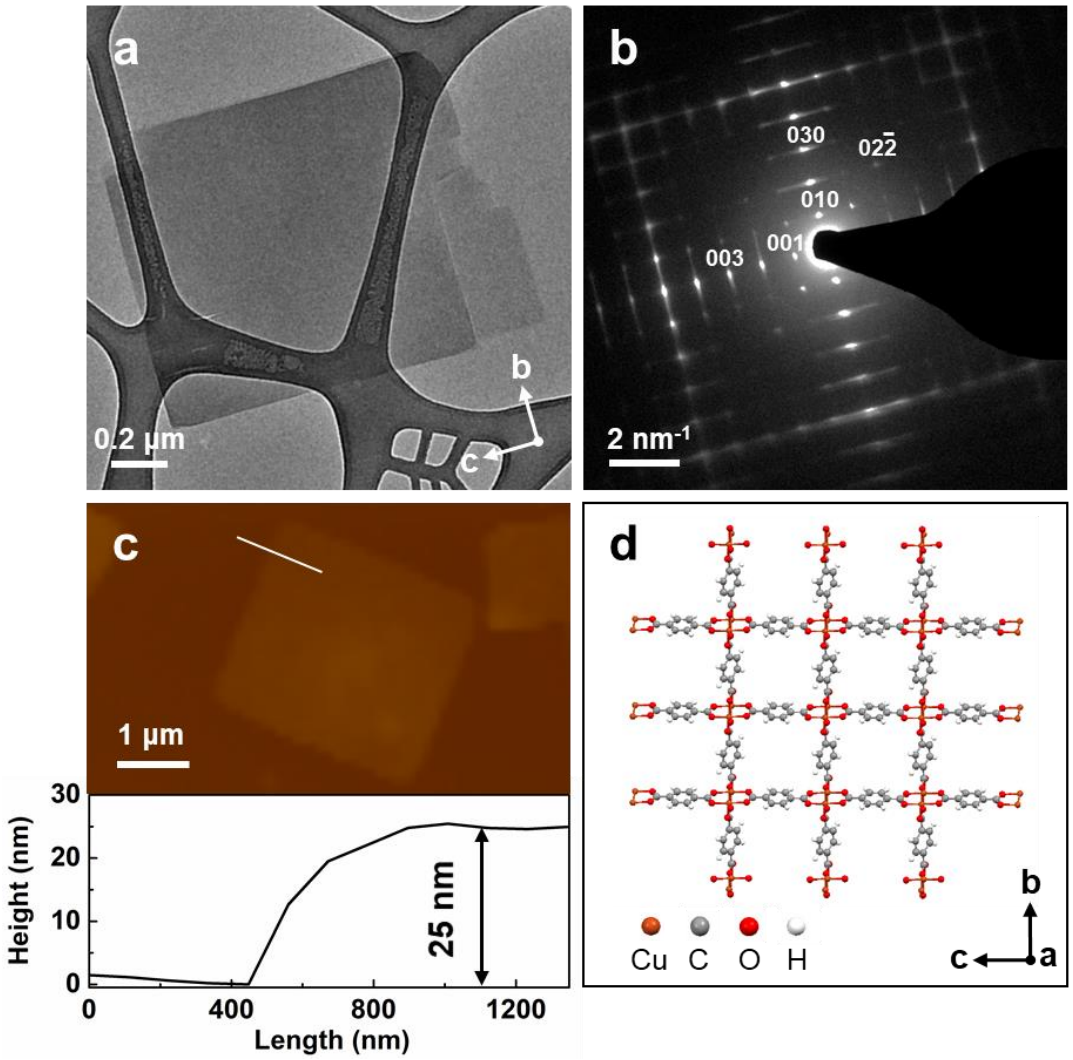

Figure 4-2. (a) TEM image of a Cu(BDC) nanosheet (chloroform washed) and its corresponding electron diffraction pattern (b) indicating the nanosheet is oriented along the a axis. (c) AFM image of nanosheets showing the typical thickness is 25 nm. (d) Schematic of the de-solvated Cu(BDC) structure with 2D layers viewed along the a axis.

During the characterization process, morphological instability of the solvent-exchanged Cu(BDC) nanosheets was observed. The TEM samples prepared by drop casting the nanosheets suspension in chloroform on a TEM grid followed by the evaporation of the volatile chloroform solvent were imaged at different time to track this effect. When imaged

within 45 minutes of the sample exposure to the ambient, the nanosheets exhibited well-defined facets, uniform thickness and smooth surface as shown in **Figures 4-3a,b**. When the TEM sample was then kept in the ambient for 20 more hours and imaged again, local thickening and void formation were observed leading to a slight increase in the surface roughness (**Figure 4-3c**). In contrast, when the sample was kept instead in a desiccator for 34 days, nanosheets could remain in good shape and surface quality (**Figure 4-3d**). This indicates the dried Cu(BDC) is sensitive to the moisture in the ambient air. As moisture is known to induce structural, morphological and chemical changes to carboxylate MOFs including Cu(BDC), the resultant microstructure is likely to induce defect and pore structure collapse during MMMs formation.[117-118] Therefore, the MMMs in this study were processed and stored in a moisture-free condition to effectively prevent the Cu(BDC) degradation. Besides dried Cu(BDC), long time storage of Cu(BDC) nanosheets in chloroform suspension also presents an instability issue. After staying in chloroform suspension for 52 days, as shown in **Figure 4-3e**, the nanosheets lost their integrity as part of the sheets were broken into small pieces and aggregated into larger particles. To prevent this from happening, in our study, fresh Cu(BDC) nanosheets were synthesized and used for MMMs fabrication.

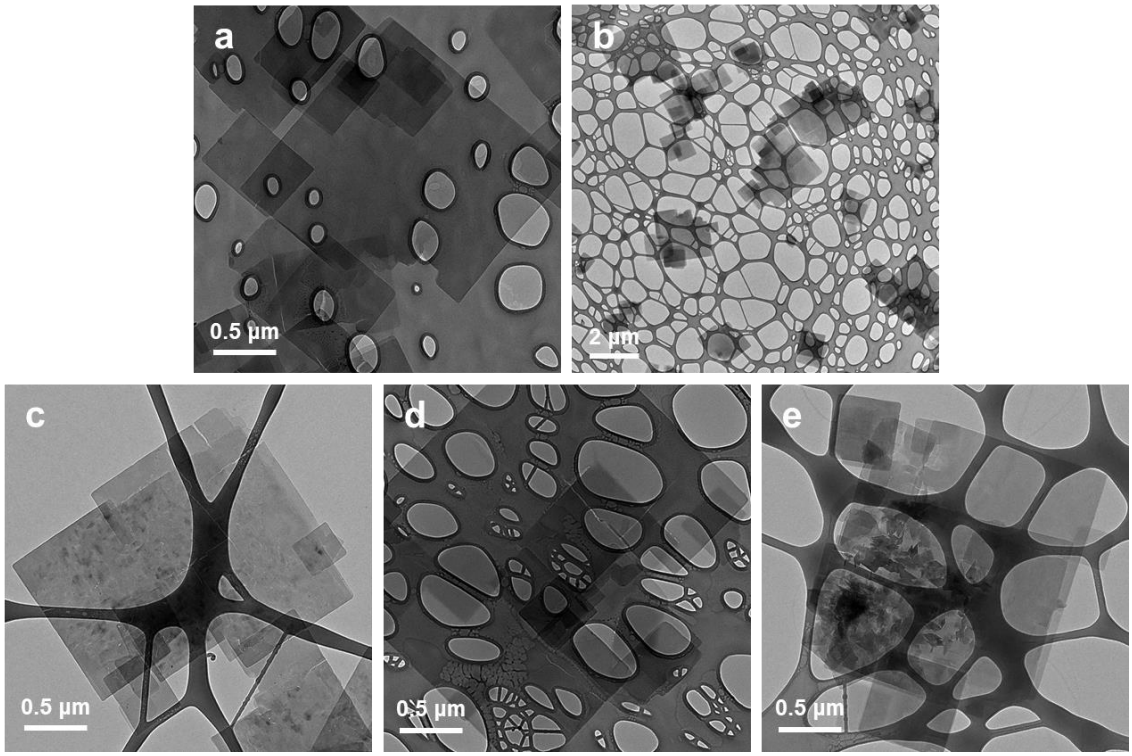

Figure 4-3. TEM images of chloroform solvent-exchanged Cu(BDC) nanosheets under different conditions. (a, b) TEM images of fresh Cu(BDC) nanosheets imaged within 45 min of the TEM grid exposure to the ambient. (c) TEM image of fresh Cu(BDC) nanosheets imaged after 20 h of TEM grid exposure to the ambient. (d) TEM image of the grid shown in (a, b) after 34 d of storage in a desiccator and imaged within 45 min of the grid preparation. (e) TEM image of nanosheets after suspended in chloroform for 52 d and imaged within 45 min of the grid preparation.

Mixed-matrix membranes were fabricated by incorporating Cu(BDC) nanosheets in 6FDA-Durene. Nanosheet suspension in chloroform was mixed with 6FDA-Durene and uniform MMMs were then obtained by solution casting in N_2 atmosphere (**Figure 4-4**). A nanosheet loading of 13 wt% was quantified by the thermogravimetric analysis (TGA) (**Figure 4-5**). Microtomy analysis on MMMs cross sections was used to characterize the

membrane morphology. Compared with the neat polymer, the 13 wt% MMM shows uniform distribution of Cu(BDC) nanosheets which correspond to the dark contrast in the TEM images (**Figure 4-6**). The nanosheets appear to be ~ 25 nm thick on average, agreeing well with the AFM measurement, which indicates individual nanosheets are free from aggregation upon incorporation into 6FDA-Durene at this high loading. Over 85 % of the nanosheets are oriented in a desirable manner, i.e. perpendicular to the thickness dimension of the membrane, suggesting the efficient alignment of the pore channels of the nanosheets. In addition, no apparent voids or defects are evident at the nanosheet-matrix interface, indicating that the sheets are well compatible with the polymer matrix. Overall, the membranes demonstrate a desirable morphology.

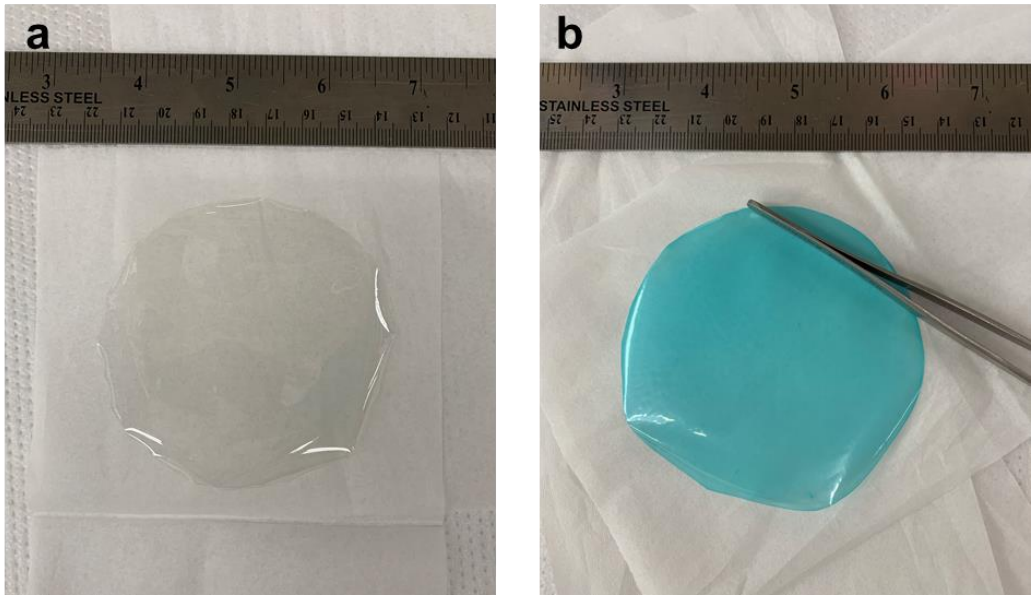

Figure 4-4. Photographic images of (a) 6FDA-Durene film and (b) mixed matrix membrane incorporating 13 wt% Cu(BDC) nanosheets in 6FDA-Durene showing the uniform distribution of the nanosheets within the matrix.

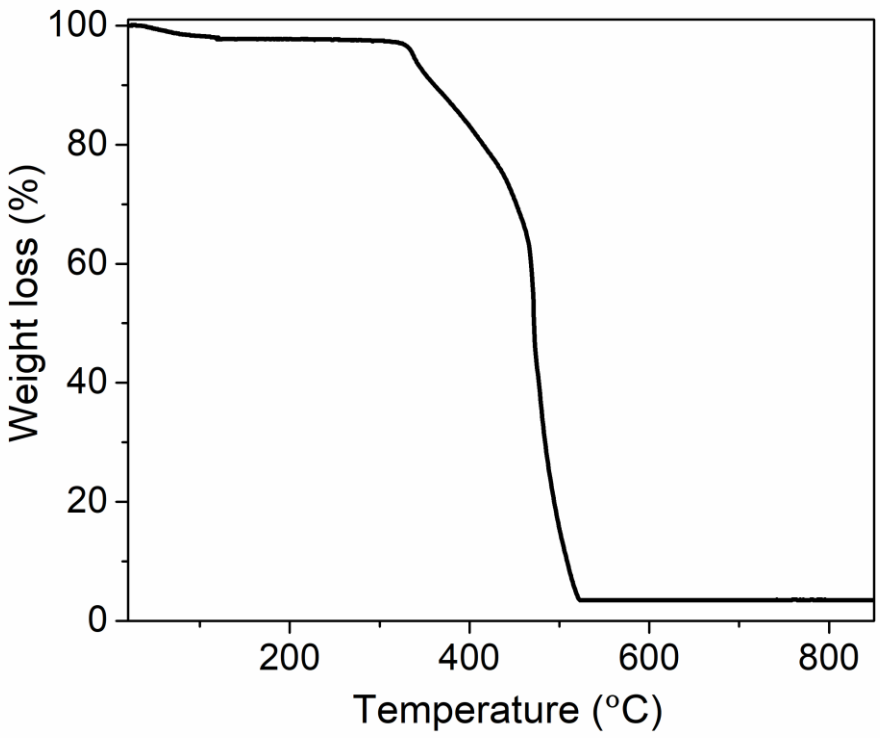

Figure 4-5. TGA of 6FDA-Durene-Cu(BDC) MMM giving rise to a calculated nanosheet loading of 13.4 %.

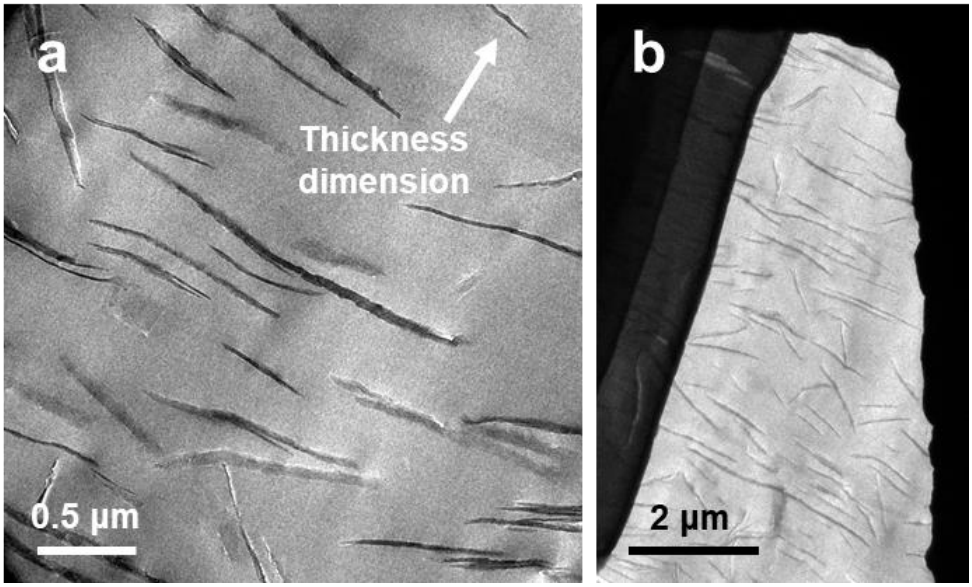

Figure 4-6. TEM images of the microtomed sections of a 13 wt% MMM based on 6FDA-Durene. (a) TEM image of a local region, depicting the nanosheets are aligning perpendicular to the thickness dimension of the membrane free from aggregation and nanosheet/polymer interfacial defects. The average thickness of nanosheets is 25 nm, matching well with the thickness obtained from AFM analysis of as-synthesized nanosheets. (b) TEM image at a lower magnification showing the uniform distribution of the nanosheets within the polymer matrix.

Single gas (CO_2, N_2) permeation measurements were performed at different feed pressures (1, 3, and 5 bar) to evaluate the performance of the MMMs. As seen from **Figure 4-7**, addition of Cu(BDC) nanosheets leads to an increase in the selectivity for the MMMs over that of the neat polymer while the CO_2 permeability remains almost unchanged for all of the feed pressures tested. For example, at 13 wt% loading and 1 bar feed pressure, the CO_2 permeability keeps the same while the N_2 permeability decreases, resulting in a 44% increase in CO_2/N_2 ideal selectivity. This performance is very intriguing as the selectivity is improved without the sacrifice in CO_2 permeability.

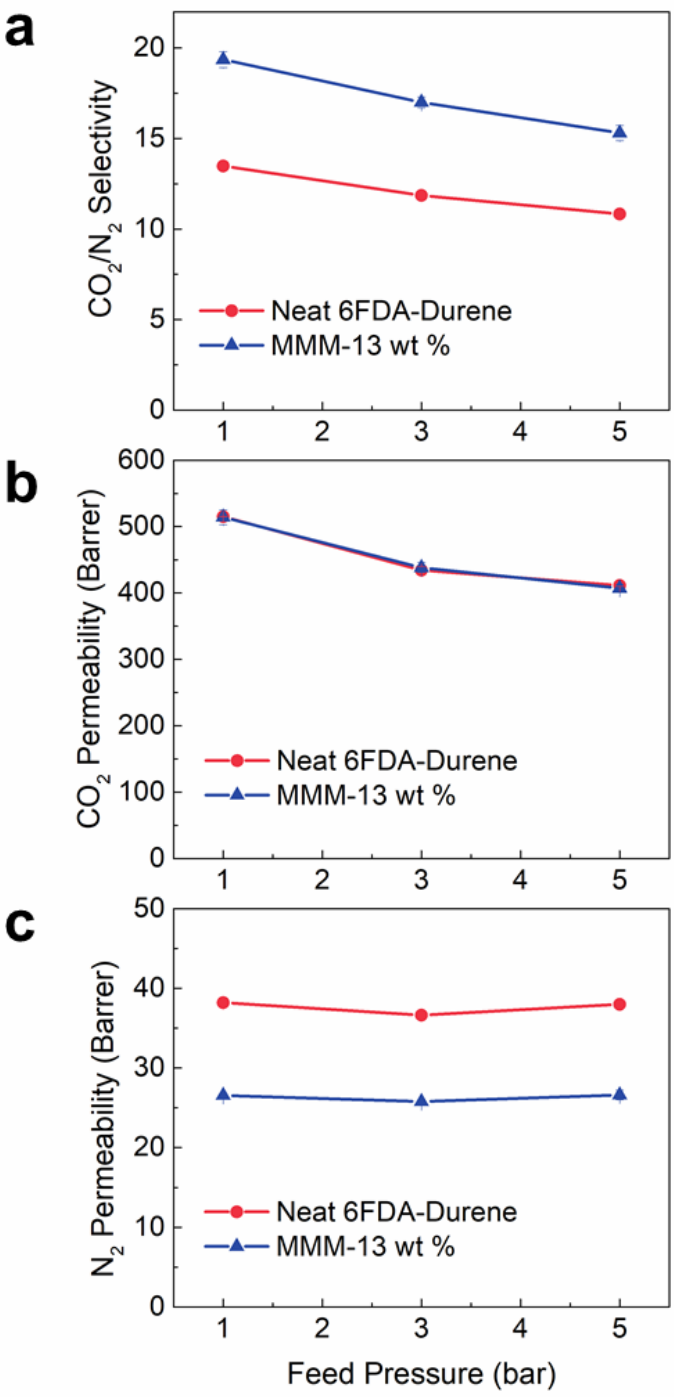

Figure 4-7. Single gas CO_2 and N_2 permeation data for neat 6FDA-Durene and MMM incorporating 13 wt% Cu(BDC) nanosheets, showing (a) ideal selectivity, (b) CO_2 permeability, and (c) N_2 permeability versus feed pressure.

To understand the gas permeation results, we analyzed the permeation data using mathematical models developed for MMMs. Cussler model describes two-dimensional transport of a component across a polymer composite where oriented staggered flakes are dispersed in the polymer matrix.[119]

The permeability of component *i* in a composite membrane P_i^C is given by

$$P_i^C = P_i^M * \frac{1}{(1-\varphi) + \frac{1}{\left[\left(\frac{1}{\varphi}\right)\left(\frac{P_i^F}{P_i^M}\right) + 4 * \left(\frac{1-\varphi}{\alpha^2\varphi^2}\right)\right]}} \quad (2)$$

where P_i^M and P_i^F are the permeabilities of the neat polymer matrix and flake, and α and φ are aspect ratio and the volume fraction of the loaded flake in the membrane. The model assumes constant flake and matrix permeabilities, and an ideal morphology where flakes are dispersed uniformly in regular spacing free from flake-matrix interfacial defects. This model was shown to describe the behavior well for MMMs with high aspect ratio flakes and moderate to high volume fraction (> 10%), as is the case for MMMs studied here (φ ~ 13%). When the flake aspect ratio is high and the volume fraction is low (< 10%), a slight modification to the Cussler model which results in Modified Cussler model, as shown in Eq.(3), is more successful in performance prediction.[120]

$$P_i^C = P_i^M * \frac{1}{(1-\varphi) + \frac{1}{\left[\left(\frac{1}{\varphi}\right)\left(\frac{P_i^F}{P_i^M}\right) + \left(\frac{1-\varphi}{\alpha^2\varphi^2}\right)\right]}} \quad (3)$$

Using Eq.(2) and the our permeation data, with an average flake aspect ratio of 80, CO_2 and N_2 flake permeabilities were extracted. As shown in **Table 4-1**, the flake permeability for CO_2 is in the range of 379 – 507 Barrer and that for N_2 is in the range of 8.5 – 8.7 Barrer. This gives rise to flake selectivity in the range of 44 – 59. Considering the matrix CO_2

permeability is in the range of 411 – 515 Barrer and N_2 permeability is in the range of 36 – 38 Barrer, the permeabilities of the fast permeating species (in this case CO_2) through the matrix and flake are closely matched, leading to a performance enhancement.

Table 4-1. Permeation results for neat 6FDA-Durene membrane and 13 wt% MMM at different feed pressures (p_f). P^M_{CO2} is CO_2 permeability of the neat polymer matrix; P^C_{CO2} is CO_2 permeability of the composite membrane; P^M_{N2} is N_2 permeability of the neat polymer matrix; P^C_{N2} is N_2 permeability of the composite membrane; P^F_{CO2} is CO_2 permeability of the Cu(BDC) flake and P^F_{N2} is N_2 permeability of the Cu(BDC) flake. The flake permeability values are extracted using Cussler model.

	Experimental permeability for MMMs (Barrer)				Extracted flake permeability		
p_f (bar)	P^M_{CO2}	P^C_{CO2}	P^M_{N2}	P^C_{N2}	P^F_{CO2}	P^F_{N2}	Selectivity
1	515	514	38.2	26.6	507	8.6	59
3	434	438	36.6	25.8	465	8.5	55
5	411	407	38.0	26.6	379	8.7	44

As introduced earlier, Cu(BDC) nanosheets were also incorporated in polymer Matrimid, 6FDA-DAM and PIM-1 at a lower loading.[67, 113] Assuming idealized MMMs morphology and using Modified Cussler model, the flake permeabilities in these polymers can also be extracted. As listed in **Table 4-2**, the flake permeabilities for CO_2 demonstrate a large range from 1.9 Barrer up to 507 Barrer. As flake permeability is an intrinsic property depending on the pore structure of the material, it is expected to show stable values. Thus, the extracted flake permeabilities from MMMs are only effective values depending not only on the pore structure, but also on the properties of the flake-matrix interfacial region, which could be impacted by the fabrication history.

Table 4-2. Comparison of permeation results for Cu(BDC)-based MMMs in the literature. The first two columns correspond to the reported experimental data for the neat polymer and the last two columns correspond to model-extracted values for Cu(BDC) flake. The Cussler model is used to extract flake permeability values for 6FDA-Durene MMM due to a high nanosheet loading. The Modified Cussler model is used to extract flake permeability values for all other MMMs. The selectivity for the first three rows corresponds to CO_2/N_2 selectivity and the selectivity for the last two rows corresponds to CO_2/CH_4 selectivity.

	Neat Polymer		**Cu(BDC) Flake**	
	CO_2 Permeability (Barrer)	Selectivity	CO_2 Permeability (Barrer)	Selectivity
6FDA-Durene (This work)	515	13	507	59
Matrimid (This work)	8.8	21	0.7	30
Matrimid (Ref. 67)	7.2	24	1.9	160
6FDA-Dam (Ref. 113)	590	30	54	78
PIM-1 (Ref. 113)	3100	17	250	36

Ideally, the flake-matrix interfacial region contains polymer chains well attached to the outer surface of the flakes without blocking the pores of the flakes. These chains at the interface are supposed to show similar properties to the chains in the bulk matrix. However, depending on the stress at the interface generated during the membrane fabrication, an undesirable void or a region with rigidified polymer chains could form, leading to non-ideal morphologies.[121] The case with voids at the interface, referred to as "sieve-in-a-cage" morphology, often results in increased permeability with same or lower selectivity compared to neat polymer depending on the void size. For the case where rigidified region of the polymer matrix is formed around the flakes, the MMMs exhibit reduced permeability and increased selectivity. Considering the Cu(BDC) nanosheet MMMs reported before all showed a trend of reduced permeability and increased selectivity, matrix rigidification is

likely to play a role, causing the effective flake permeabilities smaller than what we observe in 6FDA-Durene.

Since the stress at the interface is influenced primarily by the solvent evaporation, which is highly dependent on preparation history,[121] we fabricated MMMs in Matrimid with the same procedure as that in 6FDA-Durene to see if the same effective flake permeabilities can be obtained. As shown in **Figure 4-8**, the 6 wt% MMM leads to reduced CO_2 and N_2 permeabilities indicating the effective flake permeability values are lower than the matrix permeability values. Specifically, at feed pressure of 1 bar, the extracted flake permeability for CO_2 is 0.7 Barrer and selectivity is 30 (**Table 4-2**). These results in Matrimid demonstrate a similar trend as reported before, and it also shows that with the same fabrication history, the effective flake permeabilities could still differ by 2 orders of magnitude. This indicates the polymer type also plays a role in determining the effective Cu(BDC) flake permeabilities, likely due to the different polymer chain mobilities in response to the stress.

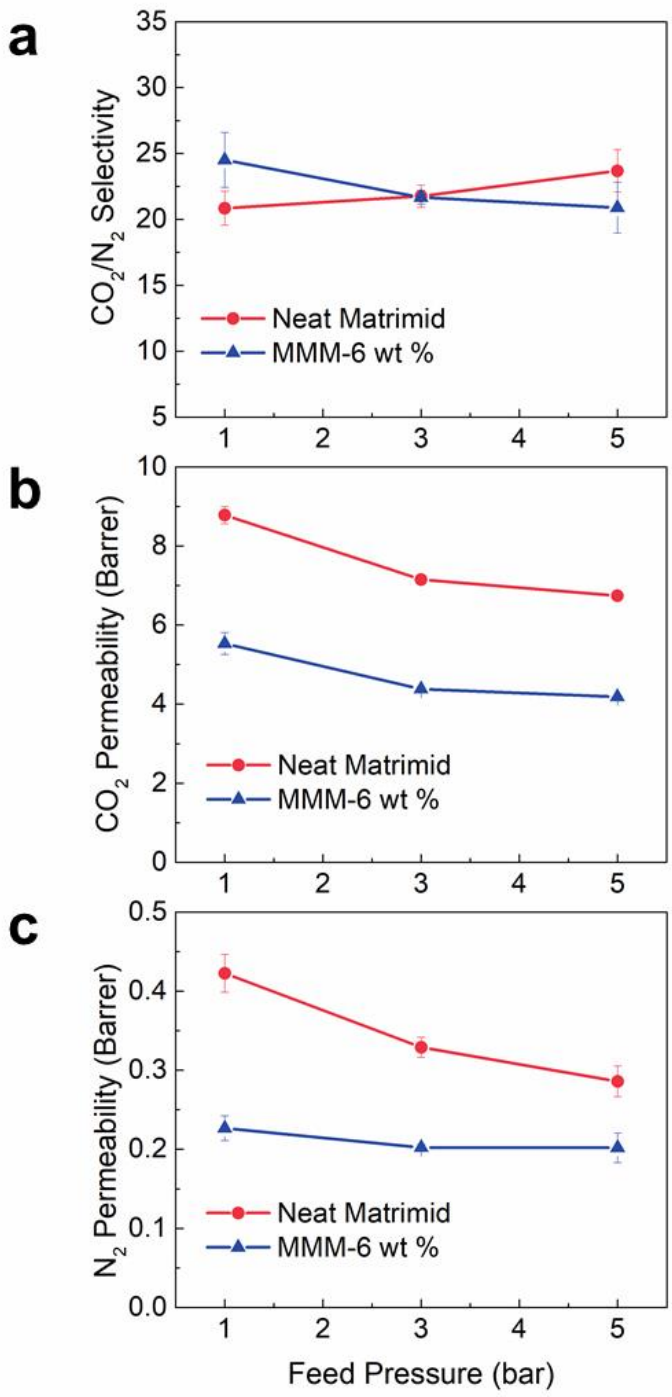

Figure 4-8. Single gas CO_2 and N_2 permeation data for neat Matrimid and MMM incorporating 6 wt% Cu(BDC) nanosheets, showing (a) ideal selectivity, (b) CO_2 permeability, and (c) N_2 permeability versus feed pressure.

4.4 Conclusion

In summary, high aspect ratio Cu(BDC) nanosheets with a de-solvated structure were synthesized and incorporated into high permeability polymer 6FDA-Durene to form mixed matrix membranes. The de-solvated Cu(BDC) nanosheets exhibit a tendency of instability towards moisture and long-time storage in chloroform, and it is found effective to prevent the degradation by using freshly synthesized nanosheets under moisture-free conditions during membrane fabrication. A method to fabricate functional MMMs with a nanosheet loading as high as 13 wt% was developed. The 13 wt% MMM displays uniform, oriented nanosheet distribution in the matrix free from nanosheet aggregation and nanosheet-polymer interfacial defects. The incorporation of nanosheets leads to a 44% increase in CO_2/N_2 ideal selectivity and a similar CO_2 permeability relative to the neat 6FDA-Durene membrane. Using the experimental permeation data and mathematical models for transport in MMMs, the effective permeabilities of CO_2 and N_2 for Cu(BDC) nanosheets in 6FDA-Durene were obtained to be in the range of 379 – 507 Barrer and 8.5 – 8.7 Barrer respectively. The close match of CO_2 flake permeability with the matrix and a higher flake CO_2/N_2 selectivity relative to the matrix accounted for the performance enhancement in the MMMs. When compared to the effective permeability values extracted based on the permeation data reported in other polymers, a range of permeability differing in two orders of magnitudes was identified, indicating the existence of non-ideal morphologies in the flake-matrix interfacial region such as matrix rigidification in those polymers. Besides the fabrication history, the polymer type is also found to affect the effective permeabilities of the Cu(BDC) flake in MMMs. Among the polymers studied in Cu(BDC) nanosheet-based MMMs, 6FDA-Durene shows the best match with the Cu(BDC) nanosheets by now in

terms of effective permeabilities and interfacial morphology, holding promise for future applications in MOF nanosheet hollow fiber membranes.

Chapter 5: All-vapor-phase synthesis of ZIFs membranes for propylene/propane separation

5.1 Introduction

Zeolitic imidazolate frameworks (ZIFs) membranes, a subclass of metal-organic framework (MOFs) membranes, are emerging as attractive gas separating agents,[21, 38-39] holding promise for improving the energy efficiency of separation processes involving important industrial mixtures, such as propylene/propane.[23, 35-36] However, a major hurdle to their industrial application is the lack of low-cost scalable fabrication methods.[2] Recently, the development of all-vapor-phase processing of MOFs thin films has opened new opportunities to prepare ZIFs membranes, suggesting the great potential for overcoming this barrier. The vapor processing of MOFs is based on a two-step concept, called MOF-chemical vapor deposition (MOF-CVD), in which metal oxide precursor layer is first deposited on silicon wafers by vapor-phase deposition techniques such as atomic layer deposition (ALD) and subsequently converted to MOF polycrystalline films upon the reaction with ligand vapor.[45] For example, polycrystalline ZIF-8 films were fabricated by reacting 2-methyldimidazole (mIm) ligand vapor with ALD ZnO layers. In addition to ZIF-8, MOF-CVD has been successfully applied to fabricate other MOFs thin films, such as ZIF-61, ZIF-67, ZIF-72, CuBDC (BDC^{2-} = 1,4-benzenedicarboxylate) and CuCDC (CDC^{2-} = trans-1,4-cyclohexanedicarboxylate), suggesting its general applicability.[45, 122] Besides MOF-CVD, direct sequential reactions between metal and ligand vapor precursors to form MOF films in a layer-by-layer fashion have also been reported, leading to thin films of HKUST-1, calcium terephthalate and amorphous layers which were subsequently crystallized to UiO-66 upon acetic acid vapor treatment.[123-125]

The vapor processing of MOF thin films on non-porous substrates has promoted the integration of MOFs materials in microelectronics.[45, 126-127] It also inspires novel vapor processing of gas separation membranes on porous supports. Kwon et al. first introduced ligand vapor treatment as a secondary growth method to prepare ZIF-8 membranes by an Ostwald-ripening process.[128] Li et al. showed ultrathin (ca. 17 nm) ZIF-8 membranes fabricated by treating ligand mIm vapor to a Zn-based gel supported on porous supports.[46] In these reports, certain steps in membrane fabrication were replaced with vapor processes. Later, an all-vapor-phase membrane synthesis method, called ligand-induced permselectivation (LIPS) was developed by Tsapatsis group.[47]

As illustrated in **Figure 5-1**, The LIPS method consists of the ALD of dense ZnO inside the mesopores (ca. 2 – 5 nm) of the γ-alumina layer which is coated on the α-alumina support, followed by ligand vapor (2-methylimidazole = mIm) treatment. During ALD, the surface hydroxyl groups present on the pore surface of γ-alumina react with alternating diethylzinc and water precursors to form ZnO deposits. After ALD, the nanocomposite becomes impermeable and nonselective, whereas after mIm-vapor treatment, it is transformed to thin (ca. 100 – 200 nm) continuous ZIF membranes and shows high permeance and selectivity for propylene/propane separation. Despite the high performance, the development of LIPS membranes is still at an early stage. The understanding of the LIPS process regarding the effect of different processing parameters on the membrane performance is very limited. In this chapter, the ALD processing parameters, γ-alumina support and ligand properties are tuned to optimize the membrane performance and provide fundamental understanding regarding the ZnO and ZIFs deposits formation in the LIPS process.

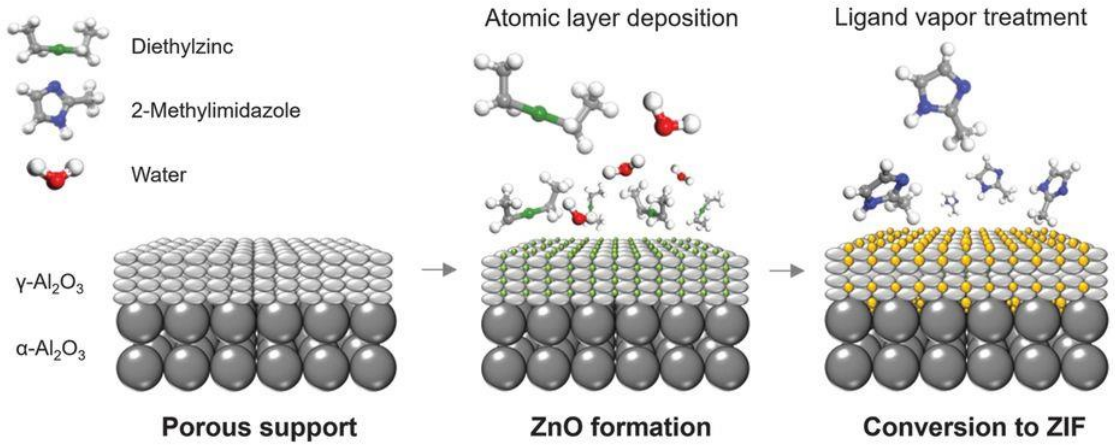

Figure 5-1. Schematic of a LIPS membrane fabrication process. Adapted from reference 47.

5.2 Experimental

5.2.1 Preparation of porous supports

α-alumina porous supports were prepared by a slip casting method developed by the Tsapatsis group.[96] γ-alumina supports were prepared on the surface of α-Al_2O_3 supports by a sol-gel method reported before.[97] 1 M boehmite sol was prepared and mixed with 3 wt% polyvinyl alcohol (PVA) solution to use as coating sol. The γ-alumina sol was then coated on the surface of α-alumina porous support by a slip casting method, followed by overnight drying at room temperature, and calcination at 450 °C for 3 h with a heating and cooling rate of 0.5 °C/min.

The γ-alumina layer thickness was varied by tuning the dip coating time to be 5 s and 10 s. To change the pore size of the γ-alumina layer, the calcination temperature was increased from 450 °C to 550 °C and 600 °C.

5.2.2 All-vapor-synthesis of LIPS membranes

The regular synthesis of LIPS membranes was performed according a previous report.[47] ZnO was first deposited into the γ-alumina supports by 20 cycles of ALD. Each cycle consists of 0.015 s water exposure, 5 s purge, 0.015 s diethylzinc (DEZ) exposure and 5 s purge. After the ALD deposition, the support was placed vertically inside a Teflon liner with 0.2 g 2-methylimidazole (mIm) placed at the bottom. The liner was sealed in an autoclave and heated at 125 °C for 24 h. After the ligand treatment, the membrane was activated in a vacuum oven at 100 °C for 16 h before the gas permeation measurement.

The ALD conditions were varied to study the effect of ALD processing parameters on the membrane performance. For the membranes prepared in the Exposure group as discussed in **Section 5.3.2**, each ALD cycle consists of 0.015 s water pulse, 5 s exposure in the closed chamber, 10 s vacuum purge, 0.015 s DEZ pulse, 5 s exposure in the closed chamber and 10 s vacuum purge. The number of deposition cycles is 20. For the membranes prepared in the Pulse (10× longer) group as discussed in **Section 5.3.2**, each ALD cycle consists of 0.15 s water pulse, 8 s vacuum purge, 0.15 s DEZ pulse and 8 s vacuum purge. The number of deposition cycles is 20. For membranes prepared with changing water pulse pressures as discussed in **Section 5.3.3**, each ALD cycle consists of 0.0055 s water exposure, 5 s purge, 0.015 s DEZ exposure and 5 s purge for ALD with water pulse pressure of 150 Torr. Each ALD cycle consists of 0.005 s water exposure, 5 s purge, 0.015 s DEZ exposure and 5 s purge for ALD with water pulse pressure of 1 Torr. The number of deposition cycles is 20.

The 2-methylimidazole (mIm) materials for ligand vapor treatment used in membrane fabrication were from chemical bottles which have been opened for over 6 months. To

check if the freshness of ligand affects the membrane performance, mIm materials from a newly-opened chemical bottle was used for membranes discussed in **Section 5.3.6**.

5.2.3 Gas permeation test

Single gas permeation tests of propylene and propane were conducted in a home-built constant volume variable pressure apparatus. The membrane was sealed tightly with O-rings inside a stainless-steel permeation cell. The cell was loaded into the apparatus with feed side introduced with pure atmospheric pressure gas at room temperature and permeate side initially maintained under vacuum. During the measurement, the rate of pressure change on the permeate side was used for permeance calculation.

The mixed gas propylene/propane permeation measurements were performed in the Wicke-Kallenbach mode. Typically, 10 sccm equimolar propylene/propane gases at atmospheric pressure were introduced to the membrane feed side. 10 sccm argon at atmospheric pressure was introduced to the permeate side as sweep gas to carry the permeating gas to an attached gas chromatograph (Shimadzu, GC 2014). The composition of permeating gas was determined by gas chromatography equipped with a flame ionization detector (FID) and a capillary column. The selectivity was determined to be the permeance ratio of the two components.

5.2.4 Characterization

X-ray diffraction (XRD) pattern was acquired using a Bruker-AXS (Siemens) D5005 diffractometer with a CuKα radiation source. Scanning electron microscopy (SEM) images were recorded using a Hitachi SU8230 scanning electron microscope operated at 1.5 kV. The membrane cross-sections for high-angle annular dark field – scanning transmission electron microscopy (HAADF-STEM) imaging were prepared by focused-ion-beam

milling with a FEI DualBeam Helios G4. Energy-dispersive X-ray (EDX) spectrum imaging was conducted using a Super-X system.

5.3 Results and discussion

5.3.1 The effect of support location in ALD chamber on the membrane performance

In a typical ALD process, three γ-alumina supports were placed inside the ALD chamber for ZnO deposition as shown in **Figure 5-2.** Sequential alternating water and diethylzinc (DEZ) pulses were introduced from precursor inlet to the chamber, passing the supports and were collected through outlet to the vacuum pump. The 20-cycle ALD modified supports were then treated with mIm ligand vapor to form ZIFs membranes. By careful tracking of the location of the supports and their final separation performance, a correlation between the membrane position in ALD and propylene/propane separation performance was identified. As shown in **Figure 5-3**, the membranes in the position II and III in ALD consistently exhibit ~20 times higher permeance and ~6 times higher selectivity than the membranes in the position I. This suggests more ZnO deposited per cycle that is not efficiently converted to ZIFs in the later ligand treatment for supports in position I. The support in position I, which is the first support in contact with the precursor in each pulse, adsorbs part of the precursor into its high surface area porous structure and leaves proper precursor concentration for supports in position II and III. This effect is not pronounced in the propylene permeance after 20 cycles of ALD, as listed in **Table 5-1**, with propylene permeance all on the order of 10^{-10} mol m^{-2} s^{-1} Pa^{-1}. However, it becomes pronounced in the final membrane performance, which indicates that the membrane performance is very sensitive to the ALD ZnO deposit amount. A suitable precursor concentration enabling a thin non-permeable ZnO deposit is critical to realize consistent high membrane

performance after ligand vapor treatment. Therefore, the following membrane performance reported in this study were collected from membranes in the position II and III.

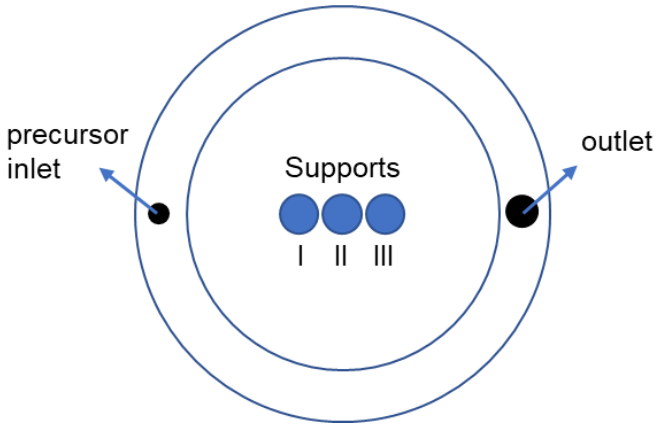

Figure 5-2. Schematic of a top-view ALD chamber loaded with supports. During deposition, the precursor is introduced from the inlet and collected into the vacuum pump through the outlet. In between, it passes supports located in the center of the chamber.

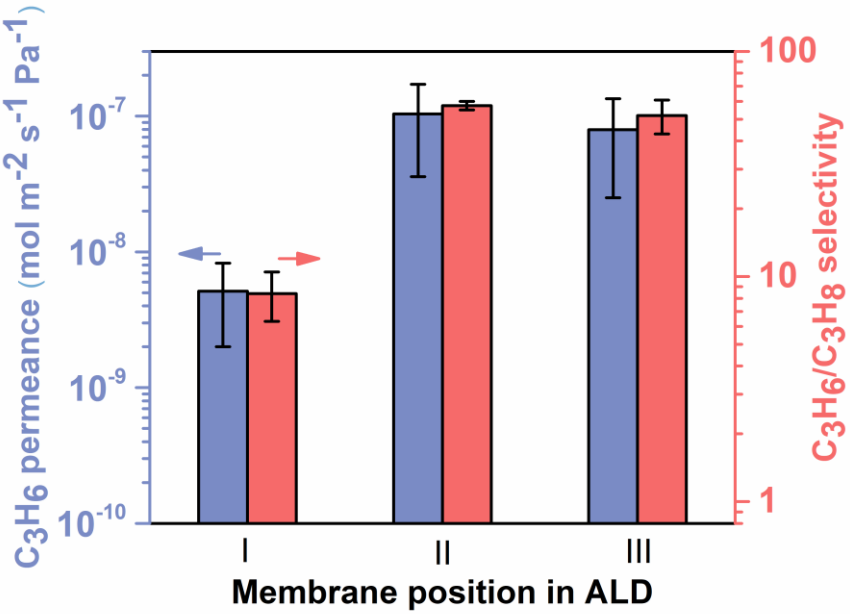

Figure 5-3. Propylene permeances and propylene/propane selectivities for membranes at different positions in ALD chamber.

Table 5-1. Permeation data for supports in different positions after 20 cycles of ZnO ALD.

ALD membrane position	Propylene or propane permeance after 20 cycles of ALD (mol m^{-2} s^{-1} Pa^{-1})
I	4.3×10^{-10}
II	3.1×10^{-10}
III	4.1×10^{-10}

5.3.2 The effect of ALD precursor exposure time on the membrane performance

According to ref. 47, the high propylene/propane separation performance is mostly due to the thin ZIFs deposit (ca. 100 – 200 nm) within and on top of the γ-alumina layer. Tracing back, this thin ZIFs deposit is originated from the thinness of ZnO deposit (ca. 200 nm) formed during ALD. Considering that the thickness of mesoporous γ-alumina layer is ~5 μm, why the ZnO is mostly present near the top 200 nm? To address this question, the ALD precursor exposure time was tuned and its effect on the membrane performance was evaluated.

The ALD condition in the control group, as reported in ref. 47, consists of 0.015 s water pulse, 5 s vacuum purge, 0.015 s DEZ pulse and 5 s vacuum purge in a cycle. To check if the thinness of ZnO is due to the limited diffusion time and/or limited precursor dose, extra time and dose were applied in the ZnO-ALD. In an experimental group named “Exposure”, the precursor pulse time was kept the same while a 5 s-exposure step in the closed chamber was added after each precursor pulse, allowing enough time for precursor diffusion. In another experimental group named “Pulse (10× longer)”, the precursor pulse duration was

increased 10 times such that both the dose and the time allowed for diffusion were increased. For all three groups, the number of deposition cycles was 20.

The propylene/propane separation performance of membranes after ligand vapor treatment is shown in **Figure 5-4**. The control group demonstrates high propylene permeance (above 1×10^{-7} mol m^{-2} s^{-1} Pa^{-1}) and high propylene/propane selectivity (above 60) while the experimental groups display low propylene permeances on the order of 10^{-10} mol m^{-2} s^{-1} Pa^{-1} and propylene/propane selectivities of 1-2.

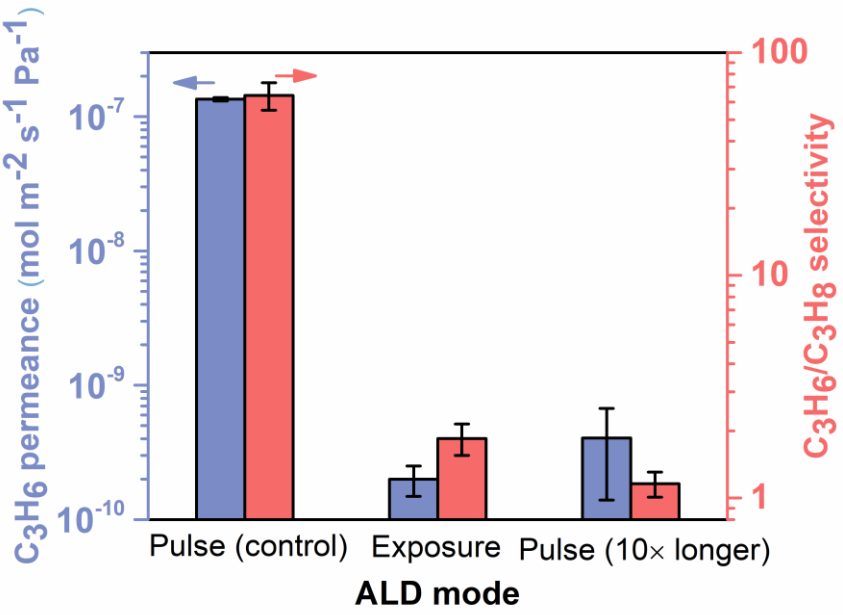

Figure 5-4. Propylene permeances and propylene/propane selectivities for membranes treated with different ALD deposition modes.

To better understand the gas permeation data, the microstructure of the membranes was characterized. **Figure 5-5** shows the top-view SEM images and X-ray diffraction patterns of the membranes. The membrane in the control group demonstrates 50 – 200 nm sized crystals on the top surface (**Figure 5-5a**), which are slightly smaller than the crystals on the membranes in the experimental groups (**Figures 5-5b, c**). All the membranes display

XRD peaks (**Figure 5-5d**) matching a ZIF-8 structure with the membrane in the Exposure group having a higher intensity, suggestive of an overall thicker top ZIF-8 layer.

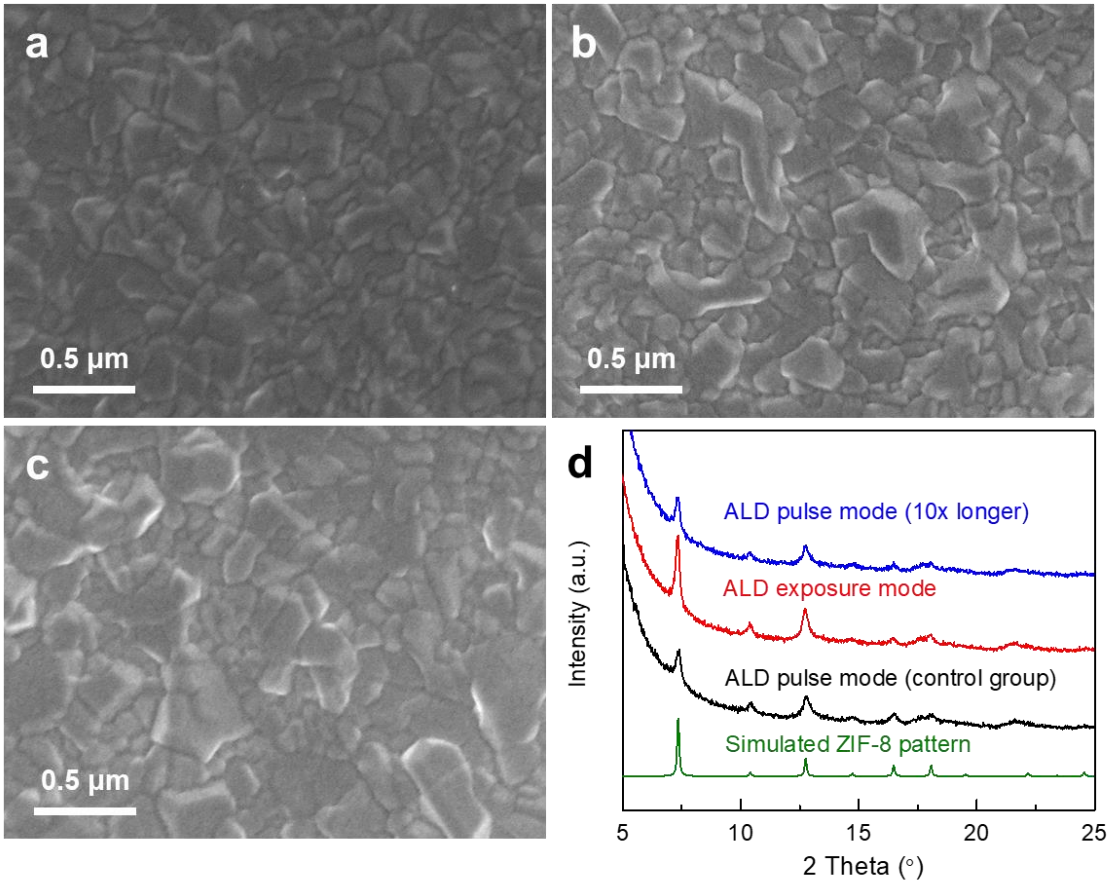

Figure 5-5. Top-view SEM images of membranes treated with different ZnO ALD conditions. (a) Regular ALD condition (control group) (b) Additional 5 s- exposure of precursor in the closed chamber after each pulse (Exposure group) (c) 10 times longer pulse time for two precursors (Pulse (10× longer) group). (d) XRD patterns of the membranes shown in (a-c) and simulated XRD pattern of ZIF-8.

The cross sections of membranes in the control group and in the Exposure group were characterized by high-angle annular dark-field scanning transmission electron microscopy (HAADF-STEM) and energy-dispersive x-ray (EDX) spectral imaging. As seen in **Figure 5-6a**, for the membrane in the control group, Zn, C and N signals, which indicate the existence of ZIFs, were detectable on top of and inside the γ-alumina layer with most of

them present at the top surface. In comparison, for the membrane in the Exposure group (**Figure 5-6b**), additional high-level Zn signal in a band of ~80 nm was detected beneath the ZIF-8 top layer, suggesting the existence of unconverted ZnO.

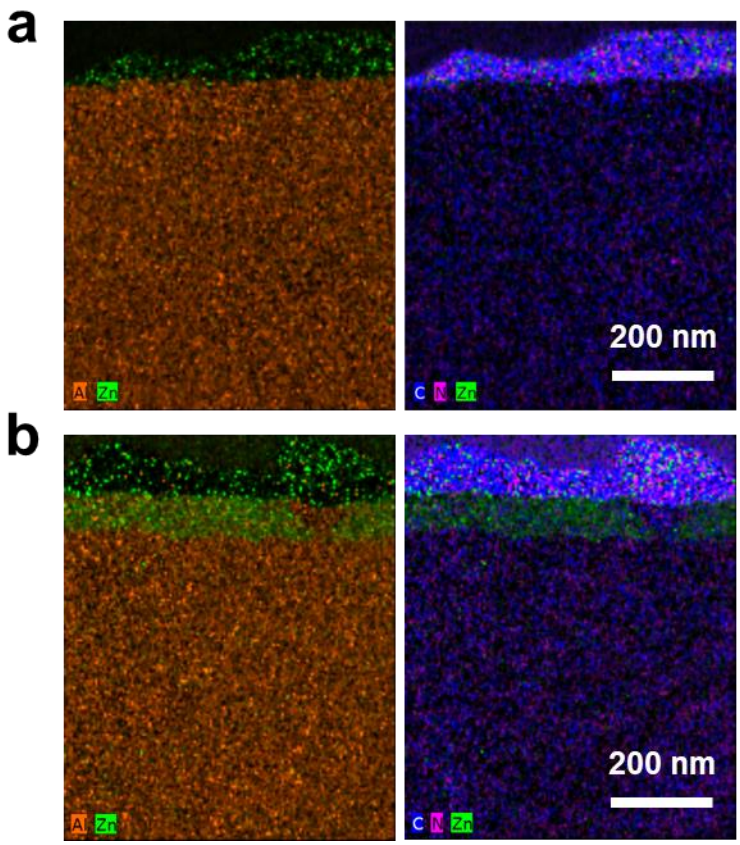

Figure 5-6. STEM-EDX images of the top part of membrane cross sections, showing corresponding spatial distribution of the aluminum (orange), zinc (green), carbon (blue) and nitrogen (pink). (a) Membrane fabricated under regular ALD condition (b) Membrane fabricated under Exposure mode ALD condition.

Based on the characterization, it is clear that with increased exposure time of the precursor in each cycle of ALD, a larger amount of ZnO is deposited. With mIm-vapor introduced from both sides of γ-alumina layer during ligand vapor treatment, as reported in ref. 47,

Zn-mIm species are formed throughout the γ-alumina layer with higher concentrations at the top and bottom (γ-alumina/α-alumina interface). The unconverted ZnO deposits in between form a band near the γ-alumina top surface, which contributes to the low permeance of the resulting membranes. It also suggests that the thinness of ZnO deposits in the control group is due to a limited exposure time of ALD precursor at a low concentration.

5.3.3 The effect of ALD H_2O pulse pressure on the membrane performance

In a typical ALD run, the pulse pressures corresponding to 0.015 s H_2O and DEZ pulses are ~ 300 Torr and 1 Torr respectively, with water pressure much higher than the DEZ pressure. H_2O residue is concerned to be left inside the pores at a high H_2O concentration before the next DEZ pulse arrives, leading to CVD-type ZnO formation. This could result in a thick deposit with low controllability. To seek the possibility of membrane performance enhancement, H_2O pulse pressure was decreased to ~150 Torr and ~1 Torr by reducing the H_2O pulse time.

As shown in **Figure 5-7**, upon ligand vapor treatment, membranes experiencing 1 Torr and 150 Torr water pulse pressures in ALD display permeances on the order of 10^{-10} mol m^{-2} s^{-1} Pa^{-1}, with propylene/propane selectivities of 1-2. Top-view SEM images and XRD patterns of the membranes are shown in **Figure 5-8**. All the membranes show a layer of ZIF-8 crystals on the top surface, but the microstructure underneath top layer could be different. According to the membrane characterization, the original H_2O pulse pressure at ~300 Torr is very desirable for realizing high performing membranes. With reduced H_2O pulse pressures, the layer-by-layer growth of ZnO is hindered such that the formed deposits

could not meet the required structure and continuity for efficient conversion into ZIFs, leading to low membrane performance.

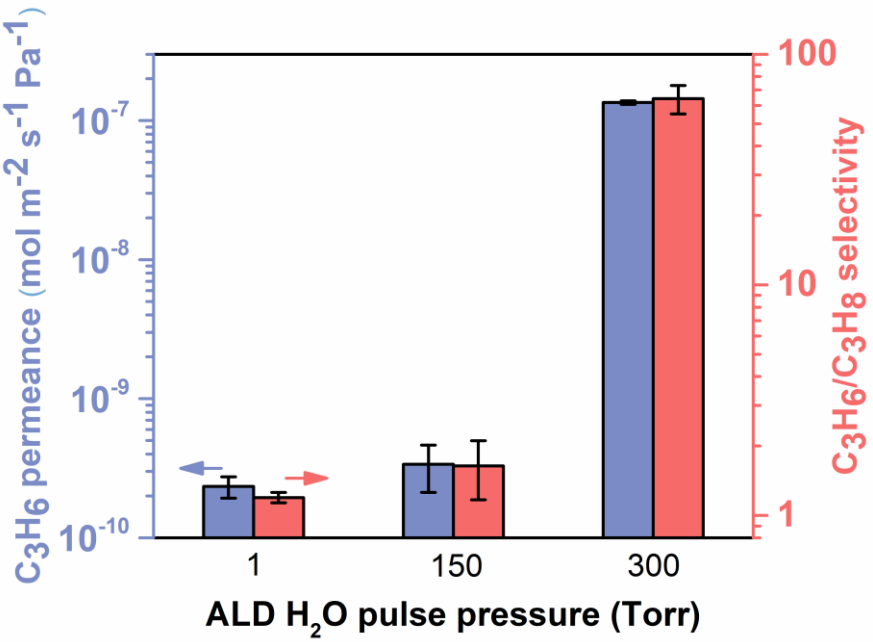

Figure 5-7. Propylene permeances and propylene/propane selectivities for membranes treated with different ALD water pulse pressures.

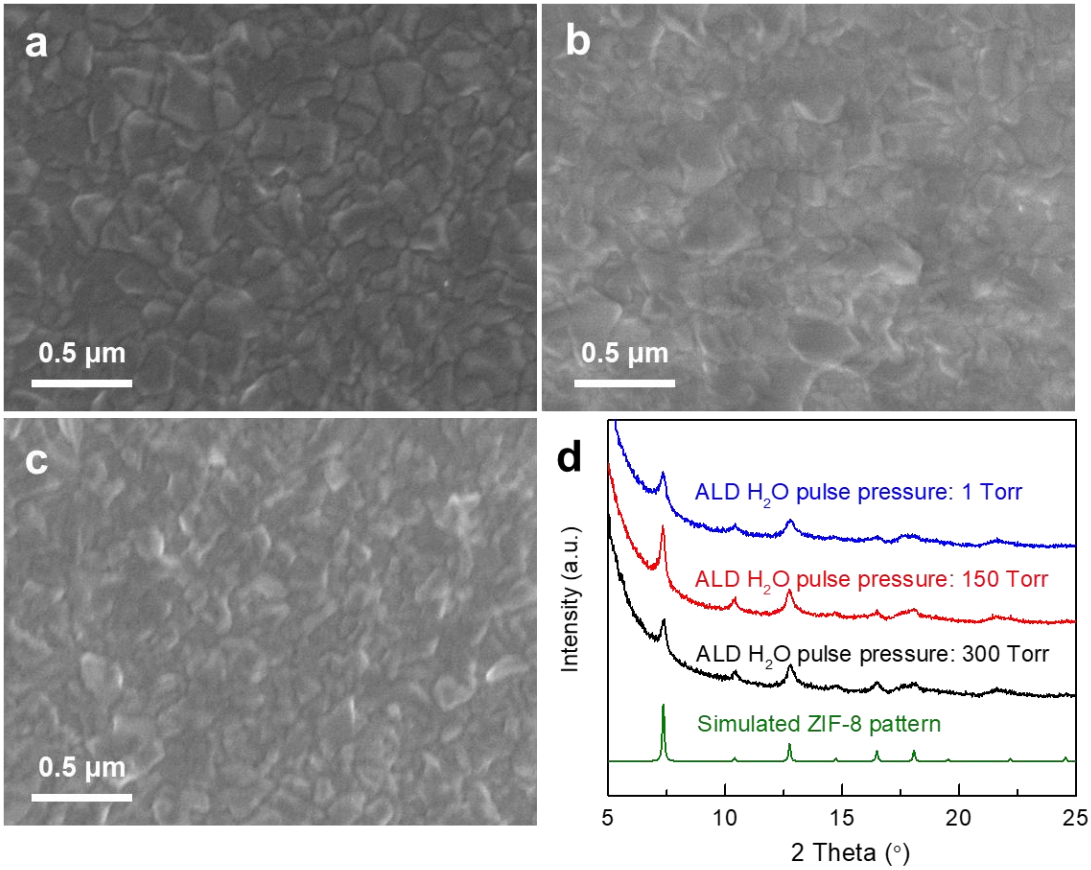

Figure 5-8. Top-view SEM images of membranes treated with different ALD water pulse pressures. (a) Regular ALD condition (control group) with H_2O pulse pressure of 300 Torr (b) ALD water pulse pressure of 150 Torr (c) ALD water pulse pressure of 1 Torr. (d) XRD patterns of the membranes shown in (a-c) and simulated XRD pattern of ZIF-8.

5.3.4 The effect of γ-alumina layer thickness on the membrane performance

As reported earlier, during the LIPS process, ZIFs are formed throughout the γ-alumina layer with higher concentrations at the top and bottom (γ-alumina/α-alumina interface). One possible way of improving the membrane performance is to reduce the γ-alumina layer thickness such that less ZIFs is formed. As the γ-alumina mesoporous layer is formed onto α-alumina substrates via dip coating followed by calcination, the dip coating time was

tuned to create supports with γ-alumina layer thickness of 3.1 μm and 4.4 μm, as demonstrated by the cross-sectional SEM images of membranes in **Figures 5-9a, b**. The LIPS process was then applied and the membrane performance is displayed in **Figure 5-9c**. Membranes with γ-alumina layer thickness of 3.1 μm and 4.4 μm show very similar propylene permeance and propylene/propane selectivity, meaning that reduced γ–alumina layer thickness does not affect the membrane separation performance. It also suggests that the primary determining factor for LIPS membrane performance is the ZIFs near the top and bottom of the γ–alumina layer.

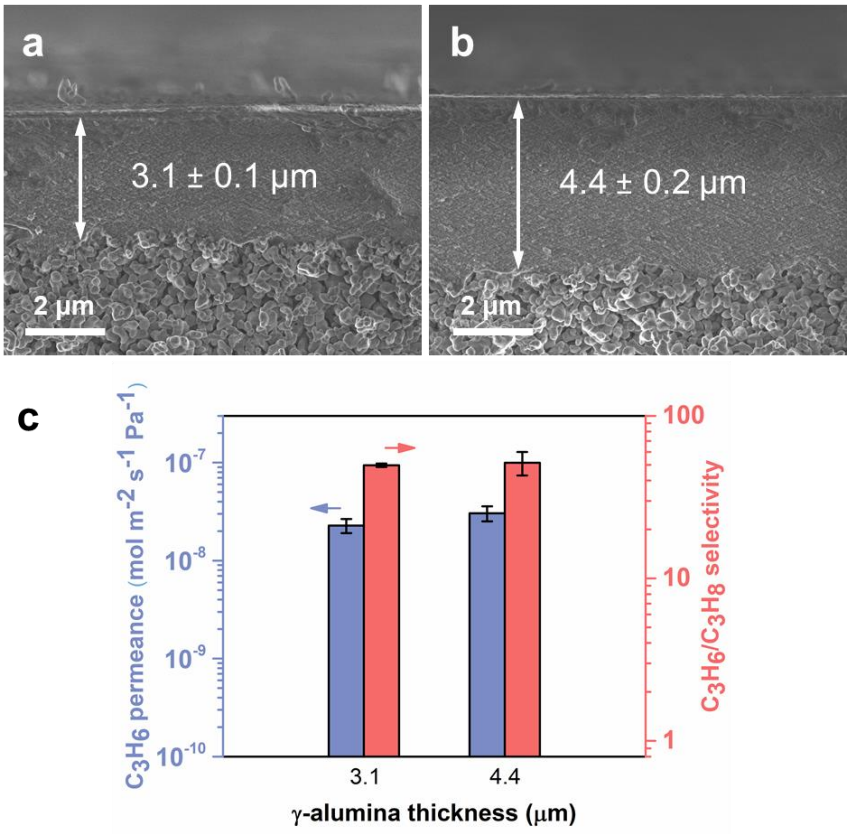

Figure 5-9. Cross-sectional SEM images of membranes with different γ–alumina layer thickness. (a) 3.1 ± 0.1 μm (b) 4.4 ± 0.2 μm. (c) Propylene permeances and propylene/propane selectivities for membranes with different γ–alumina layer thickness.

5.3.5 The effect of γ-alumina layer calcination temperature on the membrane performance

According to our previous discussion, the microstructure of the ALD deposits in the porous supports is critical to the final membrane performance after the ligand treatment. Besides the impact of ALD processing parameters, the microstructure of ALD deposit is also dependent on the pore structure of the porous supports. In an early report on LIPS membranes, the pore structure of γ-alumina layer containing mesopores (ca. 2 – 5 nm) and hydroxyl groups on the pore surface is desirable for LIPS membrane fabrication.[47] To explore how the pore structure affects the membrane performance, and to seek possibility of membrane performance improvement, the calcination temperature of the γ-alumina layer was varied. This study may also provide implications on LIPS membranes prepared with altered porous supports in the future.

γ-alumina layer is formed on the surface of α-alumina porous substrates by dip coating of γ-alumina sol, drying and calcination. Calcination temperature has an impact on the pore structure of the γ-alumina layer. With increased calcination temperature, the pore diameter is increased and the surface area is decreased.[97, 129] Here the calcination temperature of the γ-alumina layer was increased from 450 °C to 600 °C and the resultant ALD deposits and LIPS membranes were characterized by gas permeation measurement, SEM and XRD. As shown in **Table 5-2**, after 20 cycles of ZnO ALD, the propylene permeances for the γ-alumina supports calcined at 450 °C and 550 °C are on the order of 10^{-10} mol m^{-2} s^{-1} Pa^{-1}, indicating the effective blockage of the pores. However, for the γ-alumina layer calcined at 600 °C, the permeance of ALD deposits is 2 orders of magnitude higher, consistent with a more open structure in the γ-alumina layer whose pores are not effectively blocked after

20 cycles of ZnO ALD. In addition, the ZnO deposits should expand into a larger depth due to easier penetration of DEZ and water molecules through larger pores. After the mIm-vapor treatment, the propylene/propane separation performance of the membranes is shown in **Figure 5-10**. For membranes with γ-alumina layers calcined at 450 °C and 550 °C, the propylene permeances increase about 3 orders of magnitude reaching more than 1×10^{-7} mol m^{-2} s^{-1} Pa^{-1} and the propylene/propane selectivities are around 60. In contrast, for membranes with γ-alumina layers calcined at 600 °C, the propylene permeances decrease after ligand vapor treatment, with propylene permeances of around 6×10^{-9} mol m^{-2} s^{-1} Pa^{-1} and propylene/propane selectivities of around 10. The decrease in permeance after ligand vapor treatment is likely due to the volume expansion (more than 10-fold [45, 126]) during the ZnO-to-ZIFs conversion such that the formed ZIFs could fill the gas-leakage pathways in the original ZnO deposits. The membrane performance matches that from an overdosed membrane (e.g. the membranes in position I in the ALD chamber as seen in **Figure 5-3**) as a result of more unconverted ZnO deposited deep in the γ-alumina layer. Top-view SEM images and XRD patterns of membranes (**Figure 5-11**) reveal crystalline ZIF-8 layers on the top surface. The XRD intensity for the membrane with γ-alumina layer calcined at 600 °C is lower, suggesting a smaller crystal layer thickness. Overall, the mesoporous layer with a small pore size and a high surface area is desirable to form high performing membranes.

Table 5-2. Permeation data for supports with γ–alumina layers calcined at different temperatures after 20 cycles of ZnO ALD.

γ–alumina calcination T(°C)	Propylene permeance after 20 cycles of ALD (mol m^{-2} s^{-1} Pa^{-1})
450	2.7×10^{-10}
550	3.6×10^{-10}
600	4.0×10^{-8}

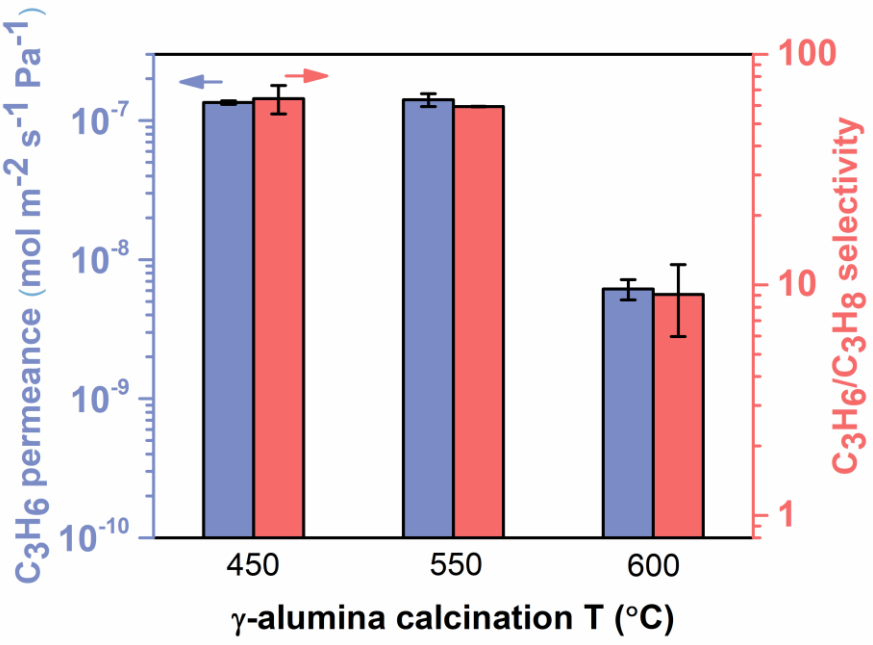

Figure 5-10. Propylene permeances and propylene/propane selectivities for membranes with γ–alumina layers calcined at different temperatures.

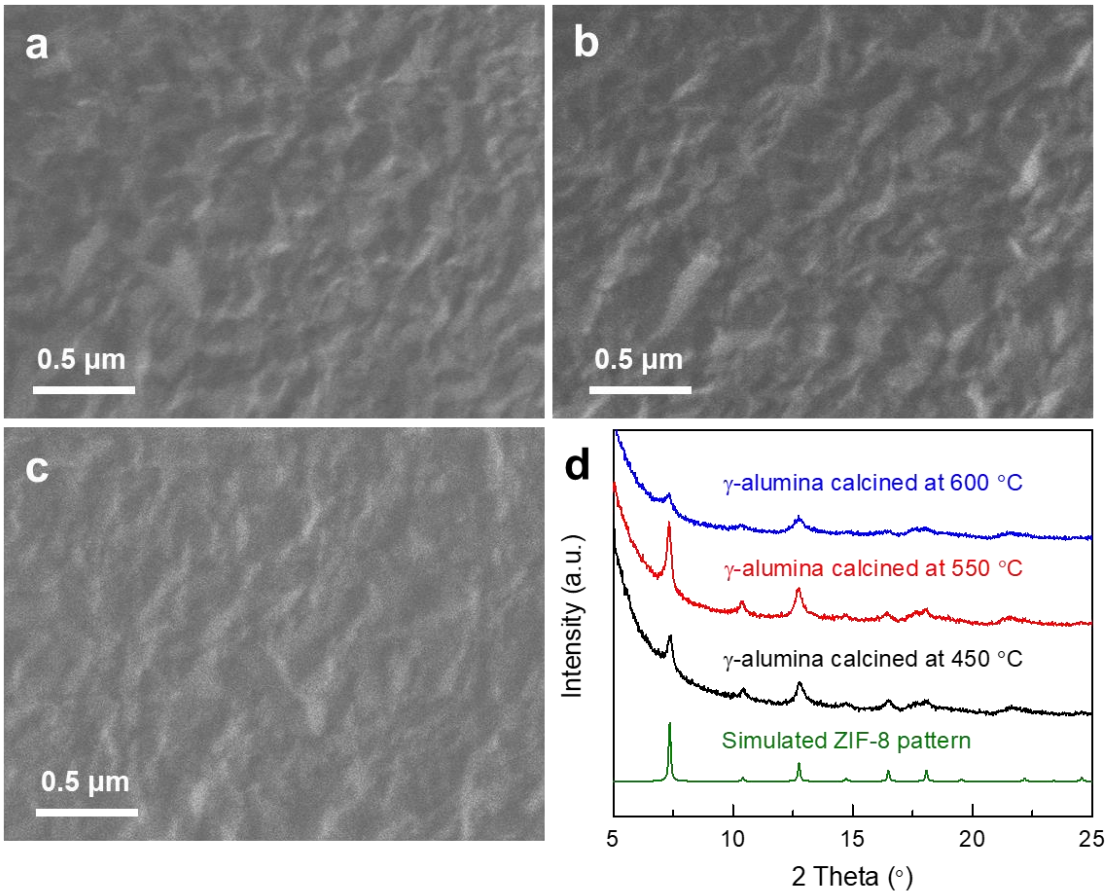

Figure 5-11. Top-view SEM images of membranes with γ–alumina layers calcined at (a) 450 °C, (b) 550 °C and (c) 600 °C. (d) XRD patterns of the membranes shown in (a-c) and simulated XRD pattern of ZIF-8.

5.3.6 The effect of freshness of ligand 2-methylimidazole on the membrane performance

Prior *in situ* powder XRD experiments and *in situ* thin film ellipsometry measurements for the mIm vapor-ZnO reaction show a faster ZnO-to-ZIF-8 conversion in a humid environment.[45, 126] To test if this behavior has an effect on the LIPS membranes, the freshness of ligand mIm was tuned. Fresh ligand obtained from a newly-opened chemical

bottle is expected to have much less adsorbed moisture than the ligand which has been exposed to the ambient air for more than 6 months. Both types of the mIm ligand were used to treat the ALD modified supports, and the performance of the resulting membranes was compared.

As shown in **Figure 5-12a**, the membranes made with mIm ligand having a higher moisture level demonstrate about 3 times higher propylene permeance and 2 times higher propylene/propane selectivity than the membranes made with fresh ligand having a low moisture level, indicating a higher ZnO-to-ZIF-8 conversion rate at a higher moisture level. In addition, the performance variation is smaller for membranes made with mIm ligand exposed to air for more than 6 months, suggestive of a higher controllability. Nevertheless, the XRD patterns **(Figure 5-12b)** and top-view SEM images **(Figures 5-12c,d)** of these two types of membranes are very similar. Likely, the moisture adsorbed in the ligand which has been exposed to air for a long time is released during the ligand vapor treatment process (at 125 °C), and facilitates the deprotonation of the ligand, the hydroxylation of ZnO and the mobility enhancement of Zn and mIm species during the reaction.[126, 130-132] As a result, more ZnO beneath the top ZIF-8 layer is converted after the same reaction time. Therefore, based on this study, the added level of moisture into the ligand powder during the storage is beneficial to yield membranes with higher propylene/propane separation performance.

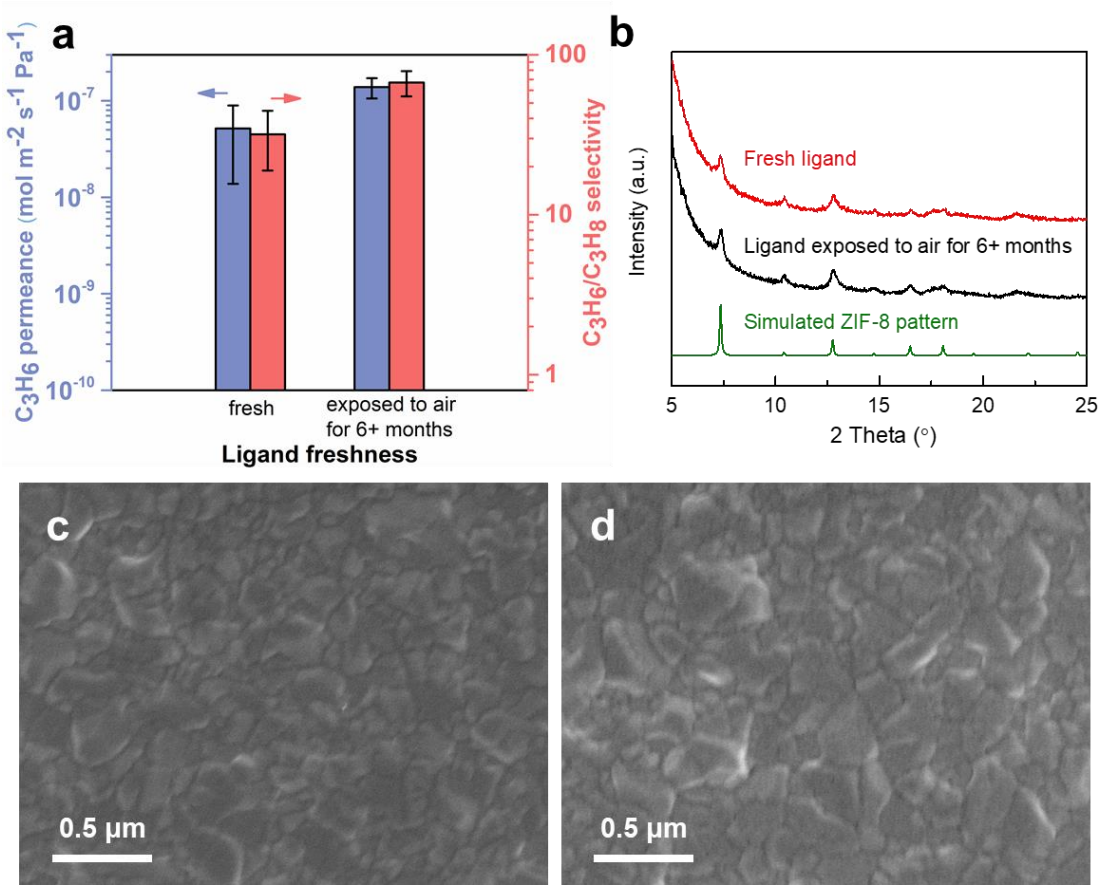

Figure 5-12. (a) Propylene permeances and propylene/propane selectivities for membranes treated with fresh ligand and ligand exposed to air for more than 6 months. (b) XRD patterns of the membranes treated with fresh ligand and ligand exposed to air for more than 6 months, as well as simulated XRD pattern of ZIF-8. Top-view SEM images of membranes treated with (c) fresh ligand and (d) ligand exposed to air for more than 6 months.

5.4 Conclusion

In summary, the LIPS process is studied by tailoring the ALD processing conditions, γ-alumina layer properties as well as the moisture levels in the ligand materials. It is found that an ALD processing condition enabling a thin non-permeable ZnO deposit, is critical

to realize consistently high membrane performance after ligand vapor treatment. The precursor concentration can be affected by the membrane position in the ALD chamber and the thinness of the ZnO deposit is due to a limited exposure time of ALD precursor at a low concentration. The change in γ-alumina layer thickness does not alter the membrane separation performance, suggesting that the ZIFs deposits near the interface (the top surface and γ-alumina/α-alumina interface) are the primary contributors to the separation performance. The γ-alumina calcination temperature which affects the mesopore size is important for LIPS process. When the calcination temperature is in the range of 450 °C to 550 °C, the membranes demonstrate very high performance, with propylene permeances above 1 $\times 10^{-7}$ mol m^{-2} s^{-1} Pa^{-1} and propylene/propane selectivities of around 60. When the calcination temperature is 600 °C, the pore diameter of the γ-alumina increases to an extent that the ALD deposits penetrate deeper, resulting in poorer membrane performance similar to that from a membrane with overdosed ZnO. In terms of ligand properties, membranes treated with ligand materials which have been exposed to the ambient air for over 6 months give rise to higher propylene permeance and propylene/propane selectivity than the membranes treated with ligand materials from a newly-opened chemical bottle. This is attributed to the higher moisture level adsorbed in the aged ligand materials that facilitates faster ZnO-to-ZIF-8 conversion. Overall, a process for reliable LIPS membrane fabrication is established which leads to superior propylene/propane separation performance holding promise for industrial applications.

Chapter 6: Concluding remarks

In conclusion, this dissertation discusses the development of synthesis methods for ultrathin MOF membranes which are a promising class of gas separation agents. To realize small membrane thickness, two approaches have been studied including the use of 2D MOF nanosheets as the membrane seed layer and an all-vapor-phase membrane synthesis process called LIPS.

A novel surfactant-assisted crystallization temperature-modulated synthesis method was developed for Zn(Bim)OAc MOF nanosheets with a thickness of 7 nm. Compared with nanosheets fabricated by top-down exfoliation, directly synthesized Zn(Bim)OAc nanosheets have a high yield and a well-controlled morphology which can be tuned by changing the synthesis temperature. In addition, a method based on TGA analysis was developed to allow the removal of the surfactant associated with nanosheets. The obtained nanosheets with high aspect ratio and desired pore orientation open new opportunities for their application as building blocks of gas separation membranes.

Using the Zn(Bim)OAc MOF nanosheets, uniform coatings were successfully prepared on porous γ-Al_2O_3 supports by vacuum filtration. Modification of the support surface by a small amount of ZnO enhances the membrane adhesion and 2-methyldimidazole vapor treatment transforms the non-permeable nanosheet deposits into thin propylene-selective membranes. This method of applying MOF nanosheets as metal precursor and ligand vapor treatment to synthesize thin membranes on top of the substrates demonstrates the feasibility to form thin membranes (ca. 100 nm) using MOF nanosheets as well as the tunability of the MOF structures upon ligand vapor treatment.

To target for low-cost membrane fabrication with a high processability, directly synthesized porous Cu(BDC) nanosheets were incorporated into a high permeability polymer 6FDA-Durene to form mixed matrix membranes that exhibited significant improvement in CO_2/N_2 selectivity without decreasing CO_2 permeability. It was demonstrated that the incorporated nanosheets are oriented and distributed uniformly along the thickness dimension of the membranes. Analysis of the permeation data using Cussler model for selective flake composites indicates the effective permeability of CO_2 for Cu(BDC) nanosheets in 6FDA-Durene is in the range of 380 – 510 Barrer, which is much higher than the effective permeability of CO_2 (~1 Barrer) for Cu(BDC) nanosheets in a low permeability polymer Matrimid. This discrepancy suggests that Cussler interpretation of selective flake composites behavior does not hold for Cu(BDC) nanosheets-based mixed matrix membranes and further investigations with polymers having a wide range of permeabilities are needed to interpret the behavior of Cu(BDC) nanosheets in polymer matrices.

Besides using 2D MOF nanosheets to realize thin membranes, an all-vapor-phase synthesis of ZIFs membranes called LIPS was studied. It was demonstrated that an ALD processing condition allowing a thin non-permeable ZnO deposit formation, and efficient ZnO-to-ZIFs conversion are very critical to realize consistent high membrane performance. With optimized support location and precursor pulse time in the ALD deposition, as well as γ-alumina layer calcination temperature and 2-methylimidazole ligand freshness, membranes with propylene permeances above 1.3×10^{-7} mol m^{-2} s^{-1} Pa^{-1} and propylene/propane selectivities above 60 were obtained which are superior to most of the previously reported ZIF-8 membranes.

Future work can focus on the extension of LIPS methods towards two directions. First, to facilitate the industrial applications of LIPS membranes, an integrated process of ALD of metal oxide in the porous supports and ligand vapor treatment in one reactor could be developed that is promising to increase the scale of the current process. Furthermore, the role of humidity in the process could be studied further to seek the possibility of better ZIFs conversion which leads to a higher separation throughput. In addition, LIPS membranes will be formed on the hollow fiber membrane geometry which has a much higher surface to volume ratio. Efforts in these scale-up processes will focus on the conditions for uniform γ-alumina supported on hollow fibers, uniform vapor concentration during deposition, faster ZnO-to-ZIFs conversion, good membrane packing and long-term stability.

The second future direction is developing LIPS membranes for ZIFs/MOFs with structures other than ZIF-8. Due to the exceptional degree of variability for both the metal ions and organic linkers in MOF structures, the development of LIPS membranes with varied metal oxides and ligand molecules could open up opportunities to form pore structures that are suitable for separation of other gas pairs such as CO_2/CH_4 and ethylene/ethane. The efforts will begin from identifying conditions to form uniform films on non-porous substrates such as Si wafers and then adapting them to porous supports. As the MOF-CVD methods have been developed to form ZIF-61, ZIF-67, ZIF-72, CuBDC and CuCDC thin films on Si wafers,[45, 122] these materials could serve as the starting point to form LIPS membranes other than ZIF-8.

Bibliography

[1] W. J. Koros, R. P. Lively, *AlChE J.* **2012**, *58*, 2624-2633.

[2] D. S. Sholl, R. P. Lively, *Nature* **2016**, *532*, 435-437.

[3] D. L. Gin, R. D. Noble, *Science* **2011**, *332*, 674-676.

[4] W. J. Koros, C. Zhang, *Nat. Mater.* **2017**, *16*, 289-297.

[5] W. J. Koros, *Chem. Eng. Prog.* **1995**, *91*, 68-81.

[6] L. M. Robeson, *J. Membr. Sci.* **1991**, *62*, 165-185.

[7] L. M. Robeson, *J. Membr. Sci.* **2008**, *320*, 390-400.

[8] H.-C. Zhou, J. R. Long, O. M. Yaghi, *Chem. Rev.* **2012**, *112*, 673-674.

[9] M. Eddaoudi, J. Kim, N. Rosi, D. Vodak, J. Wachter, M. O'Keeffe, O. M. Yaghi, *Science* **2002**, *295*, 469-472.

[10] O. M. Yaghi, M. O'Keeffe, N. W. Ockwig, H. K. Chae, M. Eddaoudi, J. Kim, *Nature* **2003**, *423*, 705-714.

[11] H. Li, M. Eddaoudi, M. O'Keeffe, O. M. Yaghi, *Nature* **1999**, *402*, 276-279.

[12] H. Furukawa, K. E. Cordova, M. O'Keeffe, O. M. Yaghi, *Science* **2013**, *341*, 1230444.

[13] J. Lee, O. K. Farha, J. Roberts, K. A. Scheidt, S. T. Nguyen, J. T. Hupp, *Chem. Soc. Rev.* **2009**, *38*, 1450-1459.

[14] J.-R. Li, R. J. Kuppler, H.-C. Zhou, *Chem. Soc. Rev.* **2009**, *38*, 1477-1504.

[15] T. M. McDonald, J. A. Mason, X. Kong, E. D. Bloch, D. Gygi, A. Dani, V. Crocella, F. Giordanino, S. O. Odoh, W. S. Drisdell, B. Vlaisavljevich, A. L. Dzubak, R. Poloni, S. K. Schnell, N. Planas, K. Lee, T. Pascal, L. F. Wan, D. Prendergast, J. B. Neaton, B. Smit, J. B. Kortright, L. Gagliardi, S. Bordiga, J. A. Reimer, J. R. Long, *Nature* **2015**, *519*, 303-308.

[16] Y. He, W. Zhou, G. Qian, B. Chen, *Chem. Soc. Rev.* **2014**, *43*, 5657-5678.

[17] N. L. Rosi, J. Eckert, M. Eddaoudi, D. T. Vodak, J. Kim, M. O'Keeffe, O. M. Yaghi, *Science* **2003**, *300*, 1127-1129.

[18] A. R. Millward, O. M. Yaghi, *J. Am. Chem. Soc.* **2005**, *127*, 17998-17999.

[19] M. Shah, M. C. McCarthy, S. Sachdeva, A. K. Lee, H.-K. Jeong, *Ind. Eng. Chem. Res.* **2012**, *51*, 2179-2199.

[20] K. S. Park, Z. Ni, A. P. Côté, J. Y. Choi, R. Huang, F. J. Uribe-Romo, H. K. Chae, M. O'Keeffe, O. M. Yaghi, *Proc. Natl. Acad. Sci.* **2006**, *103*, 10186-10191.

[21] Z. Lai, *Curr. Opin. Chem. Eng.* **2018**, *20*, 78-85.

[22] R. Banerjee, A. Phan, B. Wang, C. Knobler, H. Furukawa, M. O'Keeffe, O. M. Yaghi, *Science* **2008**, *319*, 939-943.

[23] K. Li, D. H. Olson, J. Seidel, T. J. Emge, H. Gong, H. Zeng, J. Li, *J. Am. Chem. Soc.* **2009**, *131*, 10368-10369.

[24] C. Zhang, R. P. Lively, K. Zhang, J. R. Johnson, O. Karvan, W. J. Koros, *J. Phys. Chem. Lett.* **2012**, *3*, 2130-2134.

[25] Y. Liu, Z. Ng, E. A. Khan, H.-K. Jeong, C.-b. Ching, Z. Lai, *Microporous Mesoporous Mater.* **2009**, *118*, 296-301.

[26] Y. Peng, Y. Li, Y. Ban, H. Jin, W. Jiao, X. Liu, W. Yang, *Science* **2014**, *346*, 1356-1359.

[27] Y. S. Li, F. Y. Liang, H. Bux, A. Feldhoff, W. S. Yang, J. Caro, *Angew. Chem. Int. Ed.* **2010**, *49*, 548-551.

[28] Y. Li, F. Liang, H. Bux, W. Yang, J. Caro, *J. Membr. Sci.* **2010**, *354*, 48-54.

[29] A. Huang, J. Caro, *Angew. Chem. Int. Ed.* **2011**, *50*, 4979-4982.

[30] S. R. Venna, M. A. Carreon, *J. Am. Chem. Soc.* **2010**, *132*, 76-78.

[31] Y. Liu, G. Zeng, Y. Pan, Z. Lai, *J. Membr. Sci.* **2011**, *379*, 46-51.

[32] S. Aguado, C.-H. Nicolas, V. Moizan-Baslé, C. Nieto, H. Amrouche, N. Bats, N. Audebrand, D. Farrusseng, *New J. Chem.* **2011**, *35*, 41-44.

[33] H. Bux, C. Chmelik, R. Krishna, J. Caro, *J. Membr. Sci.* **2011**, *369*, 284-289.

[34] J. B. James, J. Wang, L. Meng, Y. S. Lin, *Ind. Eng. Chem. Res.* **2017**, *56*, 7567-7575.

[35] Y. Pan, T. Li, G. Lestari, Z. Lai, *J. Membr. Sci.* **2012**, *390-391*, 93-98.

[36] H. T. Kwon, H.-K. Jeong, *J. Am. Chem. Soc.* **2013**, *135*, 10763-10768.

[37] A. J. Brown, N. A. Brunelli, K. Eum, F. Rashidi, J. R. Johnson, W. J. Koros, C. W. Jones, S. Nair, *Science* **2014**, *345*, 72-75.

[38] X. Ma, D. Liu, *Crystals* **2019**, *9*, 14.

[39] S. Qiu, M. Xue, G. Zhu, *Chem. Soc. Rev.* **2014**, *43*, 6116-6140.

[40] H. Bux, F. Liang, Y. Li, J. Cravillon, M. Wiebcke, J. r. Caro, *J. Am. Chem. Soc.* **2009**, *131*, 16000-16001.

[41] A. Huang, H. Bux, F. Steinbach, J. Caro, *Angew. Chem. Int. Ed.* **2010**, *49*, 4958-4961.

[42] A. Huang, W. Dou, J. r. Caro, *J. Am. Chem. Soc.* **2010**, *132*, 15562-15564.

[43] Q. Liu, N. Wang, J. r. Caro, A. Huang, *J. Am. Chem. Soc.* **2013**, *135*, 17679-17682.

[44] R. Ranjan, M. Tsapatsis, *Chem. Mater.* **2009**, *21*, 4920-4924.

[45] I. Stassen, M. Styles, G. Grenci, H. Van Gorp, W. Vanderlinden, S. De Feyter, P. Falcaro, D. De Vos, P. Vereecken, R. Ameloot, *Nat. Mater.* **2016**, *15*, 304-310.

[46] W. Li, P. Su, Z. Li, Z. Xu, F. Wang, H. Ou, J. Zhang, G. Zhang, E. Zeng, *Nat. Commun.* **2017**, *8*, 406.

[47] X. Ma, P. Kumar, N. Mittal, A. Khlyustova, P. Daoutidis, K. A. Mkhoyan, M. Tsapatsis, *Science* **2018**, *361*, 1008-1011.

[48] M. Tsapatsis, *Science* **2011**, *334*, 767-768.

[49] M. Y. Jeon, D. Kim, P. Kumar, P. S. Lee, N. Rangnekar, P. Bai, M. Shete, B. Elyassi, H. S. Lee, K. Narasimharao, S. N. Basahel, S. Al-Thabaiti, W. Xu, H. J. Cho, E. O. Fetisov, R. Thyagarajan, R. F. DeJaco, W. Fan, K. A. Mkhoyan, J. I. Siepmann, M. Tsapatsis, *Nature* **2017**, *543*, 690-694.

[50] P. Amo-Ochoa, L. Welte, R. González-Prieto, P. J. S. Miguel, C. J. Gómez-García, E. Mateo-Marti, S. Delgado, J. Gómez-Herrero, F. Zamora, *Chem. Commun.* **2010**, *46*, 3262-3264.

[51] P.-Z. Li, Y. Maeda, Q. Xu, *Chem. Commun.* **2011**, *47*, 8436-8438.

[52] A. Gallego, C. Hermosa, O. Castillo, I. Berlanga, C. J. Gómez‐García, E. Mateo‐Martí, J. I. Martínez, F. Flores, C. Gómez‐Navarro, J. Gómez‐Herrero, S. Delgado, F. Zamora, *Adv. Mater.* **2013**, *25*, 2141-2146.

[53] G. Xu, T. Yamada, K. Otsubo, S. Sakaida, H. Kitagawa, *J. Am. Chem. Soc.* **2012**, *134*, 16524-16527.

[54] K. Rui, G. Zhao, Y. Chen, Y. Lin, Q. Zhou, J. Chen, J. Zhu, W. Sun, W. Huang, S. X. Dou, *Adv. Funct. Mater.* **2018**, *28*, 1801554.

[55] Y. Peng, Y. Li, Y. Ban, W. Yang, *Angew. Chem. Int. Ed.* **2017**, *56*, 9757-9761.

[56] L. J. Han, D. Zheng, S. G. Chen, H. G. Zheng, J. Ma, *Small* **2018**, *14*, 1703873.

[57] Y. Ding, Y.-P. Chen, X. Zhang, L. Chen, Z. Dong, H.-L. Jiang, H. Xu, H.-C. Zhou, *J. Am. Chem. Soc.* **2017**, *139*, 9136-9139.

[58] M. Jian, H. Liu, T. Williams, J. Ma, H. Wang, X. Zhang, *Chem. Commun.* **2017**, *53*, 13161-13164.

[59] Y. Lin, H. Wan, F. Chen, X. Liu, R. Ma, T. Sasaki, *Dalton Trans.* **2018**, *47*, 7694-7700.

[60] J. Guo, Y. Zhang, Y. Zhu, C. Long, M. Zhao, M. He, X. Zhang, J. Lv, B. Han, Z. Tang, *Angew. Chem. Int. Ed.* **2018**, *57*, 6873-6877.

[61] Y. Xu, B. Li, S. Zheng, P. Wu, J. Zhan, H. Xue, Q. Xu, H. Pang, *J. Mater. Chem. A* **2018**, *6*, 22070-22076.

[62] A. Pustovarenko, M. G. Goesten, S. Sachdeva, M. Shan, Z. Amghouz, Y. Belmabkhout, A. Dikhtiarenko, T. Rodenas, D. Keskin, I. K. Voets, B. M. Weckhuysen, M. Eddaoudi, L. C. P. M. de Smet, E. J. R. Sudhölter, F. Kapteijn, B. Seoane, J. Gascon, *Adv. Mater.* **2018**, *30*, 1707234.

[63] K. Zhao, S. Liu, G. Ye, Q. Gan, Z. Zhou, Z. He, *J. Mater. Chem. A* **2018**, *6*, 2166-2175.

[64] T. He, B. Ni, S. Zhang, Y. Gong, H. Wang, L. Gu, J. Zhuang, W. Hu, X. Wang, *Small* **2018**, *14*, 1703929.

[65] M. Zhao, Y. Wang, Q. Ma, Y. Huang, X. Zhang, J. Ping, Z. Zhang, Q. Lu, Y. Yu, H. Xu, Y. Zhao, H. Zhang, *Adv. Mater.* **2015**, *27*, 7372-7378.

[66] T. Rodenas, I. Luz, G. Prieto, B. Seoane, H. Miro, A. Corma, F. Kapteijn, F. X. L. i Xamena, J. Gascon, *Nat. Mater.* **2015**, *14*, 48-55.

[67] M. Shete, P. Kumar, J. E. Bachman, X. Ma, Z. P. Smith, W. Xu, K. A. Mkhoyan, J. R. Long, M. Tsapatsis, *J. Membr. Sci.* **2018**, *549*, 312-320.

[68] L. Huang, X. Zhang, Y. Han, Q. Wang, Y. Fang, S. Dong, *J. Mater. Chem. A* **2017**, *5*, 18610-18617.

[69] Y. Wang, L. Li, L. Yan, X. Gu, P. Dai, D. Liu, J. G. Bell, G. Zhao, X. Zhao, K. M. Thomas, *Chem. Mater.* **2018**, *30*, 3048-3059.

[70] P. Deria, J. E. Mondloch, O. Karagiaridi, W. Bury, J. T. Hupp, O. K. Farha, *Chem. Soc. Rev.* **2014**, *43*, 5896-5912.

[71] N. Stock, S. Biswas, *Chem. Rev.* **2012**, *112*, 933-969.

[72] J. J. De Yoreo, P. U. P. A. Gilbert, N. A. J. M. Sommerdijk, R. L. Penn, S. Whitelam, D. Joester, H. Zhang, J. D. Rimer, A. Navrotsky, J. F. Banfield, A. F. Wallace, F. M. Michel, F. C. Meldrum, H. Cölfen, P. M. Dove, *Science* **2015**, *349*, aaa6760.

[73] M. A. Snyder, M. Tsapatsis, *Angew. Chem. Int. Ed.* **2007**, *46*, 7560-7573.

[74] I. Ogino, E. A. Eilertsen, S.-J. Hwang, T. Rea, D. Xie, X. Ouyang, S. I. Zones, A. Katz, *Chem. Mater.* **2013**, *25*, 1502-1509.

[75] W.-g. Kim, S. Nair, *Chem. Eng. Sci.* **2013**, *104*, 908-924.

[76] X. Wang, C. Chi, K. Zhang, Y. Qian, K. M. Gupta, Z. Kang, J. Jiang, D. Zhao, *Nat. Commun.* **2017**, *8*, 14460.

[77] K. Varoon, X. Zhang, B. Elyassi, D. D. Brewer, M. Gettel, S. Kumar, J. A. Lee, S. Maheshwari, A. Mittal, C.-Y. Sung, M. Cococcioni, L. F. Francis, A. V. McCormick, K. A. Mkhoyan, M. Tsapatsis, *Science* **2011**, *334*, 72-75.

[78] S. C. Junggeburth, L. Diehl, S. Werner, V. Duppel, W. Sigle, B. V. Lotsch, *J. Am. Chem. Soc.* **2013**, *135*, 6157-6164.

[79] Y. Jiang, H. Liu, X. Tan, L. Guo, J. Zhang, S. Liu, Y. Guo, J. Zhang, H. Wang, W. Chu, *ACS Appl. Mater. Interfaces* **2017**, *9*, 25239-25249.

[80] X.-M. Li, *Acta Crystallogr., Sect. E: Struct. Rep. Online* **2007**, *63*, m1984-m1984.

[81] L. Arai, M. A. Nadeem, M. Bhadbhade, J. A. Stride, *Dalton Trans.* **2010**, *39*, 3372-3374.

[82] N. Rangnekar, M. Shete, K. V. Agrawal, B. Topuz, P. Kumar, Q. Guo, I. Ismail, A. Alyoubi, S. Basahel, K. Narasimharao, C. W. Macosko, K. A. Mkhoyan, S. Al-Thabaiti, B. Stottrup, M. Tsapatsis, *Angew. Chem. Int. Ed.* **2015**, *54*, 6571-6575.

[83] R. Makiura, S. Motoyama, Y. Umemura, H. Yamanaka, O. Sakata, H. Kitagawa, *Nat. Mater.* **2010**, *9*, 565-571.

[84] L. Imperiali, K.-H. Liao, C. Clasen, J. Fransaer, C. W. Macosko, J. Vermant, *Langmuir* **2012**, *28*, 7990-8000.

[85] Q.-F. Yang, X.-B. Cui, J.-H. Yu, J. Lu, X.-Y. Yu, X. Zhang, J.-Q. Xu, Q. Hou, T.-G. Wang, *CrystEngComm* **2008**, *10*, 1534-1541.

[86] E. J. Kirkland, *Advanced computing in electron microscopy*, Springer, New York, **2010**.

[87] M. L. Odlyzko, J. T. Held, K. A. Mkhoyan, *J. Vac. Sci. Technol. A* **2016**, *34*, 041603.

[88] E. A. Flügel, M. T. Aronson, S. C. Junggeburth, B. F. Chmelka, B. V. Lotsch, *CrystEngComm* **2015**, *17*, 463-470.

[89] E. J. Kirkland, R. F. Loane, J. Silcox, *Ultramicroscopy* **1987**, *23*, 77-96.

[90] S. J. Pennycook, *Ultramicroscopy* **1989**, *30*, 58-69.

[91] Z. W. Wang, Z. Y. Li, S. J. Park, A. Abdela, D. Tang, R. E. Palmer, *Phys. Rev. B* **2011**, *84*, 073408.

[92] F. Yang, M. Wu, Y. Wang, S. Ashtiani, H. Jiang, *ACS Appl. Mater. Interfaces* **2018**, *11*, 990-997.

[93] P. Nian, H. Liu, X. Zhang, *J. Membr. Sci.* **2019**, *573*, 200-209.

[94] Y. Li, L. Lin, M. Tu, P. Nian, A. J. Howarth, O. K. Farha, J. Qiu, X. Zhang, *Nano Res.* **2018**, *11*, 1850-1860.

[95] Y. Li, H. Liu, H. Wang, J. Qiu, X. Zhang, *Chem. Sci.* **2018**, *9*, 4132-4141.

[96] K. V. Agrawal, B. Topuz, Z. Jiang, K. Nguenkam, B. Elyassi, L. F. Francis, M. Tsapatsis, M. Navarro, *AlChE J.* **2013**, *59*, 3458-3467.

[97] C.-H. Chang, R. Gopalan, Y. S. Lin, *J. Membr. Sci.* **1994**, *91*, 27-45.

[98] H. Knözinger, P. Ratnasamy, *Catal. Rev. Sci. Eng.* **1978**, *17*, 31-70.

[99] S. Chu, *Science* **2009**, *325*, 1599.

[100] D. M. D'Alessandro, B. Smit, J. R. Long, *Angew. Chem. Int. Ed.* **2010**, *49*, 6058-6082.

[101] G. Férey, *Chem. Soc. Rev.* **2008**, *37*, 191-214.

[102] L.-C. Lin, A. H. Berger, R. L. Martin, J. Kim, J. A. Swisher, K. Jariwala, C. H. Rycroft, A. S. Bhown, M. W. Deem, M. Haranczyk, B. Smit, *Nat. Mater.* **2012**, *11*, 633-641.

[103] G. T. Rochelle, *Science* **2009**, *325*, 1652-1654.

[104] A. S. Bhown, B. C. Freeman, *Environ. Sci. Technol.* **2011**, *45*, 8624-8632.

[105] S. Choi, J. H. Drese, C. W. Jones, *ChemSusChem* **2009**, *2*, 796-854.

[106] A. D. Ebner, J. A. Ritter, *Sep. Sci. Technol.* **2009**, *44*, 1273-1421.

[107] M. Rezakazemi, A. E. Amooghin, M. M. Montazer-Rahmati, A. F. Ismail, T. Matsuura, *Prog. Polym. Sci.* **2014**, *39*, 817-861.

[108] H.-K. Jeong, W. Krych, H. Ramanan, S. Nair, E. Marand, M. Tsapatsis, *Chem. Mater.* **2004**, *16*, 3838-3845.

[109] B. Seoane, J. Coronas, I. Gascon, M. Etxeberria Benavides, O. Karvan, J. Caro, F. Kapteijn, J. Gascon, *Chem. Soc. Rev.* **2015**, *44*, 2421-2454.

[110] J. E. Bachman, J. R. Long, *Energy Environ. Sci.* **2016**, *9*, 2031-2036.

[111] M. Zhao, Y. Huang, Y. Peng, Z. Huang, Q. Ma, H. Zhang, *Chem. Soc. Rev.* **2018**, *47*, 6267-6295.

[112] F. Xue, P. Kumar, W. Xu, K. A. Mkhoyan, M. Tsapatsis, *Chem. Mater.* **2018**, *30*, 69-73.

[113] Y. Yang, K. Goh, R. Wang, T.-H. Bae, *Chem. Commun.* **2017**, *53*, 4254-4257.

[114] W.-H. Lin, T.-S. Chung, *J. Membr. Sci.* **2001**, *186*, 183-193.

[115] S. L. Liu, R. Wang, T. S. Chung, M. L. Chng, Y. Liu, R. H. Vora, *J. Membr. Sci.* **2002**, *202*, 165-176.

[116] S. Japip, Y. Xiao, T.-S. Chung, *Ind. Eng. Chem. Res.* **2016**, *55*, 9507-9517.

[117] K. Tan, N. Nijem, Y. Gao, S. Zuluaga, J. Li, T. Thonhauser, Y. J. Chabal, *CrystEngComm* **2015**, *17*, 247-260.

[118] A. C. Elder, S. Bhattacharyya, S. Nair, T. M. Orlando, *J. Phys. Chem. C* **2018**, *122*, 10413-10422.

[119] E. L. Cussler, *J. Membr. Sci.* **1990**, *52*, 275-288.

[120] J. A. Sheffel, M. Tsapatsis, *J. Membr. Sci.* **2009**, *326*, 595-607.

[121] T. T. Moore, W. J. Koros, *J. Mol. Struct.* **2005**, *739*, 87-98.

[122] T. Stassin, S. Rodríguez-Hermida, B. Schrode, A. J. Cruz, F. Carraro, D. Kravchenko, V. Creemers, I. Stassen, T. Hauffman, D. De Vos, P. Falcaro, R. Resel, R. Ameloot, *Chem. Commun.* **2019**, *55*, 10056-10059.

[123] S. Han, R. A. Ciufo, M. L. Meyerson, B. K. Keitz, C. B. Mullins, *J. Mater. Chem. A* **2019**, *7*, 19396-19406.

[124] E. Ahvenniemi, M. Karppinen, *Chem. Mater.* **2016**, *28*, 6260-6265.

[125] K. B. Lausund, O. Nilsen, *Nat. Commun.* **2016**, *7*, 13578.

[126] A. J. Cruz, I. Stassen, M. Krishtab, K. Marcoen, T. Stassin, S. Rodríguez-Hermida, J. Teyssandier, S. Pletincx, R. Verbeke, V. Rubio-Giménez, S. Tatay, C. Martí-Gastaldo, J. Meersschaut, P. M. Vereecken, S. De Feyter, T. Hauffman, R. Ameloot, *Chem. Mater.* **2019**, *31*, 9462-9471.

[127] M. Krishtab, I. Stassen, T. Stassin, A. J. Cruz, O. O. Okudur, S. Armini, C. Wilson, S. De Gendt, R. Ameloot, *Nat. Commun.* **2019**, *10*, 3729.

[128] H. T. Kwon, H.-K. Jeong, A. S. Lee, H. S. An, T. Lee, E. Jang, J. S. Lee, J. Choi, *Chem. Commun.* **2016**, *52*, 11669-11672.

[129] C. W. Seo, K. D. Jung, K. Y. Lee, K. S. Yoo, *Ind. Eng. Chem. Res.* **2008**, *47*, 6573-6578.

[130] Q. Shi, Z. Chen, Z. Song, J. Li, J. Dong, *Angew. Chem. Int. Ed.* **2011**, *50*, 672-675.

[131] J. T. Newberg, C. Goodwin, C. Arble, Y. Khalifa, J. A. Boscoboinik, S. Rani, *J. Phys. Chem. B* **2018**, *122*, 472-478.

[132] T. Weckman, K. Laasonen, *J. Phys. Chem. C* **2016**, *120*, 21460-21471.